



HAL
open science

Etude d'interface entre matrice polymère et renforts à base de carbone, à l'aide d'observations multiéchelles et multimodales en microscopie électronique

Yu Liu

► **To cite this version:**

Yu Liu. Etude d'interface entre matrice polymère et renforts à base de carbone, à l'aide d'observations multiéchelles et multimodales en microscopie électronique. Autre. Université Paris Saclay (COMUE), 2017. Français. NNT : 2017SACLC059 . tel-01678885v2

HAL Id: tel-01678885

<https://theses.hal.science/tel-01678885v2>

Submitted on 18 Jan 2018

HAL is a multi-disciplinary open access archive for the deposit and dissemination of scientific research documents, whether they are published or not. The documents may come from teaching and research institutions in France or abroad, or from public or private research centers.

L'archive ouverte pluridisciplinaire **HAL**, est destinée au dépôt et à la diffusion de documents scientifiques de niveau recherche, publiés ou non, émanant des établissements d'enseignement et de recherche français ou étrangers, des laboratoires publics ou privés.

NNT: 2017SACL059

**THÈSE DE DOCTORAT
DE
L'UNIVERSITE PARIS-SACLAY
PREPAREE A
CENTRALESUPELEC**

Ecole doctorat N° 579

Sciences mécaniques et énergétiques, matériaux et géosciences

Laboratoire de Mécanique des Sols, Structures et Matériaux

CNRS UMR 8579

Spécialité de doctorat: Science des matériaux

par

M. Yu LIU

Etude d'interfaces entre matrice polymère et renforts à base de carbone, à l'aide d'observations multiéchelles et multimodales en microscopie électronique

Thèse présentée et soutenue à Gif-sur-Yvette, le 10 novembre 2017

Devant le jury composé de :

M. Gilles LUBINEAU	Professeur, KAUST	Président
Mme. Isabelle ROYAUD	Professeur, Univ-Lorraine	Rapporteur
M. Jean-François GERARD	Professeur, INSA Lyon	Rapporteur
M. Gilles REGNIER	Professeur, ENSAM	Examineur
M. Lionel PICHON	Directeur de Recherche, CentraleSupélec	Examineur
Mme. Ann-Lenaig HAMON	Maître de conférence, CentraleSupélec	Encadrant
M. Jinbo BAI	Directeur de Recherche, CentraleSupélec	Directeur de thèse

Acknowledgement

First, I would like to thank my thesis committee: Prof. Gilles Lubineau, Prof. Gilles Regnier, Prof. Isabelle Royaud, Prof. Jean-Francois Gerard and Prof. Lionel Pichon, for their insightful comments which helped me to improve the quality of my thesis.

I would also like to express my sincere gratitude to my supervisor Ms. Ann-Lenaig Hamon and Mr. Jinbo Bai for their continuous support on my Ph.D study and related research works, for their patience and motivation. Otherwise, I could not have finished my thesis.

Then I would like to thank my master's supervisor Prof. Tao Zhang for recommending me to do this PhD study in Jinbo Bai's group and for his continuous encouragement and care for my life in France.

Meanwhile, I would also like to take this opportunity to express my gratitude to the financial support from China Scholarship Council (CSC), the MATMECA consortium and the ANR under contract number ANR-10-EQPX-37.

Special gratitude is extended to Dr. Thomas Reiss and Dr. Paul Haghi-Ashtiani for the instruction of operating both SEM and TEM. I would also like to thank Dr. Pascale Gemeiner, Dr. Sébastien Roland and Dr. Xiaolong TU who gave me a lot of help in my experiments. I would like to express my thanks to Ms. Farida Djebbari, Sokona Konate, as well as all the staff of the MSSMat lab, for their assistance in the past three years.

Additionally, I also owe my sincere gratitude to my friends and my fellows who gave me their help, and I treasure the time we spent together during the past three years in France: Delong He, Benhui Fan, Michael Callahan, Mathieu Bonneric, Xue Bai, Xiaoxin Lu, Wangshu Chen, Hang Zhao, Diana Salem, Yang Ma, Shan Feng, Yiguo Xu, Minhao Yang, Hanlu Zhang, Anne Zhang, Rafael Mattedi, etc.

Last but not least, I would like to thank my family for their accompaniments and comforts especially when I was in low mood. Their smiles and sweet words were so magic for me to help me face bravely difficulties in my life. Thanks to Mengxue, without your continuous encouragement and support, I could not have finished my thesis.

Content

<i>Acknowledgement</i>	3
<i>Abstract</i>	9
<i>Résumé</i>	11
<i>Acronyms and symbols</i>	13
<i>List of figures</i>	17
<i>List of tables</i>	23
<i>Chapter 1 Background and introduction</i>	25
1.1 Carbon-based materials and surface modification	26
1.1.1 Carbon fibers (CFs)	26
1.1.2 Graphene and graphite nano-platelets (GNPs)	32
1.2 Polymer composites	40
1.2.1 Graphene reinforced nanocomposites	42
1.2.2 CF-reinforced composites	45
1.3 Interfacial study between the polymer matrix and reinforcements	48
1.3.1 Methods for GNPs reinforced nano-composites	48
1.3.2 Methods for CF reinforced composites	51
1.4 Transmission electron microscopy (TEM) in nanocomposite study	54
1.4.1 Experimental techniques	54
1.4.2 Identification of interface/interphase by TEM	56
1.5 Motivation and overview	61
References	62
<i>Chapter 2 Surface treatment of the reinforcements</i>	71
<i>Introduction</i>	71
2.1 Materials	72
2.2 Experiment	73
2.2.1 Synthesis of CNT-CFs and CNT-GNPs	73
2.2.2 Modification of the different types of fillers: Graphene oxide (GO), desized CFs, oxidized GNPs (O-GNPs) and CNT-CFs	74
2.3 Characterization results and discussion	74
2.3.1 Morphology characterization of the fillers	75
2.3.2 Basic characterization of the fillers	80

2.4 Partial conclusion.....	85
References.....	86
<i>Chapter 3 Comparison of different surface treatments of carbon fibers used as reinforcements in epoxy composites: Interfacial strength measurements by in-situ scanning electron microscope tensile tests.....</i>	
	87
<i>Introduction.....</i>	87
3.1 Experiment and characterization.....	88
3.1.1 Preparation of CNT-CF/epoxy composites.....	88
3.1.2 Tensile tests of pure epoxy.....	88
3.1.3 Single fiber test.....	88
3.1.4 Tensile and TEM samples preparation by FIB.....	88
3.1.5 Characterization.....	90
3.2 Results and discussion.....	90
3.2.1 Basic characterization of different types of CFs.....	90
3.2.2 Interfacial shear strength (IFSS).....	91
3.2.3 <i>In-situ</i> interfacial strength measurement.....	92
3.2.4 Simulation.....	92
3.2.5 Experiment by FIB-SEM.....	96
3.2.6 <i>In-situ</i> tensile test for GNP/epoxy composite.....	100
3.2.7 STEM/EDX characterization of interface/interphase.....	101
References.....	107
<i>Chapter 4 Intensive EELS study of epoxy composites reinforced by graphene-based nanofillers.....</i>	
	109
<i>Introduction.....</i>	109
4.1.1 Preparation of GNP-based nanofiller/epoxy composites.....	110
4.1.2 TEM sample preparation by FIB.....	110
4.2 Results and discussion.....	112
4.2.1 Morphology characterization of nanofillers and epoxy composites.....	112
4.2.2 Composite properties.....	113
4.2.3 EELS study.....	115
4.2.3.1 Influence of sample thickness for EELS acquisition.....	115
4.2.3.2 Influence of exposure time on the core-loss spectra.....	117
4.2.3.3 Influence of the sample thickness on the core-loss spectra.....	118
4.2.3.4 Low-loss and core-loss spectra of G/epoxy composites.....	121

4.2.4 Energy dispersive X-ray spectroscopy (EDX) characterization of G/epoxy composites	124
<i>Chapter 5 Quantitative Study of Interface/Interphase in Epoxy/Graphene-based Nanocomposites by Combining STEM and EELS analyses</i>	129
Introduction	129
5.1 Results and discussion	131
5.1.1 GNP/ & GO/epoxy nanocomposites	131
5.1.2 Interphase characterization	133
5.2 Partial conclusion	138
References	140
<i>Chapter 6 Conclusion and perspectives</i>	141
6.1 General conclusions	141
6.1.1. Surface modification of carbon-based fillers	141
6.1.2 The interface study between CF and epoxy	142
6.1.3 Interface & interphase study of GNP/epoxy composites	142
6.2 Perspective	144
<i>Appendix I Directly measuring interfacial shear strength between Polymethyl methacrylate and graphene nanoplatelets</i>	145
<i>Appendix II The peak positions values of Figure 5.3</i>	151

Abstract

This thesis aims to investigate the multiscale (nano-, micro-, and macro-scopic) behavior of the composites based on a fine investigation using the most modern techniques, to understand the interfaces and to quantify them. Two series of reinforcements on a micrometer scale, carbon fibers (CFs) and graphene-based materials, were studied here. To improve the interactions between these nanofillers and the surrounding polymer matrix, two major routes were used in this thesis: the oxidation of the fillers and the grafting of carbon nanotubes on their surface.

The study itself was conducted on a microscopic scale on the interfacial strength between CFs and the epoxy matrix, with tensile tests carried out *in-situ* in the chamber of a double-column FIB-SEM microscope (scanning electron microscope coupled to a focused ion beam). The ion beam was used to mill a thin bond-shaped tensile specimen of composite containing both an epoxy and a CF part. The tensile stress field was applied using the nanomanipulator and the test was observed both via the ionic and the electronic columns (with two different angles of view) to estimate the strain field, hence the interfacial strength when the failure is observed. A similar experiment was led on a composite with GNPs.

Finally, the transmission electron microscopy (TEM) study of the interface region between the epoxy and the graphene-based nanofillers revealed the existence of an interphase and allowed to measure its thickness and give an indication of its nature. For this purpose, an EELS (electron energy-loss spectroscopy) analysis was carried out, making it possible to measure the density of the sample very locally (probe size of the order of a tenth of a nanometer) across or parallelly to an interface. A scenario on the chemical bonding modes between the two media as a function of the surface treatment used makes it possible to explain the nature of the observed interphases.

Key words: Interface/Interphase, GNP/epoxy composites, CF/epoxy composites, FIB-SEM, Surface treatment, STEM-EELS

Résumé

Cette thèse vise à étudier le comportement multiéchelle (nano-, micro- et macroscopique) des composites, basé sur une étude fine utilisant les techniques les plus modernes pour comprendre les interfaces et les quantifier. Deux séries de renforts sur une échelle micrométrique, des fibres de carbone (CF) et des matériaux à base de graphène ont été utilisées ici. Pour améliorer l'interaction entre les nanorenforts et la matrice polymère, deux voies principales ont été utilisées dans cette thèse : l'oxydation des renforts et la greffe de nanotubes de carbone sur leur surface.

L'étude en elle-même a été menée à une échelle microscopique pour étudier la résistance interfaciale entre une fibre de carbone (CF) et la matrice époxy, avec des essais de traction effectués *in situ* dans la chambre d'un microscope à double colonne MEB-FIB (microscope électronique à balayage couplé à un faisceau d'ions focalisé). Le faisceau d'ions a été utilisé pour découper une éprouvette de traction du composite contenant à la fois de l'époxy et de la CF. Le champ de traction a été appliqué via le nanomanipulateur et l'essai a été observé via les deux colonnes ionique et électronique (sous deux angles de vue différents) et a permis d'estimer le champ de déformation, et donc la résistance interfaciale au moment de la rupture. Une expérience similaire a été menée sur un composite où les renforts sont des nanoplaquettes de graphène.

Enfin, l'étude en microscopie électronique en transmission de la région de l'interface entre l'époxy et les renforts a révélé la présence d'une interphase et a permis de mesurer son épaisseur et donner une indication de sa nature. À cette fin, une analyse EELS (spectroscopie par pertes d'énergie des électrons) a été effectuée, permettant de mesurer la densité de l'échantillon très localement (taille de sonde de l'ordre du dixième de nanomètre) en travers ou parallèlement à l'interface. Un scénario sur les modes de liaison chimique entre les deux milieux en fonction du traitement de surface utilisé permet d'expliquer la nature des interphases observées.

Mots clés: Interface/Interphase, Traitement de surface, Composites CF/époxy, Composites GNP/époxy, FIB-MEB, STEM-EELS

Acronyms

AFM	Atomic force microscopy
APO	Atmospheric plasma oxidation
CF(s)	Carbon fiber(s)
CF-CNTs	Carbon nanobubes grafted carbon fiber
CNT(s)	Carbon nanotube(s)
CVD	Chemical vapor deposition
DGEBA	Diglycidyl ether of bisphenol A
DMF	N',N'-Dimethyl formamide
EDX	Energy-dispersion X-ray spectrum
EELS	Electron energy loss spectroscopy
FE	Finite element modeling
FESEM	Field emission scanning electron microscope
FTIR	Fourier transform infrared spectroscopy
GIC	Graphite intercalation compound
GNP-CNT	Graphite nano-platelets carbon nano-tube hybrids
GNPs	Graphite nano-platelets
GO	Graphene oxide
IFSS	Interfacial shear strength
ILSS	Interlaminar shear strength
MWCNTs	Multi-walled carbon nanotubes
O-CF	Oxidized carbon fiber
O-GNPs	Oxidized graphite nano-platelets
PAN	Polyacrylonitrile

PDMS	Polydimethylsiloxane
PMMA	Poly(methyl methacrylate)
RTM	Resin transfer molding
SEM	scanning electron microscope
STEM	Scanning transmission electron microscope
SWCNT	Single-walled carbon nanotube
TEM	Transmission electron microscope
T _g	Glass transition temperature
TGA	Thermogravimetric analysis
VARTM	Vacuum-assisted resin transfer molding
XPS	X-ray photoelectron spectroscopy

Symbols

α	The convergence semi-angle
β	The collection semi-angle
γ	The sample tilt angle
λ	The mean free path
ρ	The density
b	The width of specimen
ε_0	The vacuum dielectric function
σ_{xx}	The tensile stress
σ_{xy}	The shear stress
D_{cnt}	The diameter of CNT
D_f	The diameter of fiber
E'	The storage modulus
E''	The loss modulus
E_0	The acceleration high voltage
E_m	The modulus of the matrix
E_f	The modulus of fiber
E_p	The peak position of low-loss spectrum
I_D	The intensity of D band in Raman spectrum

I_G	The intensity of G band in Raman spectrum
I_0	The zero-loss intensity
I_t	The total area measured up to some suitable energy loss in low-loss peak
m	The free electron mass
m^*	The electron effective mass
n_e	The valence electron density
P_1	The integrated area of π peak in C K-edge
P_2	The integrated area of σ peak in C K-edge
R	The radius of circle in tensile specimen
t	The thickness of specimen
$wt\%$	The weight fraction of composites
X_C	The element fraction of carbon
X_H	The element fraction of hydrogen
X_O	The element fraction of oxygen

Chapter 1

Figure 1.1 Precursor system of conventional carbon fibers (CFs). Oxidation crosslinking and pyrolysis (and/or graphitization) are used to fabricate conventional CFs from cellulose, polyacrylonitrile (PAN) and mesophase pitch precursors. The polycrystalline graphitic structure of CFs is generated from these precursor macromolecules.

Figure 1.2 (a) Crystal structure of graphite representing the ABAB stacking sequence; (b) Turbostratic structure of CFs.

Figure 1.3 (a) Schematic three-dimensional model of PAN-based CFs; (b) Transverse textures of mesophase pitch-based CFs.

Figure 1.4 Schematic for the techniques for surface modifications. Field emission scanning electron microscope (FEG-SEM) or scanning electron microscope (SEM) images show CF surfaces.

Figure 1.5 (left) Structure of graphene; (right) Single layer graphene pieces placed on SiO₂ wafer prepared by "scotch-tape method".

Figure 1.6 (A) Scanning electron microscopy (SEM) image of a graphene flake spanning an array of circular holes (scale bar, 3 μm); (B) Noncontact mode AFM image of one membrane, 1.5 mm in diameter. The solid blue line is a height profile along the dashed line. The step height at the edge of the membrane is around 2.5 nm; (C) Schematic illustration of nanoindentation on membranes; (D) AFM image of a fractured membrane.

Figure 1.7 Schematic of the experimental setup for measuring the thermal conductivity of graphene by confocal micro-Raman spectroscopy.

Figure 1.8 UV-visible spectra of roll-to-roll layer-by-layer transferred graphite and graphene films on quartz substrates.

Figure 1.9 Three typical graphene preparation methods: (A) mechanical cleavage method; (B) CVD methods and (C) chemical oxidation-reduction method.

Figure 1.10 SEM images of GNPs with different thickness and lateral sizes.

Figure 1.11 Schematic representation showing various covalent functionalization chemistry of graphene or GO. I: Reduction of GO into graphene. II: Covalent surface functionalization via diazonium reaction (ArN_2X). III: Functionalization of GO with sodium azide. IV: Reduction of azide functionalized GO with LiAlH_4 . V: Functionalization of azide functionalized GO through click chemistry (R-CHCH/CuSO_4). VI: Modification of GO with long alkyl chains by the acylation reaction. VII: Esterification of GO VIII: Nucleophilic ring-opening reaction of GO. IX: Functionalization of GO with organic isocyanates.

Figure 1.12 Sketch of the synthesis of CNT carpets directly from graphene.

Figure 1.13 Schematic illustration of the preparation of the graphite nanoplatelet-carbon nanotube hybrids (GCHs) and the graphite nanoplatelet-carbon nanotube hybrids/polydimethylsilicone (GCHs/PDMS) composites.

Figure 1.14 Different types of epoxy resins.

Figure 1.15 Schematic diagram of the preparation of aligned epoxy/graphene by impregnation method.

Figure 1.16 Schematic of a typical bag lay-up molding process.

Figure 1.17 Vacuum assisted resin transfer molding (RTM) process and fabrication setup.

Figure 1.18 Schematic of the pultrusion method.

Figure 1.19 Schematic showing the two-dimensional stress transfer model.

Figure 1.20 Interfacial stress transfer in GO nanocomposites demonstrated by Raman spectroscopy.

Figure 1.21 Illustration of the stretching method to measure the IFSS between GNPs and PMMA.

Figure 1.22 Mechanical responses of a polymer GNP-sheet nano-sandwich.

Figure 1.23 (a) Property improvements for 1 wt% nanoparticle–PMMA composites and (b,c) SEM images revealing the two typical types of nanoparticle–polymer interactions.

Figure 1.24 Four major fiber micromechanical test methods: (A) single fiber pull out test; (B) microdroplet method; (C) Fragmentation test; (D) Micro-indentation test.

Figure 1.25 TEM images of CF/epoxy composites prepared by two typical methods: (A) FIB; (B) ultramicrotome.

Figure 1.26 A classical view of electron scattering by a single atom (carbon). (a) Elastic scattering is caused by Coulomb attraction with the nucleus. Inelastic scattering results from Coulomb repulsion by (b) inner-, or (c) outer-shell electrons, which are excited to a higher energy state. The reverse transitions (de-excitation) are shown by broken arrows.

Figure 1.27 Dispersive and focusing properties of a magnetic prism (a) in a plane perpendicular to the magnetic field (side view) and (b) parallel to the field (top view). Solid lines represent zero-loss electrons; dashed lines represent those that have lost energy through interaction with the sample. (c) Conventional TEM with a magnetic prism spectrometer below the viewing screen.

Fig.1.28 Electron energy loss spectroscopy (EELS) of carbon material: the carbon K-edge, corresponding to the excitation of an electron of the K-shell is measured at 284eV and beyond. Due to the high energy resolution of this type of spectrometry, the features beyond this threshold can also be analyzed and give information on the bonding state of the excited atom.

Chapter 2

Figure 2.1 GNP morphology characterization: (A) low magnification TEM, (B) high resolution TEM images of GNP surface and (C) SEM image.

Figure 2.2 GNP-CNTs morphology characterization: (A) TEM of hybrids (The bright arrow shows the GNP), (B) high resolution TEM images of CNT (microscope and conditions) and (C) SEM image (The bright arrow shows the GNP).

Figure 2.3 GO morphology characterization: (A) TEM image; (B) A selected area (SA) diffraction pattern of the GO taken on the red spot in (A); and (C) SEM image.

Figure 2.4 SEM images showing the CF morphology: (A) original CFs; (B) desized CFs; (C) CNT-grafted CFs; and (D) CNT-CF to measure the thickness of the CNT layer.

Figure 2.5 The thermogravimetric analysis (The black line) and the differential thermogravimetric (The red line) (TGA/DTG) curves of CNT-CFs.

Figure 2.6 TGA curves of GNPs and CNT-GNPs.

Figure 2.7 XPS spectra of the C1s region scan for (A) raw CFs, (B) desized CFs, (C) CNT-CFs and (D) oxidized CNT-CFs.

Figure 2.8 XPS spectra of the survey of (A) original CFs and (B) desized CFs.

Figure 2.9 C1s XPS spectra of (A) original GNPs, (B) O-GNPs and (C) GOs.

Figure 2.10 (A) Fourier-Transform infra-red (FT-IR) curve of GOs; the inserted image is a view of the GOs dispersed in ethanol by ultrasonication; (B) Raman spectra of GNPs and GOs

Chapter 3

Figure 3.1 The preparation of the sample for micro-tensile test: (A) The polished surface containing several CFs which are marked out by red circles; (B) A Pt protection is deposited on the CF/epoxy interface with a dimension of $20\mu\text{m}\times 2\mu\text{m}\times 1\mu\text{m}$, and the red circle indicates the position of the targeted CF; (C) The tensile sample is milled down to a thickness of $1\mu\text{m}$, with a width of $8\mu\text{m}$; (D) the lamella is lifted out by the manipulator and soldered to the copper grid edge by Pt deposition; (E) Two quarter-circles are conducted on the interface to avoid the stress concentration; (F) The manipulator is welded to the lamella by depositing a Pt layer, the red arrow indicates the loading direction.

Figure 3.2 Typical tensile specimen, showing a reduced gage section and enlarged shoulders.

Figure 3.3 A schematic illustration of a representative tensile sample for the fiber and epoxy matrix.

Figure 3.4 Calculated shear (σ_{xy}) and tensile stress (σ_{xx}) distribution along the samples with different R/W ratio: (A) $R/W=\infty$; (B) $R/W=0.5$; (C) $R/W=1.0$; (D) $R/W=2.0$. (The red rectangular in each sample shows the enlarged stress distribution image.)

Figure 3.5 (A) The sketch of a tensile specimen to measure the interfacial strength between the CF and epoxy matrix; (B) SEM image of final tensile specimen prepared by FIB-SEM.

Figure 3.6 Fracture position during the tensile test: (A) at the interface, (B) in the epoxy matrix and (C) at the connection point.

Figure 3.7 Stretching process of a raw CF/epoxy composite sample observed by SEM with two series (A) Electron and (B) Ion images; (C) Strain-step curves during the stretching process, data extracted from two series of images; (D) Sketch of the global sample position, with regard to the stretching direction and the two beam sources.

Figure 3.8 (A) Displacement-tensile step plot of stretching samples extracted from ionic images. The black, red, green and blue lines are the results from the raw CF/epoxy, desized CF/epoxy, CNT-CFs/epoxy and oxidized CNT-CFs/epoxy, respectively. (B) Fracture strengths of the raw CF/epoxy, desized CF/epoxy, CNT-CF/epoxy and oxidized CNT-CF/epoxy.

Figure 3.9 Stress-strain values of pure epoxy matrix by tensile test.

Figure 3.10 Detailed size value of a GNP/epoxy tensile sample.

Figure 3.11 (A) Sample without stretching; (B) after failure.

Figure 3.12 TEM lamellae prepared by FIB (A) raw CNT-CFs/epoxy, (B) desized CNT-CFs/epoxy, (C) CNT-CFs/epoxy and (D) oxidized CNT-CFs/epoxy.

Figure 3.13 STEM Z-contrast (HAADF) image showing the interface region of the CF and epoxy: (A) raw CF/epoxy and (B) CNT-CF/epoxy interfaces.

Figure 3.14 High magnification STEM Z-contrast (HAADF) image showing a CF perpendicular to the epoxy foil prepared by FIB: Interfaces of (A) Raw CF/epoxy, (B) Desized CF/epoxy, (C) CNT-CF/epoxy and (D) Modified CNT-CF/epoxy, respectively. The regions marked out by the green rectangle were analyzed by EDX, the elements were marked out by different colors, green for oxygen, blue for carbon, pink for chlorine and red for iron, respectively.

Chapter 4

Figure 4.1 Three-roll milling method process to prepare the epoxy composites with graphene-based nanofillers.

Figure 4.2 TEM sample preparation procedures by FIB.

Figure 4.3 Fracture surface of G/epoxy composites with a weight fraction of 4 %, (A) GNP/epoxy, (B) GO/epoxy, (C) O-GNP/epoxy and (D) CNT-GNP/epoxy, respectively.

Figure 4.4 Dynamic mechanical modulus E' and loss tangent ($\tan \delta$) versus temperature of 4 wt% G/epoxy composites compared to pure epoxy.

Figure 4.5 Frequency dependence of Alternating Current (AC) conductivity for the 4 wt% G/epoxy composites compared with pure epoxy.

Figure 4.6 the integrals and energies involved in measuring the low energy region of the loss spectrum.

Figure 4.7 (A) Low-loss spectra of epoxy matrix; (B) Peak positions extracted out from low-loss spectra of three different samples as a function of sample thickness (measurements in the epoxy matrix part only).

Figure 4.8 (A) region selected for electron beam irradiation at 80 keV, the red circle indicates the area and is controlled by the aperture II; (B) Related core-loss spectra with different time exposures.

Figure 4.9 HAADF-STEM images of (A) GNP/epoxy, (B) GO/epoxy and (C) CNT-GNP/epoxy composites; Tables (D-F) show the thickness values of each point measured in images (A-C), respectively.

Figure 4.10 (A) Energy-loss spectra in the C K-edge, N K-edge and O-K edge ranges with different sample thicknesses; (B) Enlarged C K-edge marked out with the red rectangle in (A).

Figure 4.11 HAADF-STEM images of (A) GNP/epoxy, (B) GO/epoxy and (C) CNT-GNP/epoxy composites. (D-F) Corresponding plasmon peak measurements. (G-I) Corresponding core loss spectra. (J-L) Corresponding C K-edges.

Figure 4.12 A scheme of the cross-section of CNT-GNP/epoxy sample where the electron beam pass through the MWCNT region.

Figure 4.13 High magnification STEM Z-contrast (HAADF) image showing the nanofillers in the epoxy matrix: (A) GNP/epoxy, (B) O-GNP/epoxy, (C) GO/epoxy and GNP-CNT/epoxy composites. The regions marked out by green rectangular in (A) and (B) and the entire region in (C) were analyzed by energy dispersive X-ray spectroscopy (EDX), the elements were marked out by different colors, green for oxygen, yellow for carbon, and blue for iron, respectively.

Chapter 5

Figure 5.1 SEM images of (A) the GNP/epoxy and (B) the GO/epoxy composite fractured surface with 1.0 % weight fraction. Overview of STEM Z-contrast image showing: (C) a GNP plane perpendicular to the epoxy foil prepared by FIB, (E) the GO/epoxy sample. (D) and (F) show higher magnification Z-contrast images of the framed regions in (C) and (E), respectively. EELS analyses were carried out along the lines indicated on these images.

Figure 5.2 (A) Carbon core-loss and (B) low-loss spectra acquired from the epoxy matrix, a GNP and a GO, respectively.

Figure 5.3 the peak positions extracted from the low energy-loss spectra acquired from Figure 5.1(D) and (F), shown as a function of the acquisition order from point 1 to point 100: (A) for line 1 in Figure 5.1(D); (B) for line 2 in Figure 5.1(D); (D) for line 1 in Figure 5.1(F); (E) for line 2 in Figure 5.1(F); three lines parallel to the interface in each images showed the low energy-loss spectra acquisition from three regions, GNPs, epoxy in interphase region and epoxy matrix; the numbers indicate the acquisition order during experiment, point 1 to point

30 for line 3, point 31 to point 60 for line 4 and point 61 to point 90 for line 5, respectively; (C) 90 peak position values of low energy loss spectra from Figure 5.1(D); (F) 90 peak position values of low energy loss spectra from Figure 5.1(F). The inserted images indicate the acquisition position for each spectrum.

Figure 5.4 Schematic representation of a composite interphase: (A) GNP/epoxy, (B) GO/epoxy; modulus variation in the interphase: (C) GNP/epoxy and (D) GO/epoxy.

Appendix I

Figure 1 Illustration of the stretching method used in this work.

Figure 2 SEM images of (A) Original GNPs, (B) GNPs deposited on PMMA surface by spray, (C) PMMA surface after separation from the PVA (the contact area), (D) PVA surface after separation from the PMMA (the contact area). (E) Optical image of the PVA surface after separation by stretching (1000X), (F) Optical image of the PVA surface processed by ImageJ to calculate the GNP covered density (1000X).

Figure 3 Statistical analysis of the mean IFSS as a function of the GNP covered area.

Chapter 1

Table 1.1 properties of some commercial CFs.

Table 1.2 A brief record of graphene-reinforced epoxy nanocomposites studied for the improvement of mechanical and thermal properties.

Table 1.3 Comparison of two typical methods for preparation of TEM samples.

Chapter 2

Table 2.1 Materials for experiments.

Chapter 3

Table 3.1 Elongation and tensile strength at break and Young's modulus of single fiber tests for four types of CFs. 30 samples were measured for each kind of fiber. Evaluation of the interfacial shear strength (IFSS) of different CFs in the composites.

Table 3.2 The physical properties of CFs and epoxy used for simulation.

Chapter 4

Table 4.1 The thickness influence on the O/C and N/C ratios in the epoxy matrix.

Appendix II

Table The peak positions values of Figure 5.3

Chapter 1 Background and introduction

Introduction

In this chapter, I review the background of carbon-based materials, including fabrication, surface modification, influence on the properties of composites, etc. Recent developments on the interface study are also introduced for a better understanding of the structure-properties relationship. Meanwhile, I also review the techniques used for the interface study, i.e. microscopy and related analysis methods.

1.1 Carbon-based materials and surface modification

In recent decades, carbon-based reinforcements such as carbon nanotubes (CNTs), graphene and carbon fibers (CFs) play a major role due to their special structural properties along with their excellent physical or chemical properties. They offer a wide range of applications in many fields. This part reviews the structures and properties of graphene and CFs along with their surface modification methods.

1.1.1 Carbon fibers (CFs)

Carbon fibers (CFs), which contain at least 92 wt% of carbon in composition, integrate high-performance and rich functionalities [1, 2]. Their creation can be traced back to 1883, when Sir Joseph Swan conducted the pyrolysis of natural cellulose fibers for electrical-light bulbs. After the Royal Aircraft Establishment and Rolls Royce, Ltd, promoted a high-performance fiber with 1.7 GPa in mechanical strength and 400 GPa in tensile modulus in the 1960s, CFs became widely attractive [3, 4]. They are now fabricated from many different types of precursors, such as polyacrylonitrile (PAN), pitch, rayon, polyesters and polyamides, by carbonization and/or graphitization at high temperatures to eliminate other chemical elements and generate graphitic structures, as shown in **Figure 1.1**. Thousands of CFs with diameters ranging from 4 to 15 μm are bundled together to form a tow, which may be used to produce high-performance materials as it is or in other forms (e.g. fabrics). They have been widely used in aerospace, nuclear engineering and sport industries, benefiting from their excellent properties, such as high tensile strength and stiffness, low densities, a high thermal stability and a favorable electrical conductivity [7].

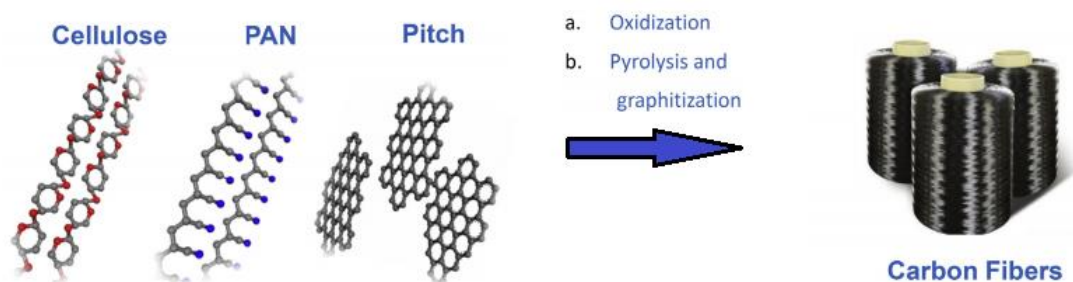


Figure 1.1 Precursor system of conventional carbon fibers (CFs). Oxidation crosslinking and pyrolysis (and/or graphitization) are used to fabricate conventional CFs from cellulose,

polyacrylonitrile (PAN) and mesophase pitch precursors. The polycrystalline graphitic structure of CFs is generated from these precursor macromolecules [1].

1.1.1.1 Carbon fiber structure and properties

Compared to other allotropic forms of carbon materials, such as graphite and diamond, the structure of CFs is very complex [8]. The structure of CFs was first characterized by X-ray diffraction, which identified the preferred orientation of layers of hexagonal carbon rings along the fiber axis with a crystallite size of several nanometers [9]. The crystallite size of CFs and their orientation largely depend on the heat treatment temperature. In detail, a higher temperature leads to a larger crystallite size and a higher orientation state. The major structure proposed for CFs is the so-called *turbostratic* structure, as shown in **Figure 1.2**, which is composed of more or less bent layers with sp^2 -hybridized carbon atoms. Although the interplanar distance is about 0.34 nm, and similar to that of graphite, there is no ABAB stacking sequence order [6].

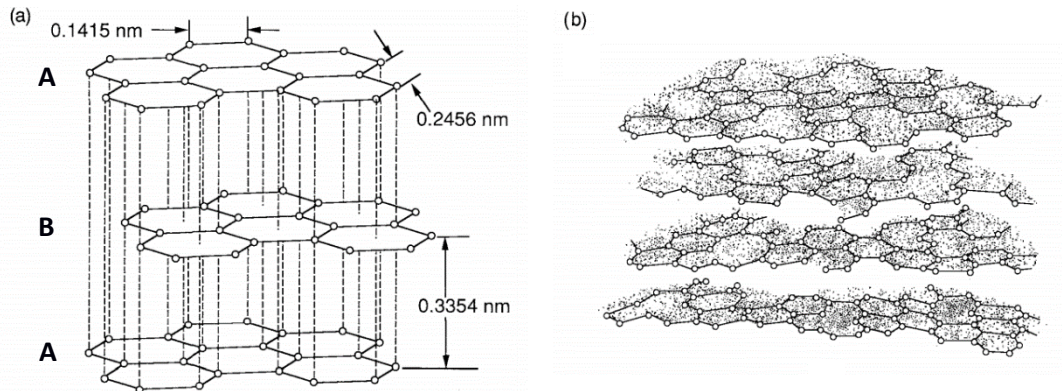


Figure 1.2 (a) Crystal structure of graphite representing the ABAB stacking sequence; (b) Turbostratic structure of CFs [10].

The microstructures of PAN- and pitch-based CFs are rather different. PAN-based CFs are fibrillar in nature, with highly ordered graphite planes in the circumcircle surface and a low order in the center. This special structure endows varied moduli throughout the CF cross-

section. Johnson *et al.* [11] developed a three-dimensional schematic representation of the microstructure of PAN-based CFs shown in **Figure 1.3(a)**. High-modulus pitch-based CFs exhibit a higher orientation than PAN-based CFs. The transverse texture of early commercial mesophase CFs was either radial or flat-layered, as shown in **Figure 1.3(b)**. These initial mesophase pitch-based CFs with radial and flat-layered transverse textures readily developed three-dimensional crystallinity. Although this structure made pitch-based CFs more flaw-sensitive than PAN-based CFs with their more random, fibril structure, it gave them superior lattice-dependent properties [12].

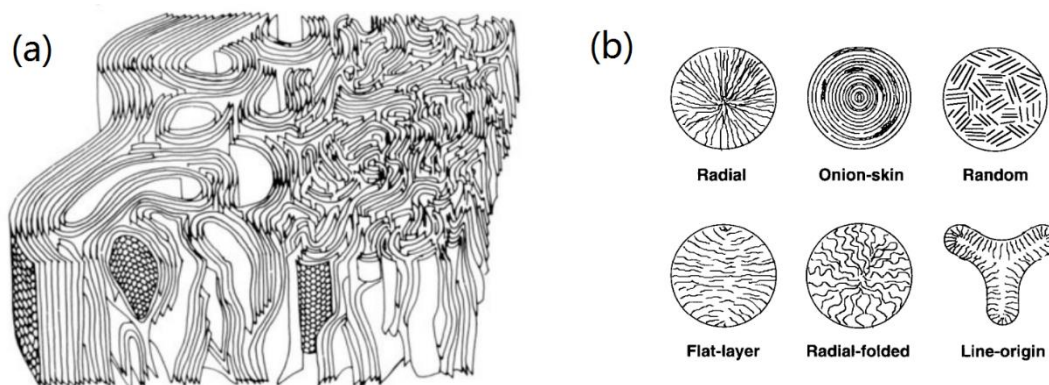


Figure 1.3 (a) Schematic three-dimensional model of PAN-based CFs [11]; (b) Transverse textures of mesophase pitch-based CFs [12].

Today, more than 90% of commercial CFs are made from PAN, and the rest are made from pitch. PAN-based CFs normally have tensile moduli ranging from 200 to 350 GPa, tensile strengths in the range of 3 to 7 GPa, compressive strength up to 3 GPa, electrical and thermal conductivities up to 10^5 S/m and 14 W/mK, respectively. In comparison, the modulus of pitch-based CFs can reach a higher level when compared to PAN-based CFs, and is around 960 GPa. Furthermore, pitch-based CFs have better electrical and thermal conductivities, which can reach 10^6 S/m and 10^3 W/mK, respectively. However, the tensile and compressive strengths of pitch-based CFs are lower than those of PAN-based CFs. In **table 1.1**, we listed the properties of some commercial CFs [13].

Table 1.1 properties of some commercial CFs [13].

Fibers	Tensile strength (GPa)	Tensile modulus (GPa)	Compressive strength (GPa)	Density (g/cm ³)	Thermal conductivity (W/mK)	Electrical conductivity (10 ⁴ S/m)	
AS4	4.27	228	-	1.79	-	6.5	
IM8	5.58	304	-	1.79	-	-	
T300	3.75	231	-	1.76	8	5.56	
PAN-based	T650/30	4.28	255	-	1.77	14	6.67
	T300	3.53	230	2.88	1.76	-	-
	T1000G	6.37	294	-	1.80	-	7.14
	M55J	4.02	540	0.9	1.91	-	12.5
	M60J	3.80	590	1.67	1.91	-	12.5
Pitch-based	P-25	1.38	159	1.15	1.90	22	7.69
	P-55S	1.90	379	0.85	1.90	120	11.8
	P-100S	2.41	758	0.48	2.16	520	40
	P-120S	2.41	827	0.45	2.17	640	45.5
	K-800X	2.34	896	-	2.20	900-1000	66.7-83.3
	K-1100	3.10	965	0.2	2.20	900-1100	76.9-90.9

1.1.1.2 Surface treatment of carbon fibers

Although CFs have excellent intrinsic properties for designing high performance composites, their surface is chemically inert, which leads to inadequate adhesion and hence weaker composite than the ideal one [14, 15]. It is essential to do proper surface treatment to develop their full potential in composites. There are several types of surface treatment methods for CFs, which could be classified into two categories, including an increase of the surface roughness by physical methods and an addition of reactive functional groups. Most of the methods bring both improvements simultaneously [16-18]. Various surface treatment methods have been reported to improve the adhesion between the CFs and the polymer matrix, as shown in **Figure 1.4**. Among them, the gas treatment method, the plasma treatment method and the wet chemical method are used to add reactive functional groups on the CF surface.

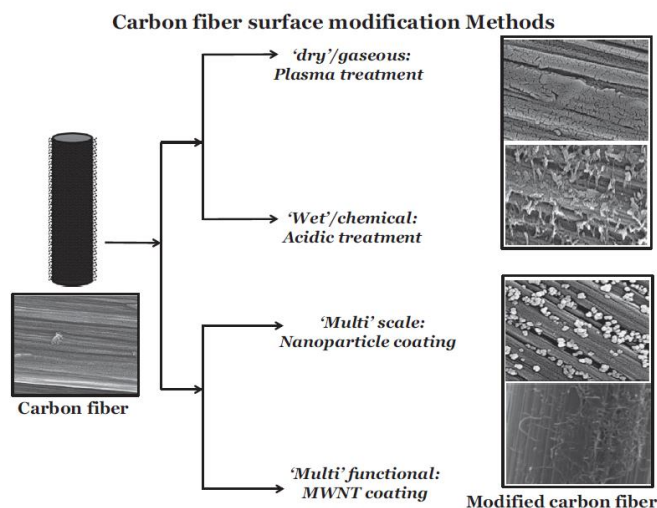


Figure 1.4 Schematic for the techniques for surface modifications. Field emission scanning electron microscope (FEG-SEM) or scanning electron microscope (SEM) images show CF surfaces [19].

The gas treatment methods are normally performed with air, oxygen and CO₂ at low or elevated temperatures. Herrick *et al.* [20] treated rayon-based CFs in air at 500 °C for 16 h to slightly improve the interlamellar shear strength (ILSS). The ILSS was increased by 45 % when the temperature was raised to 600 °C, although it was accompanied by a serious weight loss. Scola *et al.* [21] treated the CFs for 60 s in N₂ mixed with 0.1-1.8% O₂ at 1000-1500 °C to improve their bonding characteristics to a resin. There was no significant degradation of the CF mechanical properties. Dai *et al.* [7] studied the effect of heat treatment on the CF surface properties and the CF/epoxy interfacial adhesion. Three sets of T300B CFs was heated in a vacuum drying chamber at three different temperatures (150 °C, 180 °C and 200 °C) for several hours using controlled processing cycles. It demonstrated that the content of activated carbon atoms (conjunction with oxygen, nitrogen and hydroxyl) on the treated CF surface and the polar surface energy decreased with the heat treatment temperature. Compared with the untreated CFs, the wettability studied with the dynamic contact angle test between CFs and an E51 epoxy resin became worse. Results of micro-droplet tests demonstrated that the IFSS of T300B/epoxy was reduced after the heat treatment process. This was attributed to a decreased amount of reactive functional groups in the interfacial region.

Plasma treatment¹ has become a popular method to improve the CF-matrix adhesion in recent years. The principle of a such treatment is the formation of active species in a gas induced by a suitable energy transfer. Typical gases used to create a plasma include air, oxygen, ammonia, nitrogen and argon. Erden *et al.* [32] used continuous atmospheric plasma oxidation (APO) to introduce oxygen functionalities on the surface of CFs in order to improve their adhesion to a surrounding polyamide-12 (PA-12). After the APO treatment, CFs became more hydrophilic due to the introduction of polar oxygen-containing groups on the CF surface, which also resulted in an increase of the CF surface energy. The CF tensile strength remained unaffected. The IFSS between CFs and PA-12 increased from 40 to 83 MPa with up to 4 min of APO treatment. This improvement can be attributed to an increase of the surface oxygen content from 7 at.% to 16 at.%, which yielded more hydrogen bonds between the CFs and the PA-12 matrix. Many liquid-phase oxidizing agents (e.g. nitric acid, acidic potassium permanganate, acidic potassium dichromate, hydrogen peroxide and ammonium bicarbonate) have also been used to treat CF surfaces. These liquid-phase treatments do not cause excessive pitting and hence degradation of the CF strength [33]. Anodic oxidation is most widely used for the treatment of commercial CFs since it is fast, uniform and suits mass production. CFs act as an anode in a suitable electrolyte bath. A potential is applied to the CF to liberate oxygen on the surface. Typical electrolytes include nitric acid, sulfuric acid, sodium chloride, potassium nitrate, sodium hydroxide, ammonium hydroxide and so on.

Non-oxidative methods, including the deposition of an active form of carbon, plasma polymerization and grafting of polymers onto the fiber surface [37] have been used for CF surface treatments.

Whiskerization *et al.* [38] involved the growth of thin and high strength single crystals, such as silicon carbide (SiC), silicon nitride (Si₃N₄) and titanium dioxide (TiO₂) at right angles to the fiber surface.

Many polymerizable organic vapors are used for plasma polymerization processes, such as polyamide, polyimide, organosilanes, propylene, and styrene monomers. Plasma polymerization has demonstrated its ability to increase the polar component of the surface free energy of CFs.

¹ A plasma is a partially or fully ionized gas containing electrons, radicals, ions and neutral atoms or molecules.

The sizing of CFs refers to the coating of organic materials applied to the CF surface during the manufacture. Sizing is reputed to protect the CF surface from damage during subsequent textile processing, to aid in handling, to provide a chemical link between the CF surface and the matrix and thus to improve the fiber-matrix adhesion [43].

Sizing can be achieved by deposition of polymers from solutions onto the CF surface. The CFs pass through a sizing bath filled with organic solutions. The choice of sizing materials depends on the CF type and the matrix resin. They must be compatible with the matrix resin, which allows the resin to penetrate the CF bundle and interact with the CF surface. Typical sizing materials include epoxy, urethane, polyester and others. The sizing amount is 0.5-1.5 wt% of the CF and the sizing layer is hundreds of nanometers thick [44].

Drzal *et al.* [45] have studied the effect of sizing on the adhesion of CFs to an epoxy matrix. They found that the sizing layer created a brittle interfacial layer between the CF and the matrix, which improved the IFSS.

Dai *et al.* [46] have investigated the influence of sizing on the CF/matrix interfacial adhesion by comparing sized and desized T300B and T700SC CFs. They found that the desized CFs presented a lower concentration of activated carbon atoms (conjunction with oxygen and nitrogen) and a lower polar surface energy, but higher dispersive surface energy and IFSS. The sizing agent on T300B and T700SC CF surface had a negative effect on the interfacial bonding. This is contrary to the general principles. Desizing reduced the acid parameter of CFs surface which promoted the bonding strength at the fiber/epoxy interface. The IFSS of T300B/epoxy increased from 63.72 MPa to 87.77 MPa after desizing, with an improvement of 38%. This was attributed to an increment of adhesion work. The IFSS of desized T700SC/epoxy (89.39 MPa) was 9 % greater than that of T700SC/epoxy (81.74 MPa). A thicker sizing may result in a weaker layer in the interface. They concluded that IFSS for CF/epoxy systems depended not only on the chemical bonding but also on the physical and adhesive interactions.

1.1.2 Graphene and graphite nano-platelets (GNPs)

Graphene is a one atom-thick, two-dimensional sheet composed of sp^2 carbon atoms, arranged in a hexagonal lattice (**Figure 1.5 left**). Studies of single layered graphene became possible with the development by Novoselov and Geim in 2004 [47] , who used the "scotch-tape method" to produce large isolated graphene sheets from graphite and were awarded the Noble prize in 2010 (**Figure 1.5 right**). The electron energy band structure is approaching to

its three-dimensional limit when the number of graphite is within 10 layers. Hence, the graphite, which has less than 10 layers, is defined as graphene. Because of the unique properties of graphene, the research about graphene grows extremely fast around the world [48].

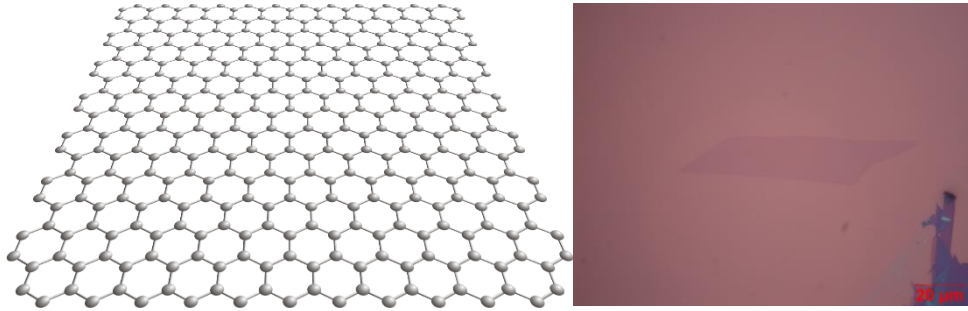


Figure 1.5 (left) Structure of graphene; (right) Single layer graphene pieces placed on SiO₂ wafer prepared by “scotch-tape method”.

1.1.2.1 Graphene properties

Graphene has many unique properties so as to draw such a high research interest in the mechanical, electrical, thermal and gas barrier fields [49].

The mechanical properties of graphene, including the Young's modulus and fracture strength, have been intensively investigated by computational and experimental methods . Atomic force microscopy (AFM) has been used to investigate the Young's modulus of few-layer graphene by suspending it over trenches (as shown in **Figure 1.6**). Circular membranes of this sample were pressed by AFM tips to measure the elastic properties and intrinsic breaking strength. It was reported that the defect-free graphene has a Young's modulus of 1.0 TPa and a fracture strength of 130 GPa [52, 53]. and is consistent with what is reported in literature since long ago. The chemical modified graphene was also tested by a similar AFM indentation method, which exhibited a mean elastic modulus of 0.25 TPa with a standard deviation of 0.15 TPa [54].

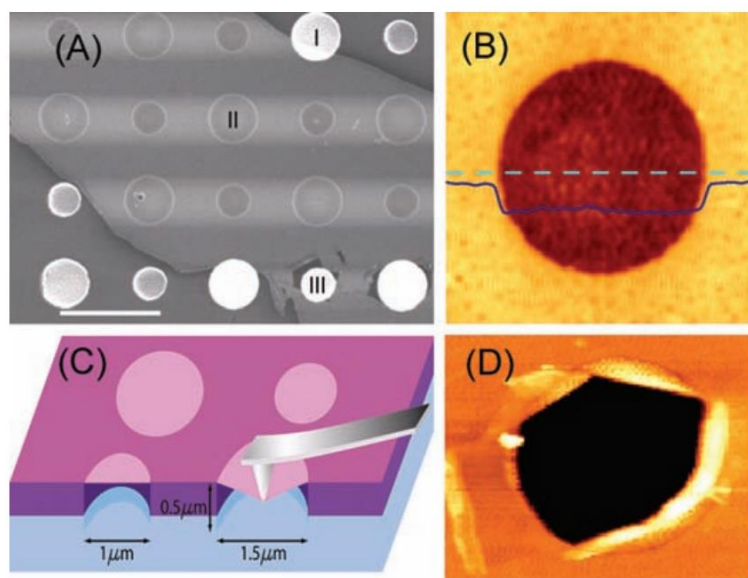


Figure 1.6 (A) Scanning electron microscopy (SEM) image of a graphene flake spanning an array of circular holes (scale bar, 3 μm); (B) Noncontact mode AFM image of one membrane, 1.5 μm in diameter. The solid blue line is a height profile along the dashed line. The step height at the edge of the membrane is around 2.5 nm; (C) Schematic illustration of nanoindentation on membranes; (D) AFM image of a fractured membrane [52].

As a potential alternative of semi-metal, graphene displays an ambipolar electric field effect and charge carriers can be tuned continuously between electrons and holes in concentrations as high as 10^{13} cm^{-2} , with room temperature mobilities of up to $15\,000 \text{ cm}^2\text{V}^{-1}\text{s}^{-1}$ [47]. Moreover, the observed mobilities depend weakly on temperature, suggesting that an ultrahigh mobility could be realized in graphene at room temperature. By minimizing the impurity scattering, mobilities exceeding $200\,000 \text{ cm}^2\text{V}^{-1}\text{s}^{-1}$ were achieved in suspended graphene [55].

Graphene has been developed intensively for its use in electronic devices, where thermal properties are a crucial factor for their performance and reliability. The amount of heat generated during the device operation needs to be dissipated. Carbon-based materials have shown higher thermal conductivities due to strong C-C covalent bonds and phonon scattering, such as 3000 W/mK for multi-walled carbon nanotubes (MWCNTs) at room temperature [56] and 3500 W/mK for single-walled carbon nanotubes (SWCNTs) [57]. However, large thermal contact resistance in CNT-based semiconductors limited their application. Recently, pure

defect-free graphene has been reported to have the highest room temperature thermal conductivity of 5000 W/mK [58]. The thermal conductivity of graphene on various supports have also been predicted by Klemens [59]. Confocal micro-Raman spectroscopy has been developed to determine the thermal conductivity of graphene, as shown in **Figure 1.7**. A suspended graphene layer was heated in the center by a laser light with a spot size of 0.5-1.0 μm . The heat generated in single layer graphene has to escape by propagating laterally through the extremely thin graphene layer. The temperature change was determined by measuring the shift in the graphene G peak using confocal micro-Raman spectroscopy [60].

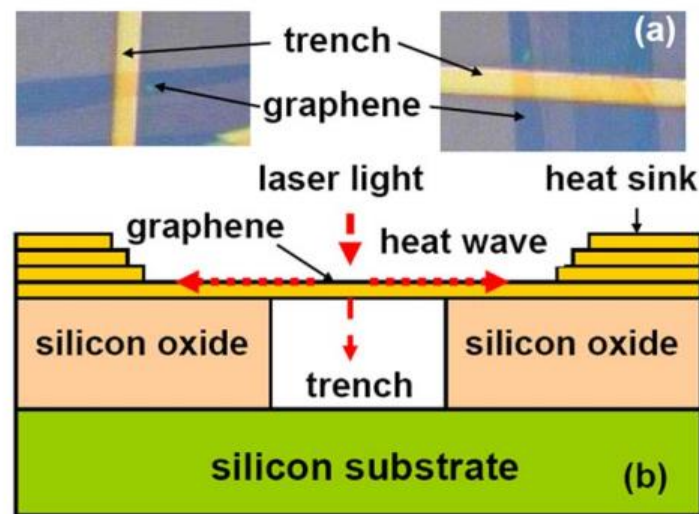


Figure 1.7 Schematic of the experimental setup for measuring the thermal conductivity of graphene by confocal micro-Raman spectroscopy [60].

Graphene has also good optical properties: it is transparent over a broad wavelength range and absorbs 2.3% of incident light. When considering graphite stackings, the absorption of light was found to increase with the number of layers, as shown in **Figure 1.8**.

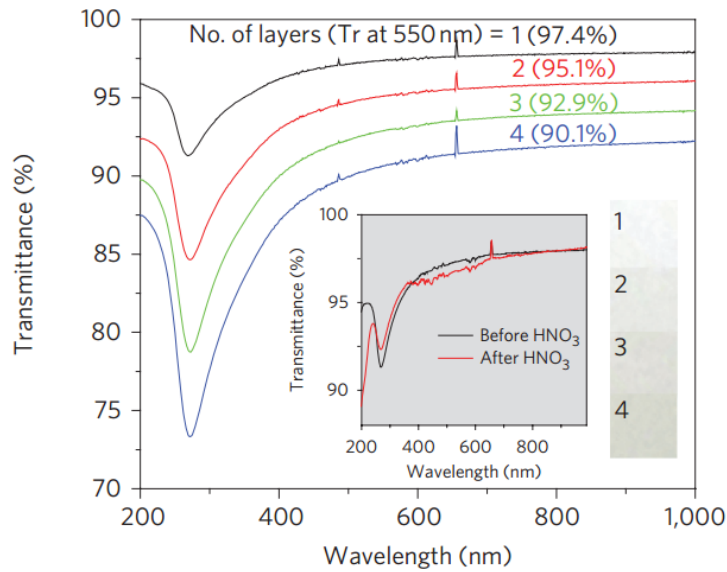


Figure 1.8 UV-visible spectra of roll-to-roll layer-by-layer transferred graphite and graphene films on quartz substrates [62].

1.1.2.2 Graphene synthesis

To benefit from the excellent properties of graphene, one of the foremost challenges is to produce sufficient amounts of high-quality graphene sheets. In recent years, numerous methods have been reported for synthesizing graphene, which can be grouped into three categories: mechanical cleavage, chemical vapor deposition (CVD) and chemical methods, as shown in **Figure 1.9**.

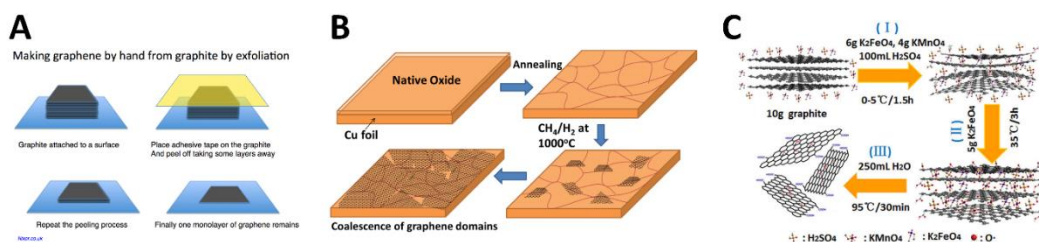


Figure 1.9 Three typical graphene preparation methods: (A) mechanical cleavage method; (B) CVD methods [63] and (C) chemical oxidation-reduction method [64].

Geim *et al.* [47] reported mechanical cleavage first by peeling graphene off from graphite flakes using Scotch tape, because of the weak interlayer energy of 2 eV/nm. The presence of graphene was optically identified by transferring it to a silicon dioxide layer on Si [65]. The method involved manual searching for single layer graphene among a myriad of multilayered flakes, and after likely specimens were identified with the optical microscope, conclusive evidence of their thicknesses was provided by AFM [66] and Raman techniques [67]. Hence, the yields of graphene by this approach are extremely low due to the manual operation.

Chemical vapor deposition (CVD) is a popular method to synthesize graphene with few defects. In CVD methods, graphene is grown on a transition metal substrate via saturation of carbon upon exposure to a hydrocarbon gas at a high temperature. Ni or Cu films are typically used as the substrate. When the substrate is cooled, the solubility of carbon on the substrate decreases and the carbon precipitates to form graphene or multilayered graphite sheets. The major advantage of the CVD approach is the production of graphene having less structural and electronic disorder or defects. However, the substrate material is very expensive, limiting considerably its application for large-scale production.

The most promising method for large-scale producing graphene is the "oxidation-reduction" methods. Due to the spaces between graphene layers in graphite, intercalating agents can reside between the graphene layers under chemical reactions, forming graphite intercalation compounds (GICs). The interlayer spacing of GIC can increase from 0.34 nm to more than 1 nm depending on the intercalant, leading to a significant reduction in the van der Waals forces between adjacent sheets. The decrease in van der Waals forces makes them much easier to be further exfoliated, offering a possible route to fabricate graphene [69]. The interlayer spacing in GICs can be expanded by thermal shock to produce expanded graphite.

Producing graphene in large scale is very difficult. For practical use, the graphite nanoplatelets (GNPs) have attracted enormous attention. GNPs are exfoliated from graphite by rapid heating and pulverization, to produce the platelets with thickness 2-10nm, with different lateral sizes (see **Figure 1.10**). Although GNPs are a state of aggregation of graphene, it can still provide excellent conductivity and good mechanical reinforcement. The reason is that GNPs have a large lateral size, therefore high aspect ratios are still achieved.

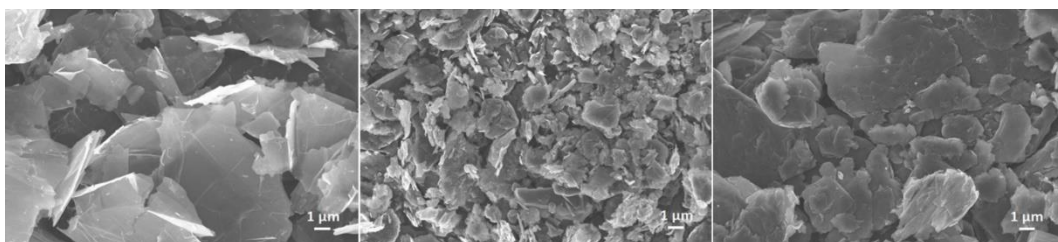


Figure 1.10 SEM images of GNPs with different thickness and lateral sizes.

1.1.2.3 Surface modification of graphene

To achieve requirements for different applications, a surface modification of graphene has been developed extensively. Graphene oxide (GO) is one of the most studied graphene derivative nanoparticles [82]. GO is electrically insulating with good dispersability in water and many polar organic solvents, which makes it of interest in the production of polymer nanocomposites. **Figure 1.11** shows various covalent functionalization methods of graphene or GO.

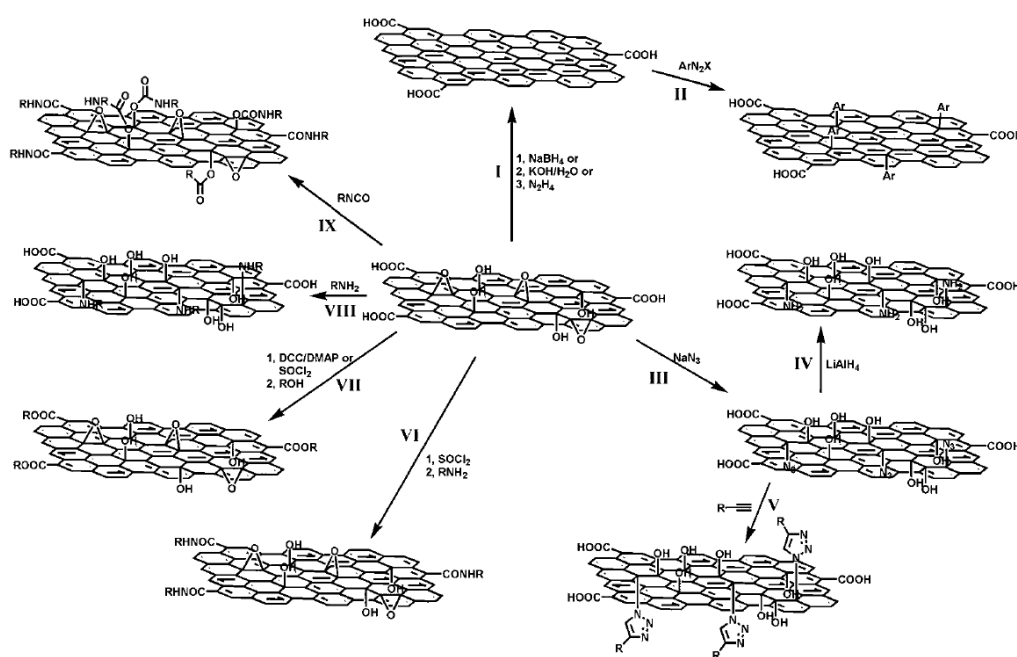


Figure 1.11 Schematic representation showing various covalent functionalization chemistry of graphene or GO. I: Reduction of GO into graphene. II: Covalent surface functionalization via diazonium reaction (ArN_2X). III: Functionalization of GO with sodium azide. IV: Reduction of azide functionalized GO with LiAlH_4 . V: Functionalization of azide functionalized GO

through click chemistry (R–ChCH/CuSO₄). VI: Modification of GO with long alkyl chains by the acylation reaction. VII: Esterification of GO VIII: Nucleophilic ring-opening reaction of GO. IX: Functionalization of GO with organic isocyanates [83].

After oxidation by a strong acid, the graphene surface has been introduced to several types of oxygen-containing groups, such as carboxyl, hydroxyl and epoxy group [84]. These functional groups help to facilitate the grafting of other molecules.

Acylation reactions are the most common approaches used for linking molecular moieties at the edges of GO [85, 86]. Reaction VI in **Figure 1.11** indicates the reaction between carboxyl acid groups and octadecylamine, which is used to modify GO by long alkyl chains [87]. Also, by using acylation methods, the carboxylic groups can be tethered to amine-functionalized molecules. For example, PEG-NH₂ was grafted onto GO to be used in a drug delivery system [88].

As we showed in reaction VII in **Figure 1.11**, the carbodiimide-activated esterification reaction could also happen between the carboxyl groups on the graphene sheets and hydroxyl groups of the polymers. Hence, a widely range of polymer chains could be grafted onto GO, such as poly(vinyl alcohol) [89], 4-(dimethylamino)-pyridine [90] and N-hydroxybenzotriazole [91], etc.

However, after oxidation, the intrinsic mechanical properties of GO are largely decreased, which may have a negative influence on the nanocomposites [91]. At the same time, the presence of the oxygen-containing groups destroys the π -conjugation, which leads to the insulation of GO.

In order to maintain the intrinsic electrical properties of graphene and extend the 2D plane into three-dimension, CNT-grafted graphene hybrids has attracted enormous attention in recent years . Zhu *et al.* [95] developed a method to bond graphene and SWCNTs seamlessly during the growth stage (**Figure 1.12**). The hybrid material exhibited a surface area of 42,000 m²/g with ohmic contact from the vertically aligned SWCNTs to the graphene and had great potential use in energy storage and nano-electronic technologies.

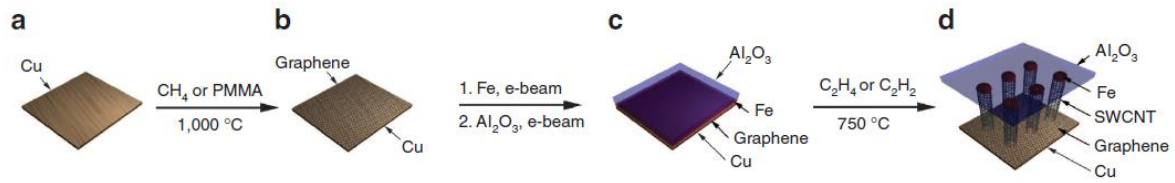


Figure 1.12 Sketch of the synthesis of CNT carpets directly from graphene [95].

Zhao *et al.* [96] synthesized a typical 1D-2D coupling graphite nanoplatelet-carbon nanotube hybrids (GCHs) structure using a catalyst chemical vapor disposition (CCVD) method. Then, the advanced graphite nanoplatelet-carbon nanotube hybrids/polydimethylsilicone (GCHs/PDMS) flexible composites have been prepared (**Figure 1.13**). The composite showed a significant increase of AC conductivity and excellent PR behavior.

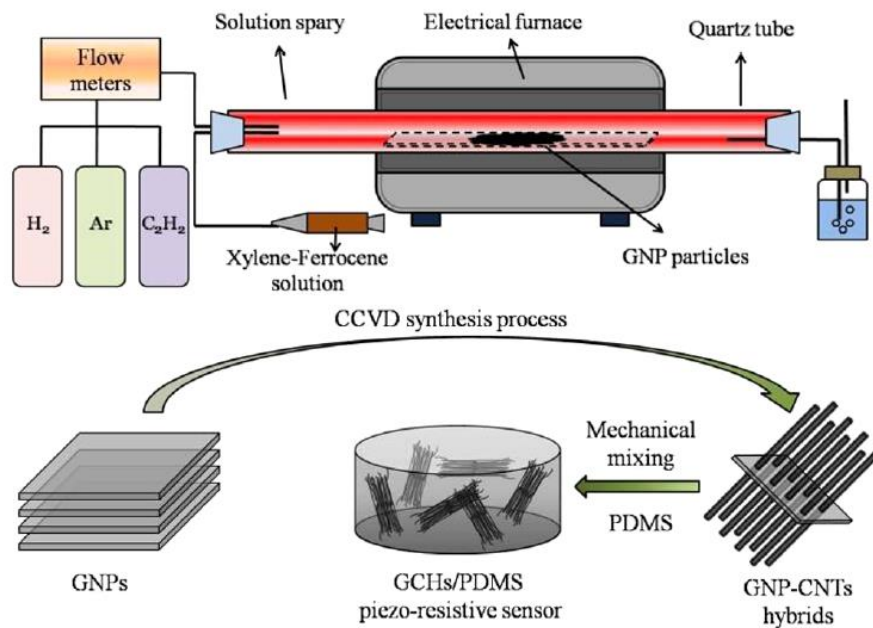


Figure 1.13 Schematic illustration of the preparation of the graphite nanoplatelet-carbon nanotube hybrids (GCHs) and the graphite nanoplatelet-carbon nanotube hybrids/polydimethylsilicone (GCHs/PDMS) composites [96].

1.2 Polymer composites

In the tendency of industry applications, the use of polymeric materials has increased largely due to its low cost, easy manufacturing and processing, low weight, etc. Among various types of polymers, the epoxy matrix draws tremendous attentions because of its superlative mechanical properties, thermal stability, solvent resistance and easy processing [100]. It is replacing lots of traditional materials due to its versatile nature. Epoxy resins are of various types (**Figure 1.14**). Trimethylol propane epoxy resin can be hardened at low-temperature. It is a non crystalline and a low viscosity plastic material [101]. The tetra-functional epoxy resin has a very high cross-linking density and is used as a high thermoresistance material [102]. Novolac epoxy resin also has a very high crosslinking density, which leads to excellent chemical, thermal and solvent resistance properties [103]. Cycloaliphatic epoxy resin has excellent UV stability, excellent electric properties, good thermal stability and good weather ability due to its aliphatic backbone with fully saturated molecular structure [104]. Bisphenol-A epoxy resin has adjustable properties which depend on the number of monomers. Molecules with a low molecular weight have a high viscosity and exist in the liquid state while those with a high molecular weight exist in the solid state [105].

These thermosetting resins can be hardened by using an extensive range of curing agents, which can be classified into amine-type curing agents, anhydride, catalytic and alkali type curing agents. The final properties of the epoxy matrix depend largely on the fraction and type of curing agents [106, 107]. The three-dimensional highly cross-linked networks are formed in epoxy resin curing systems. There are many trigger mechanism, including room temperature hardening, photo hardening and heat hardening. Usually, curing agents, such as aliphatic polyamines, low molecular weight polyamide, alicyclic polyamines and functionalized aromatic amines, take place at room temperature [108]. Heat hardeners are generally classified into two types: postcuring (at high temperature) and precuring (at low temperature) curing agents. These hardening agents are resol resins, aromatic polyamines, acid anhydrides, amino resins, hydrazide, etc. Irradiation by ultraviolet light, infrared light or an electron beam are named as photo-hardening. Comparing to other processes, photo-hardening is more rapid and reliable [109].

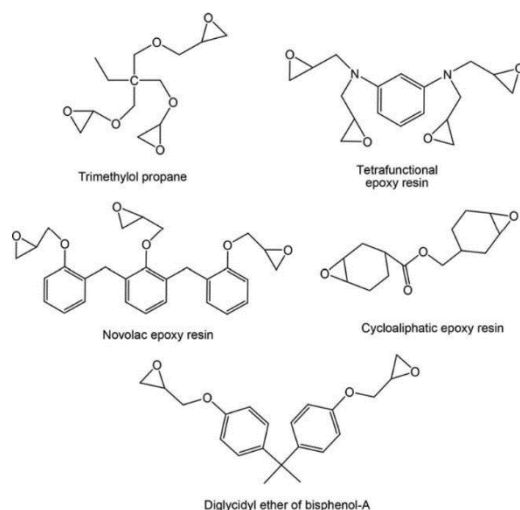


Figure 1.14 Different types of epoxy resins [110].

Many kinds of polymers have limited applications in engineering area due to their low fracture toughness and poor absolute strength. To overcome these disadvantages, polymers are often integrated with a variety of reinforcements, such as carbon black [111], clay [112], CNTs [113], metal oxide particles [114], CFs [115] and graphene [116]. Ever since the discovery of carbon materials, their significant properties, including excellent electrical, thermal and mechanical properties, have gathered a large attention. Such providential properties have endowed them as ideal candidates for polymer reinforcement. Polymer composites reinforced with GNPs, CFs and their derivatives are known to improve significantly their mechanical and other physical properties.

1.2.1 Graphene reinforced nanocomposites

Graphene has been found as a promising material for polymer composites because of its excellent thermal conductivity (above $3\,000\text{ WmK}^{-1}$), electron mobility of $2.5 \times 10^5\text{ cm}^2\text{V}^{-1}\text{s}^{-1}$ (theoretical limit $\sim 2 \times 10^5\text{ cm}^2\text{V}^{-1}\text{s}^{-1}$), and extremely thin thickness (one atom layer). The exploration of epoxy/graphene composites has increased dramatically in recent years.

1.2.1.1 Processing methods

To benefit from the excellent properties of graphene, it is crucial to homogeneously disperse graphene into the epoxy matrix. For epoxy and other kinds of polymer matrices, dispersion significantly depends on the processing methods. There are several commonly used

techniques for preparing graphene/epoxy nanocomposites, including solution mixing, epoxy impregnation and mechanical mixing [117].

Solvent processing is the simplest and most widely used method for processing graphene/epoxy nanocomposites. Usually, the functionalized graphene could be easily dispersed in various types of solvents, and then be mixed with the epoxy resin by ultrasonication. Afterward, the solvent is evaporated in controlled conditions. Wan *et al.* [118] dispersed silane-functionalized GO in acetone by sonication, mixed the solution with the epoxy resin followed by a ball milling process and finally removed acetone by heating the mixture at 80°C. The prepared nanocomposite showed enhanced mechanical and thermal properties at low GO concentration. Fand *et al.* [119] dispersed amine functionalized graphene in Dimethylformamide (DMF) solvent, which enhanced the interaction between the graphene and the epoxy matrix. The composites showed enhanced dissipation capacity for strain energy during fracture.

Resin impregnation is a recently discovered method for preparing polymer composites. Jia *et al.* [120] prepared 0.1 wt% graphene/epoxy composites by impregnation of epoxy resin into a 3D graphene-nickel foam. Then, the nickel template was etched and the polymer was cured. The final composites showed excellent fracture toughness. Moreover, the glass transition temperature T_g increased by 31°C compared to pure epoxy. Li *et al.* [121] used the impregnation methods to prepare 11.84 wt% epoxy/graphene composites (as shown in **Figure 1.15**). Due to the filtration process, the graphene could be aligned, and the final composites showed a remarkable improvement in thermal conductivity.

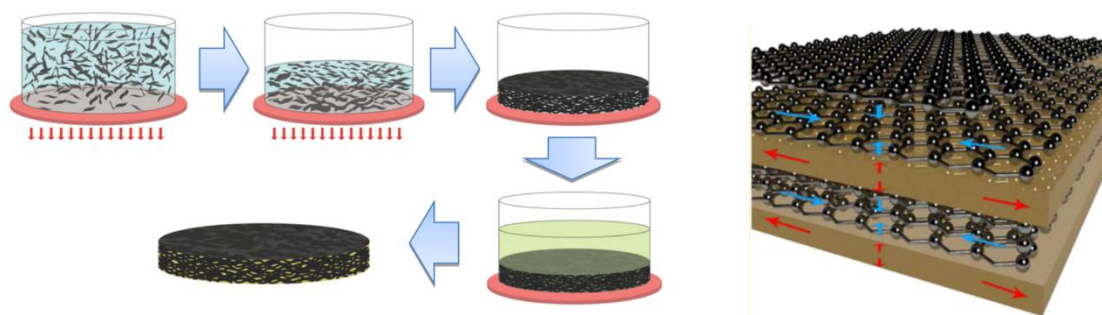


Figure 1.15 Schematic diagram of the preparation of aligned epoxy/graphene by impregnation method [121].

By using solvent processing and impregnation methods, the system cannot avoid the use of the solvent, which adds a supplementary stage to remove the solvent. Hence, the mechanical mixing is used extensively to avoid the influence of solvents. Among them, the 3-roll milling method is widely used to mix the graphene and the epoxy matrix. Chatterjee *et al.* [122] mixed GNPs and epoxy by 3-roll mill calendaring and studied the size and synergy effects of GNP- reinforced epoxy composites.

1.2.1.2 Properties

As previously mentioned, graphene has excellent physical and chemical properties. Thus, it is an ideal reinforcement for the improvement of properties of polymers and for the achievement of specific applications. In recent year, the development of graphene-reinforced polymer composites has been extensively studied and the major objective of most works on epoxy/graphene composites is to exploit the large mechanical reinforcement of the graphene coupled with other improvements, such as thermal conductivity [123], electrical conductivity [124], etc.

Table 1.2 A brief record of graphene-reinforced epoxy nanocomposites studied for the improvement of mechanical and thermal properties.

Reinforcement (fraction)	Dispersion method	Improvements	Ref.
GNPs (0.1±0.001 wt%)	S+Sn	31% increase in Young's modulus, 40% increase in tensile strength, 53% increase in fracture toughness	[125]
RGO (0.2 wt%)	S+Sn+PM	Tg increase 11°C, K _{IC} improved by 52%	[126]
GNPs (2 wt%)	3R	82% increase in fracture toughness	[122]
PBA-GFs (10 wt%)	S+Sn	1.53 W/mK in thermal conductivity	[127]
GNPs (6 wt%)	HSM	23.5% increase in Young's modulus	[128]
Graphene (0.46 vol%)	FD+M /S+Sn	38% increase in strength, 37% increase in modulus, electrical percolation threshold 0.088 vol%	[129]
Silane-GNPs (0.5 wt%)	3R	82% increase in toughness, 38% increase in strength	[130]
DGEBA-GO (0.25wt%)	S+Sn+PM	13% increase in modulus, 75% increase in strength, 41% increase in K _{IC}	[131]

Py-PGMA–GNPs (4phr)	S+Sn	1.91 W/mK in thermal conductivity, 800% increase comparing to neat epoxy	[132]
Silane-GO (1 wt%)	S+Sn	45% increase in tensile strength, 133% increase in elongation	[133]
GNPs (1 wt%)	3R	43% increase in K_{IC}	[134]
TLCP-g-GO (1 wt%)	S+Sn	46% increase in tensile strength, 48% increase in flexural modulus	[135]
Graphene (0.49vol%)	S+Sn	27% increase in Young's modulus, 124% increase in K_{IC}	[136]
Multi-layer graphene (10 vol%)	S+Sn	2300% increase in thermal conductivity	[137]
3DGS (0.2 wt%)	Mold	121% increase in tensile strength, 148% increase in compressing strength	[138]

S: solvent dispersion; Sn: sonication; PM: planetary ball mill; 3R: 3-roll mill; GFs: graphene flakes; HSM: high-shear mixer; FD: freeze dry; M: mechanical mixing; DGEBA: diglycidyl ether of bisphenol-A; Py-PGMA: poly(glycidyl methacrylate) containing localized pyrene groups; TLCP: thermotropic liquid crystalline epoxy; 3DGS: three-dimensional graphene skeleton.

1.2.2 CF-reinforced composites

CF/polymer composites have been used for commercial production since the 1960s. Due to their high specific strength and stiffness, performance to weight ratio, high thermal stability, and self-lubrication, CF/polymer composites have a wide range of potential applications, especially in aviation, automotive industries and mechanical engineering, etc.

1.2.2.1 Manufacture process

The manufacturing process for CF/polymer composites has a large influence on the final application. There are several common methods to prepare fiber/polymer composites, including hand lay-up technique, resin transfer molding (RTM), pultrusion, etc.

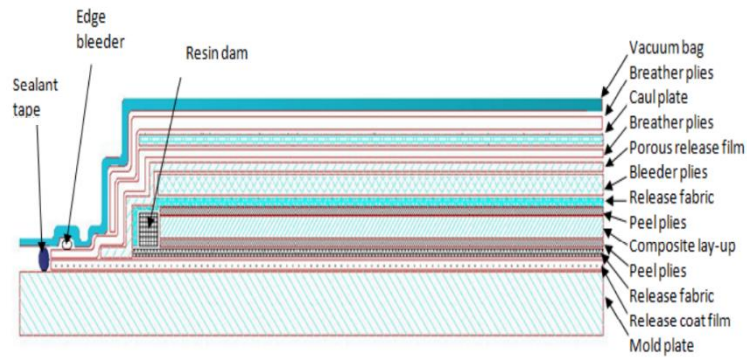


Figure 1.16 Schematic of a typical bag lay-up molding process [139].

Bag molding is an efficient and versatile process used in manufacturing CF/epoxy composites. A cross section of a typical lay-up molding of a composite structure is shown in **Figure 1.16**. The laminates are laid up in a mold, covered with a flexible bag, and cured with heat in vacuum. This method could extensively reduce the pores existing in the final composites [139].

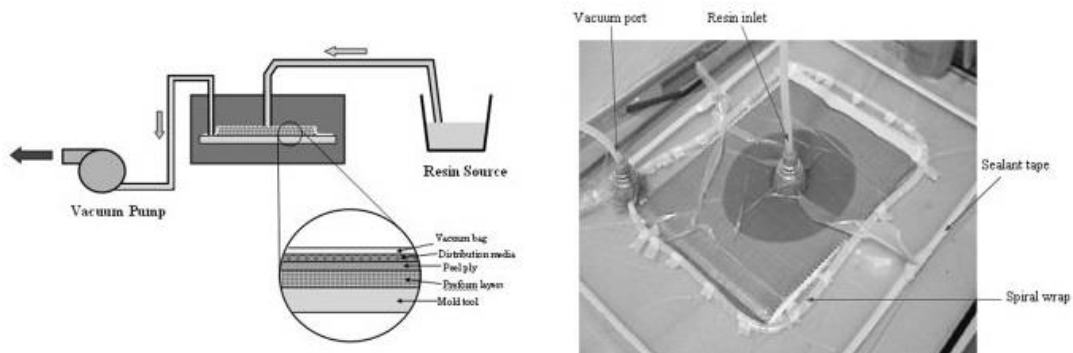


Figure 1.17 Vacuum assisted resin transfer molding (RTM) process and fabrication setup [140].

RTM is a wet impregnation process to produce composites. The resin is injected into a mold cavity under pressure. This method is used to produce continuous CF composites with intricate shapes. Typically, the resin of relatively low viscosity is used in the RTM process. The RTM allows a better control over the orientation of the fibers. Vacuum-assisted resin transfer molding (VARTM) is a variation of the RTM process, in which the vacuum is applied

to the outlet of the mold and draw the resin into the mold [139, 140]. The schematic is shown in **Figure 1.17**.

Pultrusion is a continuous composite fabrication process. The CFs are impregnated with the polymer matrix and are pulled through a heated die to form composite profiles (as shown in **Figure 1.18**).

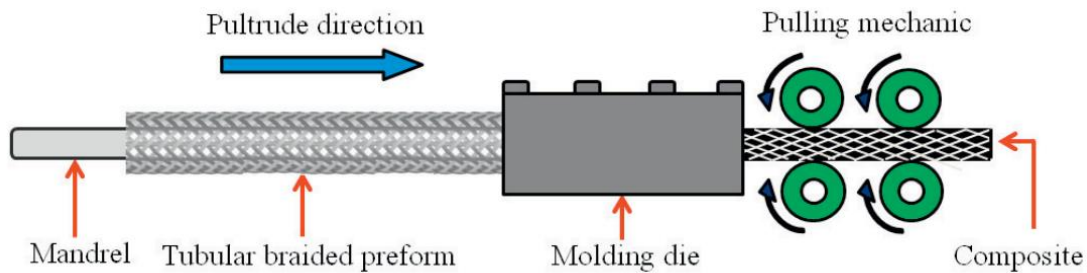


Figure 1.18 Schematic of the pultrusion method [142].

1.2.2.2 Applications

Unlike graphene-based composites which is too recent, the development of CF composites has already been used in a wide range of field, such as aircraft/aerospace, sports and recreation industries.

Aircraft is the dominant market for CFs due to its high specific properties, such as light weight, thermal stability and high rigidity, etc. CFs are used as a critical part in the modern aircraft/aerospace applications. Boeing and Airbus civil aircraft, the international space station (ISS) and satellites use CFs to make the primary and secondary structure [147]. The Boeing 787 makes greater use of composite materials in its airframe and primary structure than any previous Boeing commercial airplane. Undertaking the design process without preconceived ideas enabled Boeing engineers to specify the optimum material for specific applications throughout the airframe. The result is an airframe comprising nearly half carbon fiber reinforced plastic and other composites. This approach offers weight savings on average of 20 percent compared to more conventional aluminum designs.

CFs have also been used extensively in the sporting goods. Typical products include golf club shafts, tennis racquets fishing rods, bicycle components and skiing equipment, benefiting from the low weight and high strength of CF composites.

New applications of CFs are developed at a rapid pace. The improvement in electrical conductivity makes them suitable for elimination of static electricity, for electrodes, batteries or fuel cells [148, 149]. The high thermal conductivity and low thermal expansion make them attractive for heat dissipation components [150, 151].

1.3 Interfacial study between the polymer matrix and reinforcements

The interface is a region, which physically and chemically connects two different phases, e.g. the polymer matrix and the reinforcing fillers in the composites. It plays a crucial role in the final performance of the polymer composites, such as mechanical, thermal and electrical properties. An interface region has a thickness ranging from several nanometers to several hundreds of micrometers. For large thicknesses, a new concept comes out as “interphase”. In carbon-based nanofillers, such as graphene, CNTs and CFs, it is often difficult to characterize an interface in polymer nanocomposites due to the similar element component. In this part, we focus on the discussion of the interface effect on the mechanical properties in polymer composites reinforced by carbon-based nanofillers.

In polymer composites, nanofillers have much higher modulus and strength compared to the polymer matrix. The stress transfer efficiency determines the final performance of composites. In other words, a better interface gives rise to better reinforcement, in which the majority of the load is transferred to the nanofillers. The shear-lag theory is now the foundation stone of composite micromechanics [152], which was first used to analyze the short-fiber system by Cox [153].

1.3.1 Methods for GNPs reinforced nano-composites

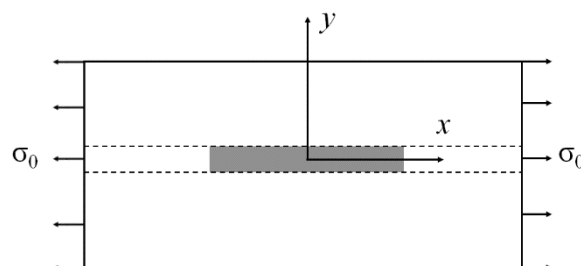


Figure 1.19 Schematic showing the two-dimensional stress transfer model [154].

The existing stress transfer model for the two-dimensional reinforcements assumes that the plane of the platelet is bonded to the polymer matrix, and is parallel to the loading direction.

The edges of the platelet are debonded to the polymer matrix so that the stress transfer only occurs on the plane of the platelet (as shown in **Figure 1.19**) [154]. For the reinforcement of a composite by platelets, such as GNPs, the starting point is to consider it to be a two-dimensional version of a CF reinforcement. The shear lag approach is also used by a number of groups to analyze reinforcement by platelets in the context of clays and biological systems such as bone and shells that have microstructures that rely upon a platelet reinforcement [155].

Raman spectroscopy has been largely used to follow the stress transfer between the matrix and nanofillers in a lot of polymer composites. In general, the shift in the Raman band rate is proportional to the stress or strain in the nanofillers due to changes in bond length. As the bond is stretched, the Raman wavenumber generally experiences a red-shift which is reversed when the system is unloaded. Gong *et al.* [156] and Young *et al.* [157] developed Raman band shift method to characterize the IFSS of monolayer graphene composites and they found the value of -2 MPa. Li *et al* used Raman spectroscopy to monitor interfacial stress transfer in poly(vinyl alcohol) (PVA) nanocomposites reinforced by GO. The results indicates that it is possible to follow the stress transfer between the PVA and GO from stress-induced shifts of the Raman D band (as shown in **Figure 1.20**) [157].

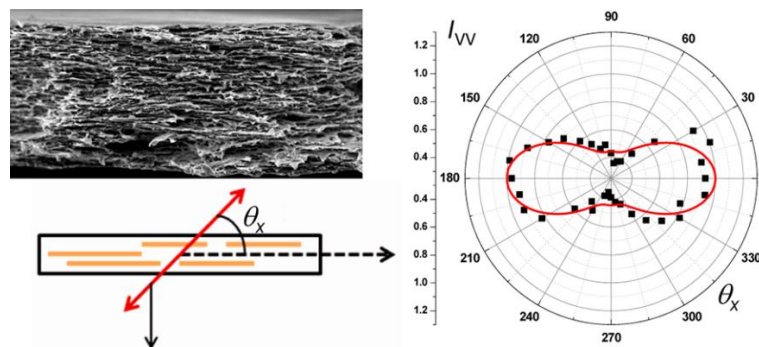


Figure 1.20 Interfacial stress transfer in GO nanocomposites demonstrated by Raman spectroscopy [157].

Raman spectroscopy only provides indirect stress/strain responses of the graphene as a function of the beam surface strain, rather than through a direct measurement of the stress-strain responses of the graphene and the polymer matrix. Jang *et al.* [158] used a semi-empirical approach to determine the IFSS of graphene composites by combining experiments with finite

element (FE) modeling. The IFSS of the reduced graphene oxide (RGO)/polycarbonate composites was successfully estimated around 136 MPa.

In our previous study, we designed a sandwich structure by using two types of polymers, polymethyl methacrylate (PMMA) and polyvinyl alcohol (PVA), with a layer of GNPs sandwiched between them to directly measure the IFSS. Then, an in-plane load was applied to shear the structure. By changing the GNP density covering the interface, we could obtain a series of mean IFSS. After linear fitting, we obtained the average IFSS between PMMA and GNPs which was 0.35 MPa when the GNP covered areas reached 100% (**Figure 1.21**, more details could be found in *Appendix I*) [159].

Li *et al.* [160] have created a novel nano-sandwich structure made of thin poly(ethyl methacrylate) (PEMA) layer/single layer CVD graphene/thin PEMA layer, and have applied a nano-bubble inflation method to obtain the interfacial mechanical response. Significant mechanical (stiffness) reinforcement has been observed at small strains in the rubbery state of the PEMA and the results were used to estimate the stiffness of the large area, single sheet, CVD graphene (**Figure 1.22**). Cai *et al.* [161] developed a novel method to directly characterize and measure the relative strength of the interfacial attractive forces between GO and polymer matrix on the nanoscale of an individual particle using AFM techniques.

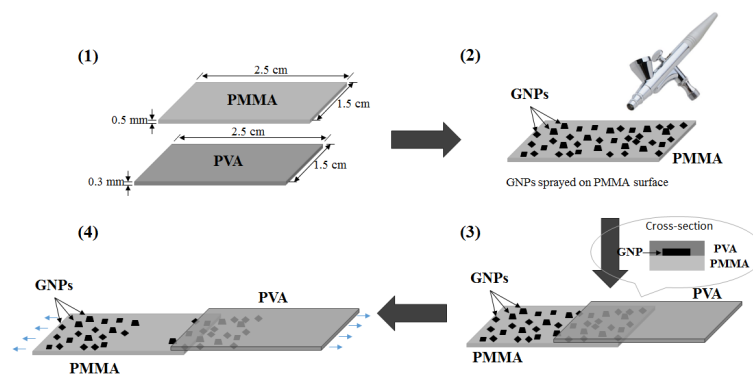


Figure 1.21 Illustration of the stretching method to measure the IFSS between GNPs and PMMA[159].

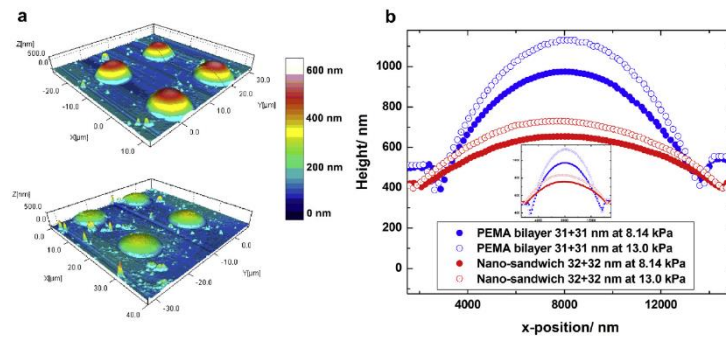


Figure 1.22 Mechanical responses of a polymer GNP-sheet nano-sandwich [160].

Due to the small scale of the interface, scanning electron microscopy (SEM) is usually used to directly observe the interface. Ramanathan *et al.* [162] incorporated 0.05 wt% of functionalized graphene sheets in a PMMA matrix and achieved an improvement of nearly 30°C of the glass transition temperature T_g . SEM images revealed the nanoparticle–polymer interactions (**Figure 1.23**).

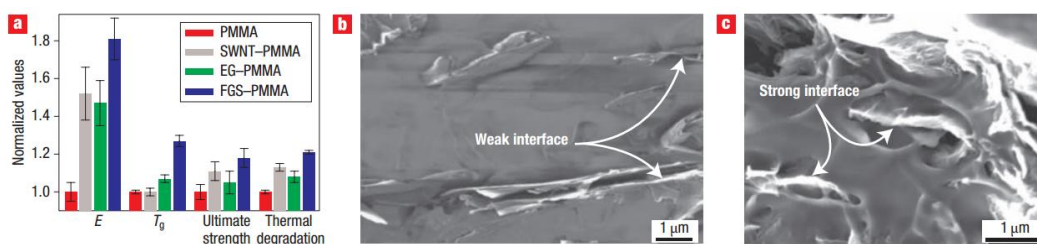


Figure 1.23 (a) Property improvements for 1 wt% nanoparticle–PMMA composites and (b,c) SEM images revealing the two typical types of nanoparticle–polymer interactions [162].

1.3.2 Methods for CF reinforced composites

The combination of an epoxy matrix and fibers gives rise to composites combining the advantages of each component. Since the polymers are soft, flexible and lightweight compared to fibers, their combination offers a high strength-to-weight ratio to the final composite. The performance of composites largely depends on those of each component and on their interfacial interaction. Due to the different chemical composition of the CFs and the matrix, a strong adhesion at the interface is needed for an efficient stress transfer and bond distribution. Hence, a clear understanding of the complex nature of the interface is needed to optimize the surface

modification procedures and thus to increase the usefulness of CFs as a constituent of composites.

Interfacial strengths can be estimated qualitatively or semi-quantitatively by observing the tensile fracture of single fibers in an epoxy matrix, as well as the local stress and CF debonding. At present, there are primarily four techniques that have been developed over the years, namely CF pull-out, micro bond, CF push-in and fragmentation tests.

Single fiber pull-out tests are the most commonly used methods to directly estimate the IFSS between the fiber and the matrix. Single fibers are cast into a thin film of epoxy resin, the fiber passing through the film normal to the surface of the resin. The force and displacement are monitored as the fiber is pulled axially until either pull-out occurs or the fiber breaks, as shown in **Figure 1.24** [163]. Kelly [163] gave the earliest description of the single fiber pull out test. It was found that if the embedded length of the fiber was longer than the length of interfacial failure, complete debonding could not occur. Favre *et al.* [164] developed it by studying CFs in epoxy. The IFSS obtained by this method ranged from 25 to 90 MPa.

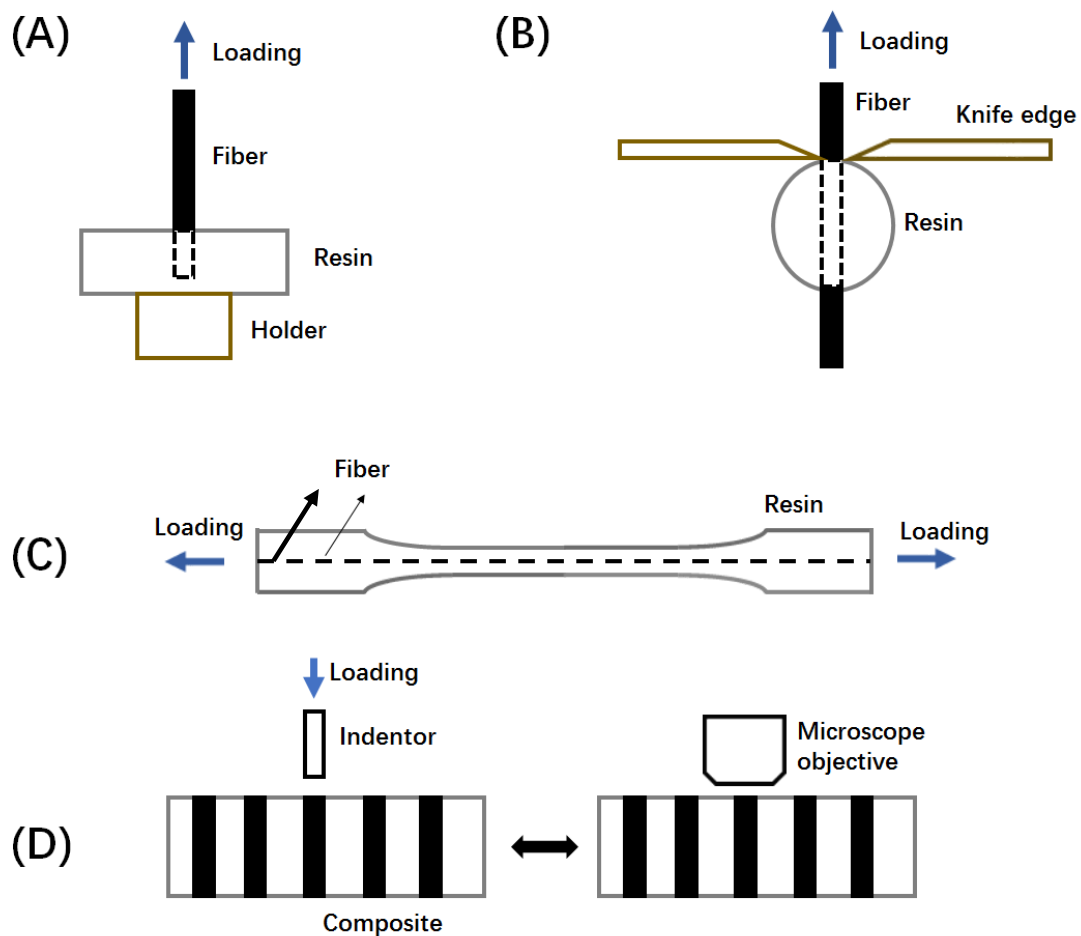


Figure 1.24 Four major fiber micromechanical test methods: (A) single fiber pull out test; (B) microdroplet method; (C) Fragmentation test; (D) Micro-indentation test [165].

The microbond test, also named as microdroplet methods, which is very similar to the single fiber pull out test and was first developed by Miller *et al.* [166], is useful due to its simplicity and overall repeatability of experimental results. A droplet of resin is attached on the fiber and cured in position. Usually, numerous droplets could be attached on one single fiber. Then, the sample is placed in a tensile test machine. the fiber end is gripped on the tensile head and the resin droplet is placed between two knife edges. The fiber is pulled against the knife edges and the load/extension is recorded together with the embedded length and fiber diameter for the IFSS calculation, as shown in **Figure 1.24B**. Rahmani *et al.* [167] studied the IFSS of a specific CF/epoxy composite (T650/Cycom 5320-1) by microdroplet to determine how changes in the post cure temperature affects the fiber/matrix adhesion. Sockalingam et al. used a FE modeling methodology to compute and assess the importance of various factors affecting the failure mechanisms in the microdroplet test used to measure the IFSS of S-glass fiber/epoxy matrix. The developed holistic modeling methodology allows an accurate determination of the traction-separation behavior of the interface [168].

The IFSS obtained by the two previous methods are a good indication of the interfacial strength, but these methods also have the disadvantage that the local environment in a single fiber composite is very different from the actual environment within the composite. Therefore, a micro indentation method has been developed, which is directly performed on “macroscopic” composite samples. In the indentation test, a section of the composite with the fiber vertical to the fracture surface is carefully polished and placed in the test machine. The selected fiber should be isolated. The load is applied by an indenter which has a diameter similar to the one of the tested fiber. The load and displacement response is recorded and the shear-lag analysis is used to determine the IFSS, as shown in **Figure 1.24D** [169, 170].

The fragmentation test method is the oldest method over the four techniques. A single fiber is carefully embedded in the center of a dog-bone shape resin sample. Then, the prepared sample is placed in a tensile test machine and loaded in tension. As the load increases, the fiber embedded in the resin will break into shorter length until a saturation level is achieved. The

fragment length is then measured, as shown in **Figure 1.24C**. Usually, the better the interface, the smaller the length of the fragment [171, 172].

1.4 Transmission electron microscopy (TEM) in nanocomposite study

Transmission electron microscopy (TEM), combined with other analysis techniques, such as energy-loss spectroscopy (EELS) and energy-dispersive X-ray spectroscopy (EDX), has played an important role in the study of the morphology and structure-property correlations of polymers including homopolymers, copolymers, blends and composites. There are two major advantages by using TEM in nanocomposites science and technology. First, TEM analyses usually focus on a very small region, on nanometer scale or even smaller scale, which contains a much more detailed information than that from other sources. TEM provides information on the morphology of the polymer as well as the filler. To study their interaction, their interface can be observed at a high resolution. Secondly, TEM allows to study the response of all the structural details of the composites when a load is applied (*in-situ*) enabling the design of tailored materials. TEM is the only technique which provides a very direct evidence of the intercalation and dispersion of the particles in the polymer, which allows a direct quantification of the morphological features of the composites [173].

1.4.1 Experimental techniques

The quality of the results acquired by microscopy depends much on the sample preparation. Without proper care during the specimen preparation stage, no reliable result can be obtained. For carbon-based fillers, such as CFs and GNPs, the challenge arises because of the huge mismatch in properties, such as modulus and hardness between fillers and matrix. This brings great difficulty for preparing a thin TEM sample with an original interphase [174]. The thickness of the films required for TEM investigation are in the range of 100-150 nm. Focused ion beam (FIB) and ultramicrotomy (UM) are two typical methods to prepare the TEM samples, the samples prepared by two methods are shown in **Figure 1.25**. FIB uses a finely focused ion beam to bombard the target region. By adjusting the current, site-specific milling and cutting can be performed [175]. UM produces an ultrathin film with a thickness achieving 30 nm by creating a crack that propagates into a sample [176].

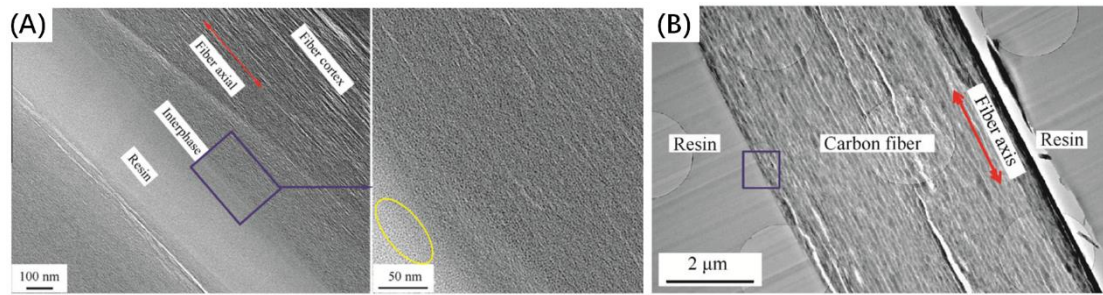


Figure 1.25 TEM images of CF/epoxy composites prepared by two typical methods: (A) FIB; (B) ultramicrotome [174].

FIB is a convenient and suitable TEM sample preparation method for interphase study. The thin uniform laminate we obtain with the use of a small incidence angle of the ion beam is suitable for TEM and EELS analysis. However, it introduces some Ga^+ ions which limit the high-resolution analysis of fine structure. Moreover, the lamella prepared by FIB is relatively smaller in the transverse directions than that prepared by UM. Hence, it is not suitable for the examination of the dispersion state of nanofillers. Regarding the UM method, distortion and crack occur in fine structures, especially in the region of interest at the interface due to the large discrepancy of modulus. However, samples prepared by UM covers a much larger area than samples prepared by FIB. It is very suitable for the confirmation of the dispersion state. The comparison of two different methods are summarized in **Table 1.3**.

Table 1.3 Comparison of two typical methods for preparation of TEM samples [174].

Comparison aspects	Focused ion beam (FIB)	Ultramicrotome (UM)
Capability for TEM analysis of interface	Suitable	Not suitable
Interphase integrity	Intact	Deformed or broken
Dispersion state of nanofillers	Not suitable	Suitable
Drawback	Ga^+ ion implantation	Expensive diamond knife is easy to damage
Preparation time & efficiency	Fast (less than 4h)	Simplification & Time efficiency
Cost	Expensive	low

1.4.2 Identification of interface/interphase by TEM

A detailed information on the graphene layers exfoliation, dispersion degree and the relative alignment of graphene and CNTs in polymeric matrix can be obtained by TEM. Nevertheless, the identification of the interface and interphase between fillers and the polymer matrix is not trivial, since all components are mainly formed of carbon atoms and consequently the contrast produced among them is very similar. Thus, the identification of the interface and interphase by TEM is not straightforward and requires microscopes equipped with different configurations of the magnetic lenses and of the electron beam. In addition, the information acquired by TEM comes from a very small region of the samples and frequently it is necessary to analyze several regions to get more representative results. Because of these technical limitations, the interface and interphase in the composites have not been conclusively identified by TEM.

1.4.2.1 Electron energy loss spectroscopy (EELS)

When electrons interact with a solid, they are scattered due to the electrostatic field generated by the sample. Images are essentially the result of elastic scattering where no energy is transferred from the electron wave to the sample. but in some cases, the electron wave transfers a specific amount of energy to the specimen (inelastic interaction). These two types of interactions are shown in **Figure 1.26**.

There are two situations in the elastic scattering, large angle scattering, where the deflection angle exceeds 90° , and small angle scattering. The former involves a small amount of electrons which travel close enough to the atomic nuclei, with a high concentration of positive charge in a very small area (typically 10^{-15} m). These electrons are called backscattered electron and are reflected from the same surface that it entered. Of course, the occurrence of this phenomenon decreases with the energy of the incoming electron (In scanning electron microscopy system). The latter involves most electrons travelling further from the center of an atom and therefore being scattered through smaller angles.

Inelastic scattering is the result of the interaction between the incident probing electron and the electrons in the sample. It is also divided into two types: inner-shell and outer-shell interaction. For the inner-shell interaction, the fast electron loses an amount of energy similar to or greater than the original binding energy of the inner-shell electron. As a result, the incident electron is scattered through an angle of the order of 10 mrad for an incident energy of 100 eV.

The outer-shell interaction can also happen as single-electron excitation. The incident electron is scattered through an angle of 1 or 2 mrad for a 100 keV incident energy [177].

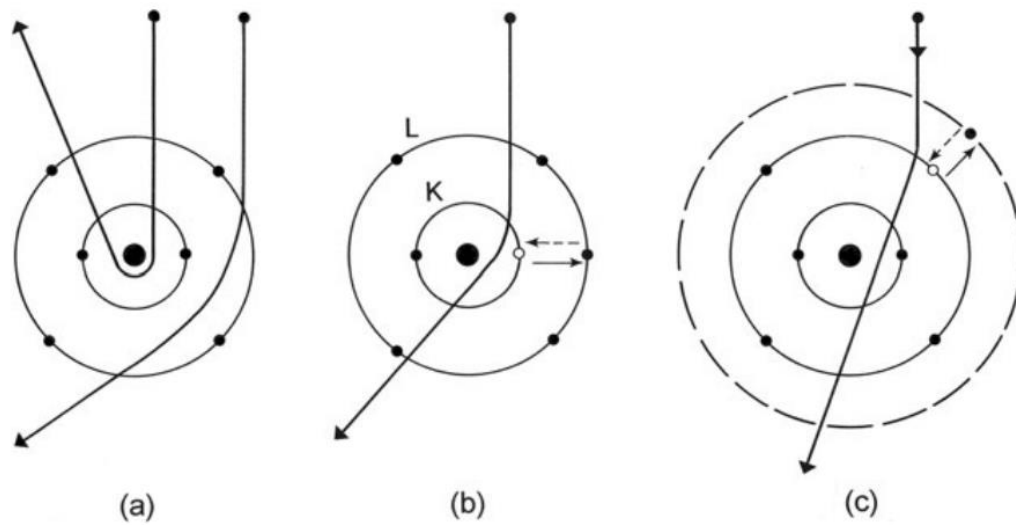


Figure 1.26 A classical view of electron scattering by a single atom (carbon). (a) Elastic scattering is caused by Coulomb attraction with the nucleus. Inelastic scattering results from Coulomb repulsion by (b) inner-, or (c) outer-shell electrons, which are excited to a higher energy state. The reverse transitions (de-excitation) are shown by broken arrows [177].

Electron energy loss spectroscopy (EELS) is an important characterization technique available in TEM. It involves a measurement of the energy distribution of probing electrons that have interacted with a specimen and lost energy due to inelastic scattering. If the incident electrons have a kinetic energy of a few hundred electron volts (eV) and are reflected from the surface of the specimen, the technique is called high-resolution EELS. Relatively simple instrumentation can then provide spectra with an energy resolution down to a few meV, sufficient to resolve vibrational as well as electronic modes of energy loss; this technique is used to extensively study the physics and chemistry of solid films.

High energy electrons can pass through a thin film with a thickness below about 1 μm . The electromagnetic lenses of the TEM can be used to focus them into a probe with very small diameter (1 nm or even 0.1 nm). As a result, EELS carried out in a TEM is capable of very high spatial resolution. Combined with the low specimen thickness, this implies spectroscopic analysis of extremely small volumes of material.

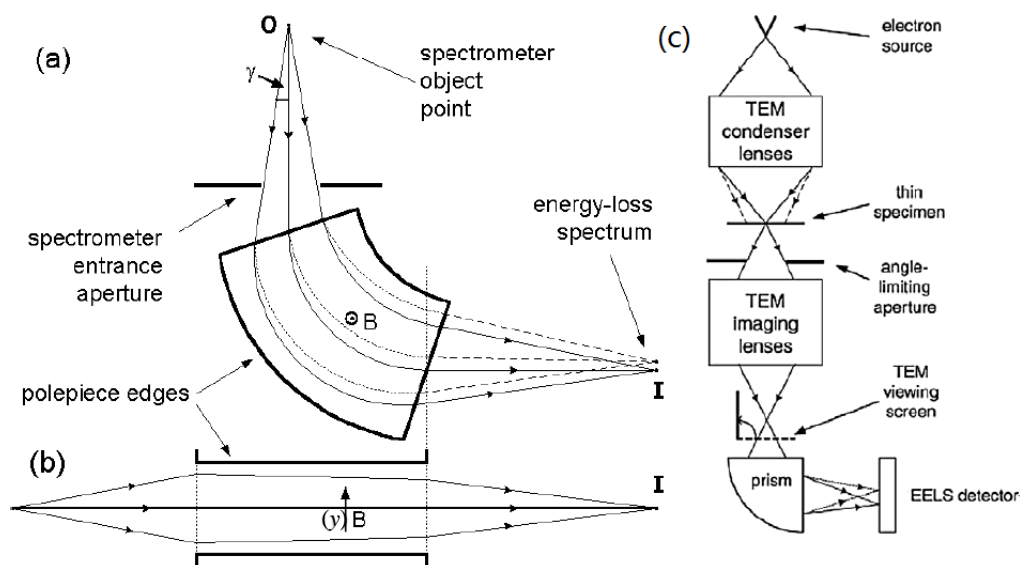


Figure 1.27 Dispersive and focusing properties of a magnetic prism (a) in a plane perpendicular to the magnetic field (side view) and (b) parallel to the field (top view). Solid lines represent zero-loss electrons; dashed lines represent those that have lost energy through interaction with the sample. (c) Conventional TEM with a magnetic prism spectrometer below the viewing screen [178].

TEM-EELS instrumentation is based on the magnetic prism, in which a uniform magnetic field B (of the order of 0.01 T) is generated by an electromagnet with carefully shaped polar pieces, as shown in **Figure 1.27**. Within this field, electrons follow circular paths of radius R and are deflected through an angle of typically 90° . The sideways force on an electron is

$$F = B e v = m v^2/R$$

where, e , v and m are the electron velocity, charge and relativistic mass, giving a bent radius that depends on speed and therefore on electron energy:

$$R = (m/e) B v$$

while this behavior resembles the bending and dispersion of a beam of white light by a glass prism, the electron prism also has a focusing action. Electrons that stray from the central trajectory in a direction perpendicular to the field (**Figure 1.27a**) experience an increase or

decrease in their path length within the field, giving rise to a greater or lesser deflection angle. If the entrance beam originates from a point object, electrons of a given energy are returned to a single image point. The existence of different electron energies then results in a focused spectrum in a plane passing through that point. In addition, the fringing field at the polar piece edges focuses electrons that deviate in a direction y parallel to the magnetic field (**Figure 1.27b**). By adjusting the angles of the polar piece edges, the focusing power in these two perpendicular directions can be made equal, giving a spectrum of small width in the direction of the applied magnetic field.

The simplest form of energy-loss system consists in a conventional TEM fitted with a magnetic prism below its image-viewing chamber (**Figure 1.27c**). By tilting the TEM screen to a vertical position, electrons can enter the spectrometer, where they are dispersed according to their kinetic energy, which is their incident energy E_0 minus its energy loss ΔE occurring in the sample. A spectrometer entrance aperture, typically variable from 1 to 5 mm in diameter, limits the range of entrance angles and ensures adequate energy resolution.

Figure 1.28 shows a typical energy-loss spectrum, recorded up to a few tens of electron volts, sometimes called the low-loss region. The first peak, the most intense for a very thin specimen, occurs at 0 eV and is therefore called the zero-loss peak. It represents electrons that did not undergo inelastic scattering, but which might have been scattered elastically with an energy loss too small to measure. The width of the zero-loss peak, typically 0.2-2 eV, reflects mainly the energy distribution of the electron source.

Other low-loss features arise from inelastic scattering by conduction or valence electrons. The most prominent peak, centered around 23 eV, results from a plasma resonance of the valence electrons. The increase in intensity around 54 eV represents inelastic scattering from inner-shell electrons. The other edges occur at a higher energy loss, which corresponds to the inner shell electrons, for carbon materials, is the π bond and σ bond.

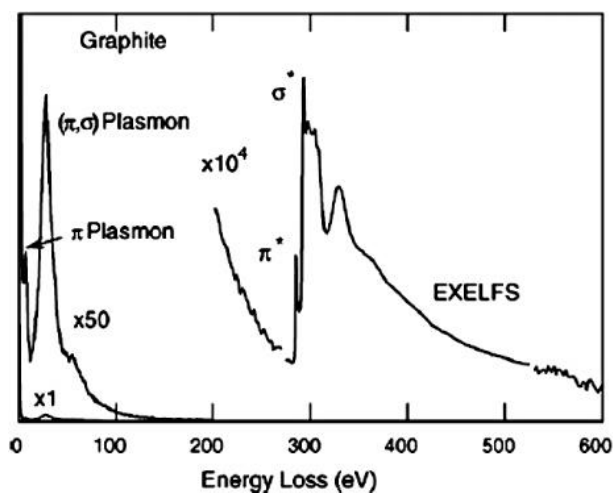


Fig.1.28 Electron energy loss spectroscopy (EELS) of carbon material: the carbon K-edge, corresponding to the excitation of an electron of the K-shell is measured at 284eV and beyond. Due to the high energy resolution of this type of spectrometry, the features beyond this threshold can also be analyzed and give information on the bonding state of the excited atom.

1.4.2.2 Energy dispersion X-ray analysis (EDX)

Energy dispersive X-ray spectroscopy (EDX) is the most standard and reliable one in the field of analytical electron microscopy and is widely used.

EDX makes use of the X-ray spectrum emitted by a solid sample as a deexcitation process. This deexcitation occurs after the excitation process due to incident electrons and mentioned above to describe EELS. This method is used to obtain a local chemical analysis. All elements from atomic number 4 to 92 can be detected in principle. Qualitative analysis involves the identification of the lines in the spectrum and is straightforward owing to the simplicity of X-ray spectra. Quantitative analysis entails measuring line intensities for each element in the sample and for the same elements in calibration standards of known composition.

By scanning the beam in a television-like raster and displaying the intensity of a selected X-ray line, element distribution images or maps can be produced.

The spatial resolution of EDX is governed by the penetration and spreading of the electron beam in the specimen. Since the electrons penetrate an approximately constant mass, spatial resolution is a function of density. In a TEM system, due to the ultra-thin specimens (around 100 nm thick), a better spatial resolution can be reached.

1.5 Motivation and overview

The interface&interphase plays a crucial role in determining the entire performance of composites. The understanding of this topic is important to help researchers to develop composites with high performance. The present dissertation addresses them and provides some answers to this topic.

In chapter 2, I introduce the surface modification methods for the reinforcements. Two series of reinforcements have been studied in this thesis, CF-based materials and graphene-based materials, respectively. Two methods, oxidation and grafting CNTs, have been employed to treat the reinforcements' surface. Basic characterizations have been conducted and the results have been analyzed in detail. From this chapter, the references are less extensive. Only the most representative works are mentioned.

In chapter 3, I study the interfacial properties of CF/epoxy composites in multi-scale. First, the intrinsic properties of four kinds of CF, original CF, desized CF, CF-CNTs and oxidized CF-CNTs, are studied. Secondly, the interfacial shear strength (IFSS) of different composites are measured by single fragmentation method. Thirdly, an *in-situ* tensile test method in SEM is developed to measure the interfacial strength between CF and epoxy matrix. Then, this method is applied on the GNPs/epoxy composites. Lastly, the STEM combined EDX mapping is conducted to study the interface in a nano-scale.

In chapter 4, four composites, GNPs/epoxy, O-GNPs/epoxy, GO/epoxy and GNP-CNTs/epoxy, are studied by combining STEM and EELS. STEM allows the distribution and morphology of the nanofillers to be investigated at high spatial resolution. The thickness influence on the core-loss spectra is discussed. Core-loss spectra are intensively studied in nanofillers parts and matrix. Components, chemical bonding in different regions are reflected by the excitation energies in EELS spectra. EDX mapping is also conducted in this work, which could be used to indirectly evaluate the interface strength.

In chapter 5, a quantitatively characterize of the interface&interphase between graphene and epoxy matrix are conducted by combining TEM and EELS. Two nanofillers are studied here, GNPs and GO, respectively. By doing line-acquisition of plasmon spectra in the interface, the density variation in the interface is clearly observed.

In chapter 6, general conclusions are formed according to works and perspectives are provided for the improvement of the future work.

References

1. Xu, Z. and C. Gao, *Graphene fiber: a new trend in carbon fibers*. *Materials Today*, 2015. **18**(9): p. 480-492.
2. Donnet, J.-B. and R.C. Bansal, *Carbon fibers*. 1998: CRC Press.
3. Standage, A. and R. Prescott, *High elastic modulus carbon fibre*. *Nature*, 1966. **211**: p. 169.
4. Johnson, W. and W. Watt, *Structure of High Modulus Carbon Fibres*. *Nature*, 1967. **215**(5099): p. 384-386.
5. Jeffries, R., *Prospects for Carbon Fibres*. *Nature*, 1971. **232**(5309): p. 304-307.
6. Frank, E., et al., *Carbon Fibers: Precursor Systems, Processing, Structure, and Properties*. *Angewandte Chemie International Edition*, 2014. **53**(21): p. 5262-5298.
7. Dai, Z., et al., *Effect of heat treatment on carbon fiber surface properties and fibers/epoxy interfacial adhesion*. *Applied surface science*, 2011. **257**(20): p. 8457-8461.
8. Dresselhaus, M.S., et al., *Synthesis of graphite fibers and filaments*, in *Graphite fibers and filaments*. 1988, Springer. p. 12-34.
9. Dorey, G., *Carbon fibres and their applications*. *Journal of Physics D: Applied Physics*, 1987. **20**(3): p. 245.
10. Hoffman, W.P., et al., *The surface topography of non-shear treated pitch and PAN carbon fibers as viewed by the STM*. *Journal of Materials Research*, 2011. **6**(8): p. 1685-1694.
11. Johnson, D., *Structure-property relationships in carbon fibres*. *Journal of Physics D: Applied Physics*, 1987. **20**(3): p. 286.
12. Edie, D.D., *The effect of processing on the structure and properties of carbon fibers*. *Carbon*, 1998. **36**(4): p. 345-362.
13. *Recent Progress in Fabrication, Structure, and Properties of Carbon Fibers*. *Polymer Reviews*, 2012. **52**(3): p. 234-258.
14. Dvir, H., J. Jopp, and M. Gottlieb, *Estimation of polymer–surface interfacial interaction strength by a contact AFM technique*. *Journal of colloid and interface science*, 2006. **304**(1): p. 58-66.
15. Park, S.-J. and B.-J. Kim, *Roles of acidic functional groups of carbon fiber surfaces in enhancing interfacial adhesion behavior*. *Materials Science and Engineering: A*, 2005. **408**(1): p. 269-273.
16. Kim, J.-K. and Y.-w. Mai, *High strength, high fracture toughness fibre composites with interface control—A review*. *Composites Science and Technology*, 1991. **41**(4): p. 333-378.
17. Pukánszky, B., *Interfaces and interphases in multicomponent materials: past, present, future*. *European Polymer Journal*, 2005. **41**(4): p. 645-662.
18. Jones, C., *The chemistry of carbon fibre surfaces and its effect on interfacial phenomena in fibre/epoxy composites*. *Composites Science and Technology*, 1991. **42**(1): p. 275-298.

19. Bijwe, J. and M. Sharma, *Carbon Fabric-Reinforced Polymer Composites and Parameters Controlling Tribological Performance*, in *Wear of Advanced Materials*. 2013, John Wiley & Sons, Inc. p. 1-60.
20. Herrick, J.W., P.E. Gruber Jr, and F.T. Mansur, *SURFACE TREATMENTS FOR FIBROUS CARBON REINFORCEMENTS*. 1966, DTIC Document.
21. Scola, D. and M. Basche, *Treatment of carbon fibers*. 1973, Google Patents.
22. Morra, M., et al., *Surface studies on untreated and plasma-treated carbon fibers*. *Composites science and technology*, 1991. **42**(4): p. 361-372.
23. Commercon, P. and J. Wightman, *Surface characterization of plasma treated carbon fibers and adhesion to a thermoplastic polymer*. *The Journal of Adhesion*, 1992. **38**(1-2): p. 55-78.
24. Yuan, L., et al., *Plasma surface treatment on carbon fibers. Part 1: Morphology and surface analysis of plasma etched fibers*. *Composites science and technology*, 1992. **45**(1): p. 1-7.
25. Yuan, L., S. Shyu, and J. Lai, *Plasma surface treatments of carbon fibers. Part 2: Interfacial adhesion with poly (phenylene sulfide)*. *Composites science and technology*, 1992. **45**(1): p. 9-16.
26. Allred, R.E. and W.C. Schimpf, *CO₂ plasma modification of high-modulus carbon fibers and their adhesion to epoxy resins*. *Journal of adhesion science and technology*, 1994. **8**(4): p. 383-394.
27. Dilsiz, N., et al., *Effect of Plasma Polymerization on Carbon Fibers Used for Fiber/Epoxy Composites*. *Journal of Colloid and Interface Science*, 1995. **170**(1): p. 241-248.
28. Vaidyanathan, N.P., et al., *Surface treatment of carbon fibers using low temperature plasma*. *The Journal of Adhesion*, 1995. **48**(1-4): p. 1-24.
29. Chand, N., E. Schulz, and G. Hinrichsen, *Adhesion improvement of carbon fibres by plasma treatment and evaluation by pull-out*. *Journal of materials science letters*, 1996. **15**(15): p. 1374-1375.
30. Bogoeva-Gaceva, G., et al., *Characterization of the surface and interphase of plasma-treated HM carbon fibres*. *Composites Part A: Applied Science and Manufacturing*, 1997. **28**(5): p. 445-452.
31. Pittman, C., et al., *Oxygen plasma and isobutylene plasma treatments of carbon fibers: determination of surface functionality and effects on composite properties*. *Carbon*, 1998. **36**(1): p. 25-37.
32. Erden, S., et al., *Continuous Atmospheric Plasma Oxidation of Carbon Fibres: Influence on the Fibre Surface and Bulk Properties and Adhesion to Polyamide 12*. *Plasma Chemistry and Plasma Processing*, 2010. **30**(4): p. 471-487.
33. Kim, J.-K. and Y.-W. Mai, *Engineered interfaces in fiber reinforced composites*. 1998: Elsevier.
34. Yumitori, S. and Y. Nakanishi, *Effect of anodic oxidation of coal tar pitch-based carbon fibre on adhesion in epoxy matrix: Part 2. Comparative study of three alkaline solutions*. *Composites Part A: Applied Science and Manufacturing*, 1996. **27**(11): p. 1059-1066.
35. Fukunaga, A. and S. Ueda, *Anodic surface oxidation for pitch-based carbon fibers and the interfacial bond strengths in epoxy matrices*. *Composites Science and Technology*, 2000. **60**(2): p. 249-254.
36. Liu, X., C. Yang, and Y. Lu, *Contrastive study of anodic oxidation on carbon fibers and graphite fibers*. *Applied Surface Science*, 2012. **258**(10): p. 4268-4275.
37. Morgan, P., *Carbon fibers and their composites*. 2005: CRC press.

38. Goan, J. and S. Prosen, *Interfacial bonding in graphite fiber-resin composites*, in *Interfaces in Composites*. 1969, ASTM International.
39. Donnet, J.B. and G. Guilpain, *Surface characterization of carbon fibres*. *Composites*, 1991. **22**(1): p. 59-62.
40. Dagli, G. and N.-H. Sung, *Properties of carbon/graphite fibers modified by plasma polymerization*. *Polymer Composites*, 1989. **10**(2): p. 109-116.
41. Fitzer, E. and R. Weiss, *Effect of surface treatment and sizing of c-fibres on the mechanical properties of cfr thermosetting and thermoplastic polymers*. *Carbon*, 1987. **25**(4): p. 455-467.
42. Yumitori, S., D. Wang, and F.R. Jones, *The role of sizing resins in carbon fibre-reinforced polyethersulfone (PES)*. *Composites*, 1994. **25**(7): p. 698-705.
43. Naoki, S. and M. Norihito, *Sizing agent for carbon fiber, method for sizing carbon fiber by said sizing agent, sized carbon fiber and knitted or woven fabric Using said carbon fiber*. US 20040197555 A1, 2006.
44. Broyles, N.S., et al., *Sizing of carbon fibres with aqueous solutions of poly(vinyl pyrrolidone)*. *Polymer*, 1998. **39**(12): p. 2607-2613.
45. *Adhesion of Graphite Fibers to Epoxy Matrices: II. The Effect of Fiber Finish*. *The Journal of Adhesion*, 1983. **16**(2): p. 133-152.
46. Dai, Z., et al., *Effect of sizing on carbon fiber surface properties and fibers/epoxy interfacial adhesion*. *Applied Surface Science*, 2011. **257**(15): p. 6980-6985.
47. Novoselov, K.S., et al., *Electric field effect in atomically thin carbon films*. *science*, 2004. **306**(5696): p. 666-669.
48. Geim, A.K. and K.S. Novoselov, *The rise of graphene*. *Nature materials*, 2007. **6**(3): p. 183-191.
49. Singh, V., et al., *Graphene based materials: Past, present and future*. *Progress in Materials Science*, 2011. **56**(8): p. 1178-1271.
50. Jiang, J.-W., J.-S. Wang, and B. Li, *Young's modulus of graphene: a molecular dynamics study*. *Physical Review B*, 2009. **80**(11): p. 113405.
51. Lee, J.-U., D. Yoon, and H. Cheong, *Estimation of Young's modulus of graphene by Raman spectroscopy*. *Nano letters*, 2012. **12**(9): p. 4444-4448.
52. Lee, C., et al., *Measurement of the elastic properties and intrinsic strength of monolayer graphene*. *science*, 2008. **321**(5887): p. 385-388.
53. Lee, C., et al., *Elastic and frictional properties of graphene*. *physica status solidi (b)*, 2009. **246**(11 - 12): p. 2562-2567.
54. Suk, J.W., et al., *Mechanical properties of monolayer graphene oxide*. *ACS nano*, 2010. **4**(11): p. 6557-6564.
55. Bolotin, K.I., et al., *Ultrahigh electron mobility in suspended graphene*. *Solid State Communications*, 2008. **146**(9): p. 351-355.
56. Kim, P., et al., *Thermal transport measurements of individual multiwalled nanotubes*. *Physical review letters*, 2001. **87**(21): p. 215502.
57. Pop, E., et al., *Thermal conductance of an individual single-wall carbon nanotube above room temperature*. *Nano letters*, 2006. **6**(1): p. 96-100.
58. Balandin, A.A., et al., *Superior thermal conductivity of single-layer graphene*. *Nano letters*, 2008. **8**(3): p. 902-907.
59. Klemens, P., *Theory of thermal conduction in thin ceramic films*. *International journal of thermophysics*, 2001. **22**(1): p. 265-275.
60. Ghosh, S., et al., *Extremely high thermal conductivity of graphene: Prospects for thermal management applications in nanoelectronic circuits*. *Applied Physics Letters*, 2008. **92**(15): p. 151911.

61. Nair, R.R., et al., *Fine structure constant defines visual transparency of graphene*. Science, 2008. **320**(5881): p. 1308-1308.
62. Bae, S., et al., *Roll-to-roll production of 30-inch graphene films for transparent electrodes*. Nat Nano, 2010. **5**(8): p. 574-578.
63. Kumar, A. and C.H. Lee, *Synthesis and biomedical applications of graphene: present and future trends*. Advances in Graphene Science, 2013: p. 5772-5578.
64. Yu, H., et al., *High-efficient Synthesis of Graphene Oxide Based on Improved Hummers Method*. 2016. **6**: p. 36143.
65. Blake, P., et al., *Making graphene visible*. Applied Physics Letters, 2007. **91**(6): p. 063124.
66. Shearer, C.J., et al., *Accurate thickness measurement of graphene*. Nanotechnology, 2016. **27**(12): p. 125704.
67. Ferrari, A.C., et al., *Raman spectrum of graphene and graphene layers*. Physical review letters, 2006. **97**(18): p. 187401.
68. Somani, P.R., S.P. Somani, and M. Umeno, *Planer nano-graphenes from camphor by CVD*. Chemical Physics Letters, 2006. **430**(1): p. 56-59.
69. Stankovich, S., et al., *Synthesis of graphene-based nanosheets via chemical reduction of exfoliated graphite oxide*. Carbon, 2007. **45**(7): p. 1558-1565.
70. Cao, H., et al., *Large-scale graphitic thin films synthesized on Ni and transferred to insulators: Structural and electronic properties*. Journal of Applied Physics, 2010. **107**(4): p. 044310.
71. Bhaviripudi, S., et al., *Role of Kinetic Factors in Chemical Vapor Deposition Synthesis of Uniform Large Area Graphene Using Copper Catalyst*. Nano Letters, 2010. **10**(10): p. 4128-4133.
72. Kim, K.S., et al., *Large-scale pattern growth of graphene films for stretchable transparent electrodes*. nature, 2009. **457**(7230): p. 706-710.
73. Stankovich, S., et al., *Graphene-based composite materials*. nature, 2006. **442**(7100): p. 282-286.
74. Verdejo, R., et al., *Functionalized graphene sheet filled silicone foam nanocomposites*. Journal of Materials Chemistry, 2008. **18**(19): p. 2221-2226.
75. Schniepp, H.C., et al., *Functionalized single graphene sheets derived from splitting graphite oxide*. The Journal of Physical Chemistry B, 2006. **110**(17): p. 8535-8539.
76. Gilje, S., et al., *A chemical route to graphene for device applications*. Nano letters, 2007. **7**(11): p. 3394-3398.
77. Gómez-Navarro, C., et al., *Electronic transport properties of individual chemically reduced graphene oxide sheets*. Nano letters, 2007. **7**(11): p. 3499-3503.
78. Nieto, A., D. Lahiri, and A. Agarwal, *Synthesis and properties of bulk graphene nanoplatelets consolidated by spark plasma sintering*. Carbon, 2012. **50**(11): p. 4068-4077.
79. Shen, J., et al., *Synthesis of amphiphilic graphene nanoplatelets*. small, 2009. **5**(1): p. 82-85.
80. Wang, G., et al., *Facile synthesis and characterization of graphene nanosheets*. The Journal of Physical Chemistry C, 2008. **112**(22): p. 8192-8195.
81. Zhu, C., et al., *Reducing sugar: new functional molecules for the green synthesis of graphene nanosheets*. ACS nano, 2010. **4**(4): p. 2429-2437.
82. Dreyer, D.R., et al., *The chemistry of graphene oxide*. Chemical Society Reviews, 2010. **39**(1): p. 228-240.
83. Loh, K.P., et al., *The chemistry of graphene*. Journal of Materials Chemistry, 2010. **20**(12): p. 2277-2289.

84. Mkhoyan, K.A., et al., *Atomic and electronic structure of graphene-oxide*. Nano letters, 2009. **9**(3): p. 1058-1063.
85. Mei, Q., et al., *Highly efficient photoluminescent graphene oxide with tunable surface properties*. Chemical Communications, 2010. **46**(39): p. 7319-7321.
86. Kumar, N.A., et al., *Polyaniline-grafted reduced graphene oxide for efficient electrochemical supercapacitors*. ACS nano, 2012. **6**(2): p. 1715-1723.
87. Li, W., et al., *Simultaneous surface functionalization and reduction of graphene oxide with octadecylamine for electrically conductive polystyrene composites*. Carbon, 2011. **49**(14): p. 4724-4730.
88. Xu, Z., et al., *Covalent functionalization of graphene oxide with biocompatible poly (ethylene glycol) for delivery of paclitaxel*. ACS applied materials & interfaces, 2014. **6**(19): p. 17268-17276.
89. Xu, Y., et al., *Strong and ductile poly (vinyl alcohol)/graphene oxide composite films with a layered structure*. Carbon, 2009. **47**(15): p. 3538-3543.
90. Yang, Y., et al., *Synthesis of PNIPAM polymer brushes on reduced graphene oxide based on click chemistry and RAFT polymerization*. Journal of Polymer Science Part A: Polymer Chemistry, 2012. **50**(2): p. 329-337.
91. Gong, L., et al., *Nylon-6/Graphene composites modified through polymeric modification of graphene*. Composites Part B: Engineering, 2015. **73**: p. 49-56.
92. Yu, D. and L. Dai, *Self-assembled graphene/carbon nanotube hybrid films for supercapacitors*. The Journal of Physical Chemistry Letters, 2009. **1**(2): p. 467-470.
93. Youn, D.H., et al., *Highly active and stable hydrogen evolution electrocatalysts based on molybdenum compounds on carbon nanotube–graphene hybrid support*. ACS nano, 2014. **8**(5): p. 5164-5173.
94. Yu, D., et al., *Scalable synthesis of hierarchically structured carbon nanotube-graphene fibres for capacitive energy storage*. Nature nanotechnology, 2014. **9**(7): p. 555-562.
95. Zhu, Y., et al., *A seamless three-dimensional carbon nanotube graphene hybrid material*. Nature communications, 2012. **3**: p. 1225.
96. Zhao, H. and J. Bai, *Highly Sensitive Piezo-Resistive Graphite Nanoplatelet–Carbon Nanotube Hybrids/Polydimethylsilicone Composites with Improved Conductive Network Construction*. ACS Applied Materials & Interfaces, 2015. **7**(18): p. 9652-9659.
97. Kuilla, T., et al., *Recent advances in graphene based polymer composites*. Progress in polymer science, 2010. **35**(11): p. 1350-1375.
98. Saheb, D.N. and J.P. Jog, *Natural fiber polymer composites: a review*. Advances in polymer technology, 1999. **18**(4): p. 351-363.
99. Kovac, J., *Comprehensive Desk Reference of Polymer Characterization and Analysis (edited by Robert F. Brady, Jr.)*. Journal of Chemical Education, 2004. **81**(10): p. 1425.
100. Jin, F.-L., X. Li, and S.-J. Park, *Synthesis and application of epoxy resins: A review*. Journal of Industrial and Engineering Chemistry, 2015. **29**: p. 1-11.
101. Kwak, G.H., S.J. Park, and J.R. Lee, *Thermal stability and mechanical behavior of cycloaliphatic–DGEBA epoxy blend system initiated by cationic latent catalyst*. Journal of applied polymer science, 2000. **78**(2): p. 290-297.
102. Park, S.-J., F.-L. Jin, and J.-R. Lee, *Thermal and mechanical properties of tetrafunctional epoxy resin toughened with epoxidized soybean oil*. Materials Science and Engineering: A, 2004. **374**(1): p. 109-114.
103. Lee, M.C., T.H. Ho, and C.S. Wang, *Synthesis of tetrafunctional epoxy resins and their modification with polydimethylsiloxane for electronic application*. Journal of applied polymer science, 1996. **62**(1): p. 217-225.

104. Yoo, M.J., et al., *Investigation of curing kinetics of various cycloaliphatic epoxy resins using dynamic thermal analysis*. European Polymer Journal, 2010. **46**(5): p. 1158-1162.
105. Jin, F.-L., C.-J. Ma, and S.-J. Park, *Thermal and mechanical interfacial properties of epoxy composites based on functionalized carbon nanotubes*. Materials Science and Engineering: A, 2011. **528**(29): p. 8517-8522.
106. Bascom, W., et al., *The fracture of epoxy - and elastomer - modified epoxy polymers in bulk and as adhesives*. Journal of Applied Polymer Science, 1975. **19**(9): p. 2545-2562.
107. Ferdosian, F., M. Ebrahimi, and A. Jannesari, *Curing kinetics of solid epoxy/DDM/nanoclay: Isoconversional models versus fitting model*. Thermochimica Acta, 2013. **568**: p. 67-73.
108. Ahmad, Z., M.P. Ansell, and D. Smedley, *Effect of nano-and micro-particle additions on moisture absorption in thixotropic room temperature cure epoxy-based adhesives for bonded-in timber connections*. International Journal of Adhesion and Adhesives, 2010. **30**(6): p. 448-455.
109. Jiang, W., F.-L. Jin, and S.-J. Park, *Thermo-mechanical behaviors of epoxy resins reinforced with nano-Al₂O₃ particles*. Journal of Industrial and Engineering Chemistry, 2012. **18**(2): p. 594-596.
110. Anwar, Z., et al., *Advances in epoxy/graphene nanoplatelet composite with enhanced physical properties: A review*. Polymer-Plastics Technology and Engineering, 2016. **55**(6): p. 643-662.
111. Balberg, I., *A comprehensive picture of the electrical phenomena in carbon black-polymer composites*. Carbon, 2002. **40**(2): p. 139-143.
112. Gao, F., *Clay/polymer composites: the story*. Materials today, 2004. **7**(11): p. 50-55.
113. Andrews, R. and M. Weisenberger, *Carbon nanotube polymer composites*. Current Opinion in Solid State and Materials Science, 2004. **8**(1): p. 31-37.
114. Zhu, R., et al., *Fused silver nanowires with metal oxide nanoparticles and organic polymers for highly transparent conductors*. ACS nano, 2011. **5**(12): p. 9877-9882.
115. Ku, H., et al., *A review on the tensile properties of natural fiber reinforced polymer composites*. Composites Part B: Engineering, 2011. **42**(4): p. 856-873.
116. Carotenuto, G., et al. *Graphene-polymer composites*. in *IOP Conference Series: Materials Science and Engineering*. 2012. IOP Publishing.
117. Wei, J., T. Vo, and F. Inam, *Epoxy/graphene nanocomposites-processing and properties: a review*. RSC Advances, 2015. **5**(90): p. 73510-73524.
118. Wan, Y.-J., et al., *Mechanical properties of epoxy composites filled with silane-functionalized graphene oxide*. Composites Part A: Applied Science and Manufacturing, 2014. **64**: p. 79-89.
119. Fang, M., et al., *Constructing hierarchically structured interphases for strong and tough epoxy nanocomposites by amine-rich graphene surfaces*. Journal of Materials Chemistry, 2010. **20**(43): p. 9635-9643.
120. Jia, J., et al., *Exceptional electrical conductivity and fracture resistance of 3D interconnected graphene foam/epoxy composites*. ACS nano, 2014. **8**(6): p. 5774-5783.
121. Li, Q., et al., *Ultrahigh thermal conductivity of assembled aligned multilayer graphene/epoxy composite*. Chemistry of Materials, 2014. **26**(15): p. 4459-4465.
122. Chatterjee, S., et al., *Size and synergy effects of nanofiller hybrids including graphene nanoplatelets and carbon nanotubes in mechanical properties of epoxy composites*. Carbon, 2012. **50**(15): p. 5380-5386.

123. Wang, F., et al., *Mechanical properties and thermal conductivity of graphene nanoplatelet/epoxy composites*. Journal of Materials Science, 2015. **50**(3): p. 1082-1093.
124. Wajid, A.S., et al., *High - Performance Pristine Graphene/Epoxy Composites With Enhanced Mechanical and Electrical Properties*. Macromolecular Materials and Engineering, 2013. **298**(3): p. 339-347.
125. Rafiee, M.A., et al., *Enhanced mechanical properties of nanocomposites at low graphene content*. ACS nano, 2009. **3**(12): p. 3884-3890.
126. Tang, L.-C., et al., *The effect of graphene dispersion on the mechanical properties of graphene/epoxy composites*. Carbon, 2013. **60**: p. 16-27.
127. Song, S.H., et al., *Enhanced Thermal Conductivity of Epoxy–Graphene Composites by Using Non - Oxidized Graphene Flakes with Non - Covalent Functionalization*. Advanced Materials, 2013. **25**(5): p. 732-737.
128. King, J.A., et al., *Mechanical properties of graphene nanoplatelet/epoxy composites*. Journal of Applied Polymer Science, 2013. **128**(6): p. 4217-4223.
129. Wajid, A.S., et al., *High-Performance Pristine Graphene/Epoxy Composites With Enhanced Mechanical and Electrical Properties*. Macromolecular Materials and Engineering, 2013. **298**(3): p. 339-347.
130. Ahmadi-Moghadam, B., et al., *Effect of functionalization of graphene nanoplatelets on the mechanical response of graphene/epoxy composites*. Materials & Design (1980-2015), 2015. **66**: p. 142-149.
131. Wan, Y.-J., et al., *Grafting of epoxy chains onto graphene oxide for epoxy composites with improved mechanical and thermal properties*. Carbon, 2014. **69**: p. 467-480.
132. Teng, C.-C., et al., *Thermal conductivity and structure of non-covalent functionalized graphene/epoxy composites*. Carbon, 2011. **49**(15): p. 5107-5116.
133. Wang, X., et al., *Covalent functionalization of graphene with organosilane and its use as a reinforcement in epoxy composites*. Composites Science and Technology, 2012. **72**(6): p. 737-743.
134. Chandrasekaran, S., C. Seidel, and K. Schulte, *Preparation and characterization of graphite nano-platelet (GNP)/epoxy nano-composite: Mechanical, electrical and thermal properties*. European Polymer Journal, 2013. **49**(12): p. 3878-3888.
135. Qi, B., et al., *Enhanced thermal and mechanical properties of epoxy composites by mixing thermotropic liquid crystalline epoxy grafted graphene oxide*. Express Polymer Letters, 2014. **8**(7).
136. Zaman, I., et al., *A Facile Approach to Chemically Modified Graphene and its Polymer Nanocomposites*. Advanced Functional Materials, 2012. **22**(13): p. 2735-2743.
137. Shahil, K.M.F. and A.A. Balandin, *Graphene–Multilayer Graphene Nanocomposites as Highly Efficient Thermal Interface Materials*. Nano Letters, 2012. **12**(2): p. 861-867.
138. Ni, Y., et al., *Superior mechanical properties of epoxy composites reinforced by 3D interconnected graphene skeleton*. ACS applied materials & interfaces, 2015. **7**(21): p. 11583-11591.
139. Agarwal, B.D., L.J. Broutman, and K. Chandrashekhara, *Analysis and performance of fiber composites*. 2006: John Wiley & Sons.
140. Cecen, V., et al., *FTIR and SEM analysis of polyester - and epoxy - based composites manufactured by VARTM process*. Journal of applied polymer science, 2008. **108**(4): p. 2163-2170.
141. Fairuz, A., et al., *Polymer composite manufacturing using a pultrusion process: a review*. American Journal of Applied Sciences, 2014. **11**(10): p. 1798.

142. Memon, A. and A. Nakai, *Mechanical Properties of Jute Spun Yarn/PLA Tubular Braided Composite by Pultrusion Molding*. Energy Procedia, 2013. **34**: p. 818-829.
143. Wan, Y.Z., et al., *Three-dimensionally braided carbon fiber–epoxy composites, a new type of materials for osteosynthesis devices. II. Influence of fiber surface treatment*. Journal of Applied Polymer Science, 2002. **85**(5): p. 1040-1046.
144. Dhakate, S.R. and O.P. Bahl, *Effect of carbon fiber surface functional groups on the mechanical properties of carbon–carbon composites with HTT*. Carbon, 2003. **41**(6): p. 1193-1203.
145. Sharma, S.P. and S.C. Lakkad, *Effect of CNTs growth on carbon fibers on the tensile strength of CNTs grown carbon fiber-reinforced polymer matrix composites*. Composites Part A: Applied Science and Manufacturing, 2011. **42**(1): p. 8-15.
146. Manocha, L.M., H. Bhatt, and S.M. Manocha, *Development of carbon/carbon composites by co-carbonization of phenolic resin and oxidised pan fibers*. Carbon, 1996. **34**(7): p. 841-849.
147. Lee, S.M., *Handbook of composite reinforcements*. 1992: John Wiley & Sons.
148. Lodge, K., *The electrical properties of joints in carbon fibre composites*. Composites, 1982. **13**(3): p. 305-310.
149. Deierling, P. and O. Zhupanska, *Experimental study of high electric current effects in carbon/epoxy composites*. Composites Science and Technology, 2011. **71**(14): p. 1659-1664.
150. Gallego, N., et al., *The thermal conductivity of ribbon-shaped carbon fibers*. Carbon, 2000. **38**(7): p. 1003-1010.
151. Gandikota, V., G.F. Jones, and A.S. Fleischer, *Thermal performance of a carbon fiber composite material heat sink in an FC-72 thermosyphon*. Experimental Thermal and Fluid Science, 2010. **34**(5): p. 554-561.
152. Young, R.J. and P.A. Lovell, *Introduction to polymers*. 2011: CRC press.
153. Cox, H., *The elasticity and strength of paper and other fibrous materials*. British journal of applied physics, 1952. **3**(3): p. 72.
154. Hsueh, C.-H., *A two-dimensional stress transfer model for platelet reinforcement*. Composites Engineering, 1994. **4**(10): p. 1033-1043.
155. Young, R.J., et al., *The mechanics of graphene nanocomposites: a review*. Composites Science and Technology, 2012. **72**(12): p. 1459-1476.
156. Gong, L., et al., *Interfacial stress transfer in a graphene monolayer nanocomposite*. Advanced Materials, 2010. **22**(24): p. 2694-2697.
157. Young, R.J., et al., *Strain mapping in a graphene monolayer nanocomposite*. Acs Nano, 2011. **5**(4): p. 3079-3084.
158. Jang, H.-K., et al., *Interfacial shear strength of reduced graphene oxide polymer composites*. Carbon, 2014. **77**: p. 390-397.
159. Liu, Y., A.-L. Hamon, and J. Bai, *Directly measuring interfacial shear strength between Polymethyl methacrylate and graphene nanoplatelets*. Materials Letters, 2016. **182**: p. 244-247.
160. Li, X., J. Warzywoda, and G.B. McKenna, *Mechanical responses of a polymer graphene-sheet nano-sandwich*. Polymer, 2014. **55**(19): p. 4976-4982.
161. Cai, M., et al. *Direct measurement of the interfacial attractions between functionalized graphene and polymers in nanocomposites*. in *AIP Conference Proceedings*. 2010. AIP.
162. RamanathanT, et al., *Functionalized graphene sheets for polymer nanocomposites*. Nat Nano, 2008. **3**(6): p. 327-331.

163. DiFrancia, C., T.C. Ward, and R.O. Claus, *The single-fibre pull-out test. I: Review and interpretation*. Composites Part A: Applied Science and Manufacturing, 1996. **27**(8): p. 597-612.
164. Favre, J.-P. and M.-C. Merienne, *Characterization of fibre/resin bonding in composites using a pull-out test*. International journal of adhesion and adhesives, 1981. **1**(6): p. 311-316.
165. Pitkethly, M.J., et al., *A round-robin programme on interfacial test methods*. Composites Science and Technology, 1993. **48**(1): p. 205-214.
166. Miller, B., U. Gaur, and D.E. Hirt, *Measurement and mechanical aspects of the microbond pull-out technique for obtaining fiber/resin interfacial shear strength*. Composites science and technology, 1991. **42**(1-3): p. 207-219.
167. Rahmani, N., et al., *The effect of post cure temperature on fiber/matrix adhesion of T650/Cycom 5320-1 using the micro-droplet technique*. Polymer Testing, 2015. **46**: p. 14-20.
168. Sockalingam, S. and G. Nilakantan, *Fiber-matrix interface characterization through the microbond test*. International Journal Aeronautical and Space Sciences, 2012. **13**(3): p. 282-295.
169. Mandell, J., J. Chen, and F. McGarry, *A microdebonding test for in situ assessment of fibre/matrix bond strength in composite materials*. International Journal of Adhesion and Adhesives, 1980. **1**(1): p. 40-44.
170. Miller, B., P. Muri, and L. Rebenfeld, *A microbond method for determination of the shear strength of a fiber/resin interface*. Composites Science and Technology, 1987. **28**(1): p. 17-32.
171. Dilandro, L., A.T. Dibenedetto, and J. Groeger, *The effect of fiber-matrix stress transfer on the strength of fiber-reinforced composite materials*. Polymer Composites, 1988. **9**(3): p. 209-221.
172. Lacroix, T., et al., *Modelling of critical fibre length and interfacial debonding in the fragmentation testing of polymer composites*. Composites science and technology, 1992. **43**(4): p. 379-387.
173. Adhikari, R. and G.H. Michler, *Polymer nanocomposites characterization by microscopy*. Journal of Macromolecular Science®, Part C: Polymer Reviews, 2009. **49**(3): p. 141-180.
174. Wu, Q., et al., *Imaging the interphase of carbon fiber composites using transmission electron microscopy: Preparations by focused ion beam, ion beam etching, and ultramicrotomy*. Chinese Journal of Aeronautics, 2015. **28**(5): p. 1529-1538.
175. Wirth, R., *Focused Ion Beam (FIB) combined with SEM and TEM: Advanced analytical tools for studies of chemical composition, microstructure and crystal structure in geomaterials on a nanometre scale*. Chemical Geology, 2009. **261**(3): p. 217-229.
176. Zankel, A., et al., *Ultramicrotomy in the ESEM, a versatile method for materials and life sciences*. Journal of Microscopy, 2009. **233**(1): p. 140-148.
177. Egerton, R.F., *Electron energy-loss spectroscopy in the electron microscope*. 2011: Springer Science & Business Media.
178. Egerton, R.F., *Electron energy-loss spectroscopy in the TEM*. Reports on Progress in Physics, 2008. **72**(1): p. 016502.

Chapter 2 Surface treatment of the reinforcements

Introduction

In this chapter, I introduce the different surface treatment methods applied to the reinforcements. Two series of reinforcements on a micrometer scale, CFs and graphene-based materials, are used here.

To improve the interaction between nanofillers and polymer matrix, two major routes are used in this thesis:

- (1) introducing a “strong” chemical bonding [1];
- (2) and increasing the surface roughness [2].

Chemical oxidation is a representation of the first strategy. For graphene-based materials, graphene oxide (GO) is an ideal candidate for nanofillers in composites with enhanced interface interactions and strength, due to the abundant functional groups on the surface. It results in a high efficiency of the load transfer and in improved mechanical properties. However, after treatment by a strong acid, the mechanical properties of GO have decreased largely. Hence, in this thesis, I also introduce a moderate oxidation method, i.e. the reinforcements are heated up to a given temperature in atmospheric conditions. The oxidized graphite nano-platelets (O-GNPs) are prepared by this method.

The latter strategy, the increase of surface roughness, is also known as a physical reinforcement. Depositing nanoparticles and grafting carbon nanotubes (CNTs) on graphitic surfaces are the most used methods. Our group has achieved excellent research works on the

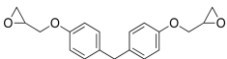
investigation of the synthesis of graphite nanoplatelets CNT-GNP and CNT-CF hybrids. Both hybrids are fabricated in this thesis. I also fabricate the oxidized CNT-CFs by combining physical and chemical modifications.

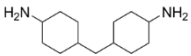
The detailed information of the filler preparation and characterization are provided in this chapter. The basic characterization results, including microscopy (TEM, SEM), TGA, Fourier transform Infra-red (FT-IR), X-ray photoelectron spectroscopy (XPS) and Raman spectroscopy, are analyzed to confirm the successful synthesis of the fillers.

2.1 Materials

All the information on the materials used for experiments are listed in **Table 2.1** including their names, molecular formula, physical states, purities and providers.

Table 2.1 Materials for experiments.

Materials	Molecular formula (Structure)	Physical states	Purity	Notes
CF (T700GC)				Toray Carbon Fibers America, Inc.
GNPs (G5)		<i>s</i> *		KNANO Science Inc.
Ferrocene	Fe(C ₅ H ₅) ₂	<i>s</i>		
Potassium manganate	KMnO ₄	<i>s</i>	CP	
Acetone	CO(CH ₃) ₂	<i>l</i> *	99.8 %	
Dimethyl formamide	HCON(CH ₃) ₂	<i>l</i>	99.8 %	Sigma Aldrich
Ethanol	C ₂ H ₅ OH	<i>l</i>	96 %	
Sulfuric acid	H ₂ SO ₄	<i>l</i>	98 %	
Hydrogen chloride	HCl	<i>l</i>	30 %	
Hydrogen peroxide	H ₂ O ₂	<i>l</i>	30 %	
Argon	Ar	<i>g</i> *		Carrier gas
Hydrogen	H ₂	<i>g</i>		Carrier gas
Acetylene	C ₂ H ₂	<i>g</i>		Carbon source
Bisphenol F-(epichlohydrin) (1080s)		<i>l</i>		Resoltech

4-4'-methylenebis (cyclohexylamine) (1084)		<i>l</i>	Resoltech
--	---	----------	-----------

* *s*, *l* and *g* stand respectively for solid, liquid and gas phase

2.2 Experiment

2.2.1 Synthesis of CNT-CFs and CNT-GNPs

The growth of CNTs on CFs was carried out in a chemical vapor deposition (CVD) quartz tube with a diameter of 100 mm, which was heated by an electrical resistance furnace (CARBOLITE®). One kind of T700 grade CF fabric was used in this study. Its diameter was around 7 μm . The furnace was heated up to 600 °C in an argon and hydrogen flow with a rate of 1.2 and 0.3 L min^{-1} , respectively. After 10 min stabilization, a xylene solution containing 0.1 g ml^{-1} ferrocene was injected in form of spray into the reactor by a syringe injector, with an injection speed of 24 ml h^{-1} . The growth lasted 3 min for CNTs grafted on the CFs. The furnace was finally cooled down to room temperature under argon protective atmosphere (1 L min^{-1}) [3].

The CNT-GNP hybrid structure was produced by a CVD method. Acetylene (C_2H_2) was used as the carbon source and ferrocene ($\text{Fe}(\text{C}_5\text{H}_5)_2$) as the catalyst precursor. A typical process can be reduced to the following steps [4]:

1. The as received GNP powders (KNANO, China) were homogeneously spread on a quartz plate (4*30 cm^2) using a sieve, the plate was placed in a quartz tube reactor (120 cm in length, 45 mm in inner diameter) heated to 650 °C by a horizontal tube furnace (75 cm in length) under argon atmosphere.
2. The ferrocene, dissolved in xylene (C_2H_{10}) at a concentration of 0.05 g cm^{-1} , was injected into the reactor by a syringe system and carried to the stable reaction zone in the form of a spray by carrier gases (Ar and H_2).
3. Accompanying the injection of the catalyst solution, acetylene was also fed into the reactor simultaneously. The gas flow rate was controlled by electronic mass flow meters (Bronkhorst).
4. The CNT growth time was set to 15 min.

5. After growth, the system was cooled down to room temperature under argon atmosphere.

2.2.2 Modification of the different types of fillers: Graphene oxide (GO), desized CFs, oxidized GNPs (O-GNPs) and CNT-CFs

The modified Hummers method was used for the preparation of GO as described previously [5]. Briefly, 2 g of graphite powder was stirred into 50 mL of cooled (0 °C) and concentrated H₂SO₄. Then, 6 g of KMnO₄ was cooled gradually below 5 °C. After being stirred below 5 °C for 1 h, the mixture was heated up to a temperature of 35 °C and stirred for an additional 30 min. Then, 100 mL of distilled water was added slowly, and the temperature was maintained below 100 °C. Finally, 15 mL of 30 % H₂O₂ was added. The crude GO were filtered out, washed with a solution of 5 % HCl in distilled water at least three times and subsequently dialyzed for at least 48 h until SO₄²⁻ could not be detected by a BaCl₂ solution. GO were filtered out again and vacuum-dried at a temperature below 60 °C to obtain the dried target products.

The surface oxidation of GNPs was carried out in a quartz tube with a diameter of 100 mm, which was heated by an electrical resistance furnace (CARBOLITE). The GNPs were supported on a quartz plate (30 mm in width × 500 mm in length) placed in the center of the tube. The furnace was heated up to a temperature of 550°C in an open system and kept for 2 h, then cooled down to room temperature.

The as-prepared CNT-CFs were subsequently oxidized: they were heated up to a temperature of 400 °C and stabilized for 4 min in air. Since the commercial CFs are coated by a sizing layer and since the influence of this layer is best studied by comparing with the rough CFs (without this layer), a “desized process” has been conducted by heating the as-received CFs up to a temperature of 650°C for several minutes in an argon atmosphere [6].

2.3 Characterization results and discussion

The microstructure of different CF and graphene-based surfaces was observed by SEM (ZEISS, LEO 1530 Gemini) at 5 kV. A thermogravimetric analysis (TGA, NETZSCH STA 449 F3) was used to evaluate the mass fraction of CNTs grafted on the surface of a CF. Around 80 mg of chopped CNT-CF powders was heated from 30 to 900 °C at a rate of 10 °C/min. The atmosphere was a mixture of oxygen and nitrogen, with a flow rate of 20 mL/min. The same conditions were used to test the graphene-based materials. The X-ray photoelectron spectra

(XPS) were recorded on a THERMO VG ESCALAB 250 spectrometer equipped with a monochromatic RX K α Al (1486.6 eV) source. AVANTAGE 4.67 was used to analyze and deconvolute the XPS peaks. TEM imaging was performed using a Titan³ G2 (FEI) with a bright field emission gun (XFEG) operating at the chosen accelerating voltage of 80 kV to control the damage due to the electron beam on the sample.

2.3.1 Morphology characterization of the fillers

In this part, two types of electron microscopes are conducted, scanning electron microscope (SEM) and transmission electron microscope (TEM). The SEM is normally used for an overview observation of specimens. For the reinforcements, the lateral size and thickness of graphene, the length of CNTs and the diameter of CF are acquired from the SEM images. The TEM needs very thin samples but it has a much higher resolution compared to SEM, the plane structure of GNPs, the diameter of CNTs are acquired from the TEM images. The detailed information is shown as follows:

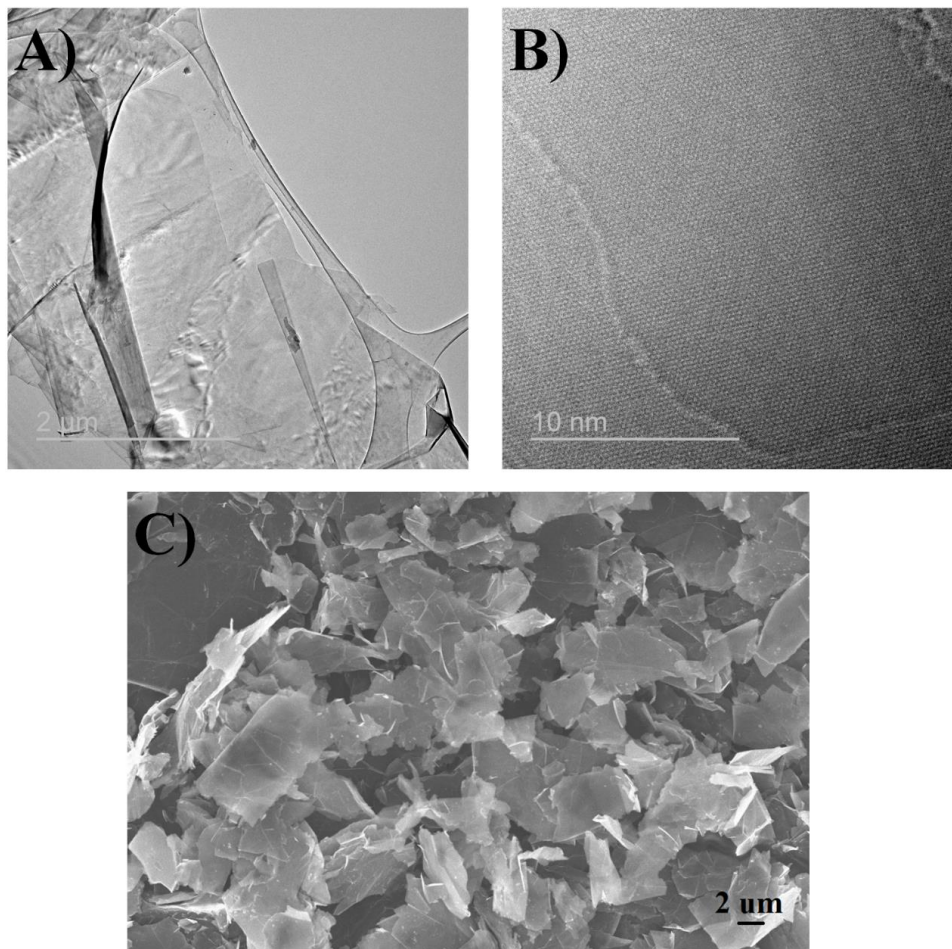


Figure 2.1 GNP morphology characterization: (A) low magnification TEM, (B) high resolution TEM images of GNP surface and (C) SEM image.

The TEM image of as-received GNPs are shown in **Figure 2.1A**. **Figure 2.1B** shows the high resolution TEM image of GNP surface. The regular hexagons can be easily distinguished with few defects. The SEM image of GNPs have showed semitransparent platelets in morphology with a diameter ranging from 5 to 10 μm . Additionally, from the information from the supplier, the GNPs have a very low-density due to its thinness.

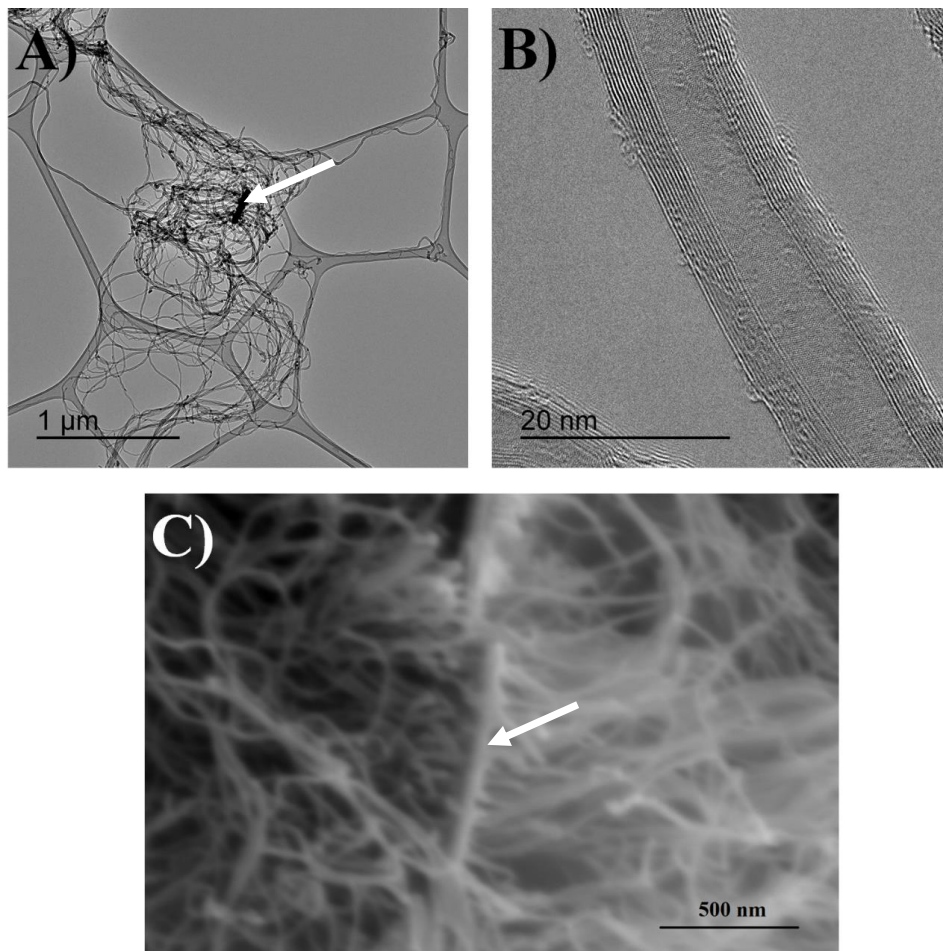


Figure 2.2 GNP-CNTs morphology characterization: (A) TEM of hybrids (The bright arrow shows the GNP), (B) high resolution TEM images of CNT (microscope and conditions) and (C) SEM image (The bright arrow shows the GNP).

CVD is one of the most popular methods used to produce CNTs. In this process, thermal decomposition of a hydrocarbon vapor is conducted in the presence of metallic catalyst. Differently with high temperature electric arc discharge technique, a medium temperature range can meet for the synthesis which makes CVD popular for CNT's synthesis. The temperature used for CVD is usually less than 1000 °C (in our system, 650 °C for the synthesis of GNP-CNTs and 600 °C for the CNT-CFs) and hydrocarbon compounds are decomposed on the substrate by inducing catalysts.

The GNP-CNTs hybrids were synthesized through the floating-catalyst CVD method without any pretreatment. C₂H₂ was selected as the carbon sources, and ferrocene served as the catalyst. The TEM image of hybrids in **Figure 2.2(A)** clearly shows the 1D-2D coupling structure, in which the dark bar-shape in the center (as marked out by a white arrow) is a GNP surrounded by the CNT clusters. **Figure 2.2(B)** shows the high resolution TEM image of CNTs grafted on the GNP. It has a diameter of 7-10 nm and a length of tens of micrometers. The SEM image of the hybrids is shown in **Figure 2.2(C)**. The CNTs are grafted and grown perpendicularly to the GNP surface. The lateral size of the GNP is lower than 1 μm.

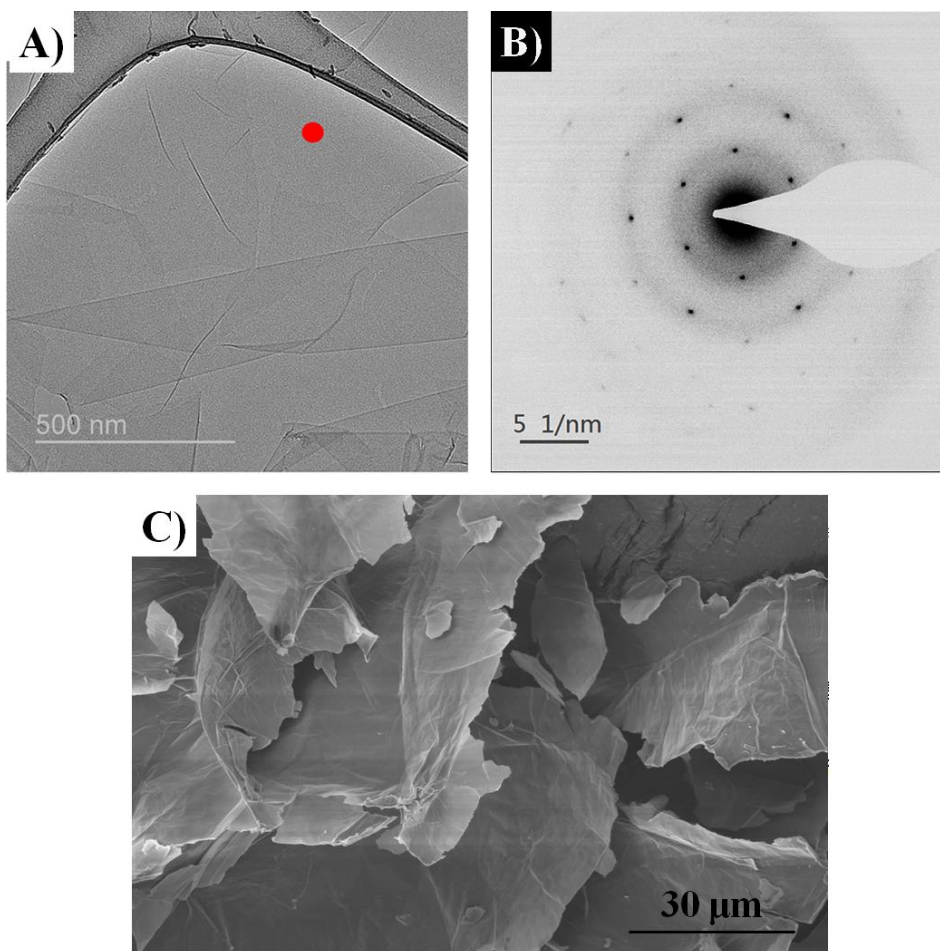


Figure 2.3 GO morphology characterization: (A) TEM image; (B) A selected area (SA) diffraction pattern of the GO taken on the red spot in (A); and (C) SEM image.

Figure 2.3(A) shows the TEM image of GOs. After ultrasonication, most of the GO platelets disperse into a monolayer state. We chose a zone to obtain the selected area (SA) diffraction pattern and it can be found that a portion of GO still maintains the crystal structure of the graphene due to the hexagonal pattern shown in the **Figure 2.3(B)** (Attention: to make the circle clearer, the image of diffraction pattern has been reversed to obtain a negative image); at the same time, the appearance of the dark circles indicates the amorphization of the graphene structure after oxidation. GO in **Figure 2.3(C)** appears with a much larger lateral size compared to that of GNPs. Based on the supplier's information, the lateral size of GO is around 7 μm. The far greater lateral size observed by SEM could be possibly attributed to the aggregation of several platelets during the drying process.

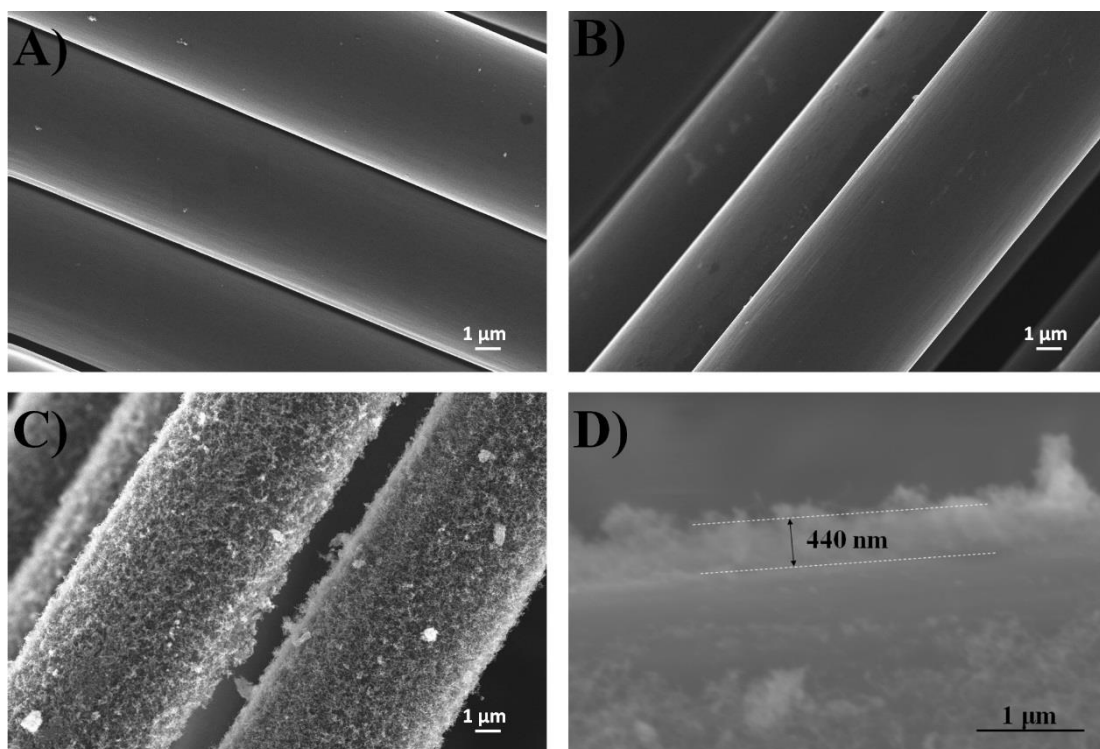


Figure 2.4 SEM images showing the CF morphology: (A) original CFs; (B) desized CFs; (C) CNT-grafted CFs; and (D) CNT-CF to measure the thickness of the CNT layer.

The morphologies of the raw CFs, desized CFs and CNT-CFs are shown in **Figure 2.4**. The raw fibers have a smooth and cylindrical surface with a diameter of around 7 μm (**Figure 2.4A**). After desizing, the CF surface has no obvious change and few difference could be detected at a SEM resolution scale (**Figure 2.4B**). The *in-situ* growth of homogeneous CNTs on the CFs was achieved by an easy one-step CVD method using the metalorganic compound ferrocene as a catalyst precursor. As shown in **Figure 2.4C**, the CNTs grow homogeneously on the whole surface of the fabric and on each CF. More importantly, each CF is covered by a continuous cylindrical shell consisting of aligned CNTs. The thickness of the CNT layer on the CF was measured by SEM, which can be seen in **Figure 2.4D**. A part of the CNT was removed manually (i.e. using a macroscopic tool) before the SEM observation. The thickness of the CNT layer is about 440 nm. The real thickness of the CNT layer may be larger than this value since the CF cylinder may not be tilted to the right position. To create some oxygen-containing groups on the CF and CNT surfaces, the CNT-CFs were heated up to a temperature of 400 $^{\circ}\text{C}$ in atmospheric condition for 3 min. No obvious change could be observed by SEM.

2.3.2 Basic characterization of the fillers

Thermogravimetric analysis (TGA)

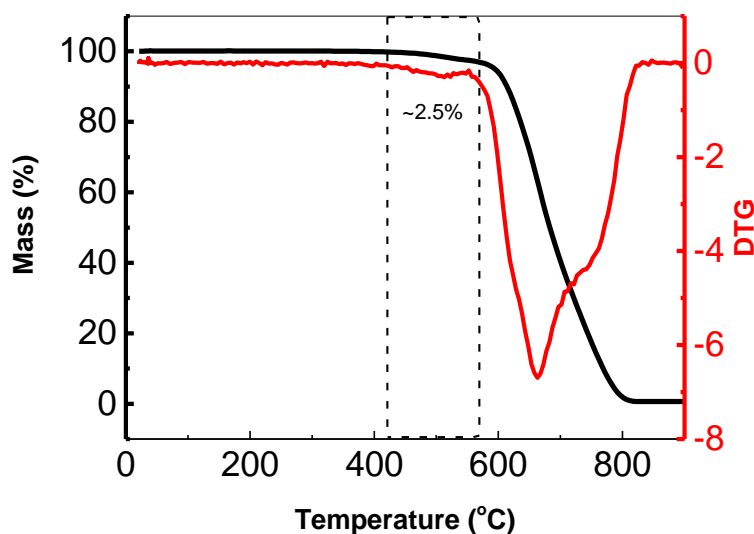


Figure 2.5 The thermogravimetric analysis (The black line) and the differential thermogravimetric (The red line) (TGA/DTG) curves of CNT-CFs.

The mass fraction of the CNTs grown on CFs could be evaluated by TGA/DTG analysis (**Figure 2.5**). CFs decompose above 600 °C. Due to the low percentage of CNTs, it is difficult to distinguish the CNT decomposition from the TG curve. However, if we study the DTG curve carefully, beside the large decomposition above 600 °C, there exists a small, broad peak around 500 °C, which corresponds to the CNT decomposition of 2.5 wt%, as I marked out by blue rectangle.

TGA measurements were used to confirm the decomposition temperature of GNPs, as shown in **Figure 2.6**. The as-received GNPs show a small weight loss below 600 °C, caused by the decomposition of some surface amorphous carbon. The major decomposition begins at 600 °C, and complete at 630 °C. After grafting CNTs on the GNP surface, the decomposition temperature of the hybrids shifts to a lower temperature, around 550 °C. The major decomposition temperature of CNTs is around 550 °C, which is responsible for this shift.

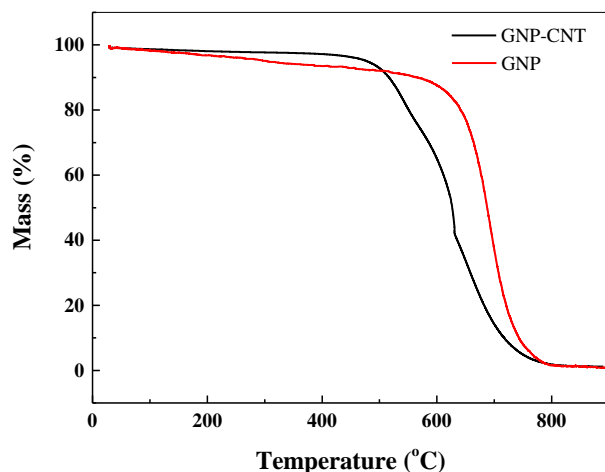


Figure 2.6 TGA curves of GNPs and CNT-GNPs.

X-ray photoelectron spectroscopy (XPS)

XPS can be used to analyze the surface chemistry of a material in its as-received state, or after surface treatment. In my experiment, the XPS spectra of different samples treated by grafting CNTs and oxidation are analyzed in this part.

The XPS spectra of four types of CFs were recorded to confirm the chemical composition on the surface. Selected results of the XPS studies showing fitted C1s peaks (284 eV) are given in **Figure 2.7**. This peak corresponds to the ionization of a K-shell (1s) electron of a carbon atom. With all fibers, typical asymmetric peaks in the C1s region are found. For the curve fitting of the peaks, the following functions have been considered: aromatic and aliphatic carbon, carbon in keto-enol equilibria (C_{ke}), carbonyl groups, hydroxyl groups and carboxylic groups [7]. The surface modification of the CFs was determined by measuring the oxygen content. For the raw CFs, due to the sizing layer, the oxygen content is increased to 31.8 %. After heating in argon atmosphere at 650°C for several minutes, the sizing layer could be removed completely. Based on the XPS results, the oxygen content is decreased to 6.2 %. From the C1s peak shown in **Figure 2.7A** and **B**, the difference is obvious: the C_{ke} peak dramatically decreased. Due to the quick heating process at 650 °C for several minutes, the decomposed sizing layer may redeposit on the CF surface, which leads to a residual oxygen content of 6.2 %. After grafting CNTs on CF surface, the C1s peak offers little change compared to the case of desized CFs. However, due to the CNT layer covering the CF surface, the oxygen content is decreased to 2.0 %, as shown in **Figure 2.7C**. Then, the CNT-CFs were

heated at 400 °C for 4 min, and the XPS results indicated that the oxygen content increased to 2.4%, which indicates that oxygen-containing groups have been introduced on the CF and CNT surfaces successfully.

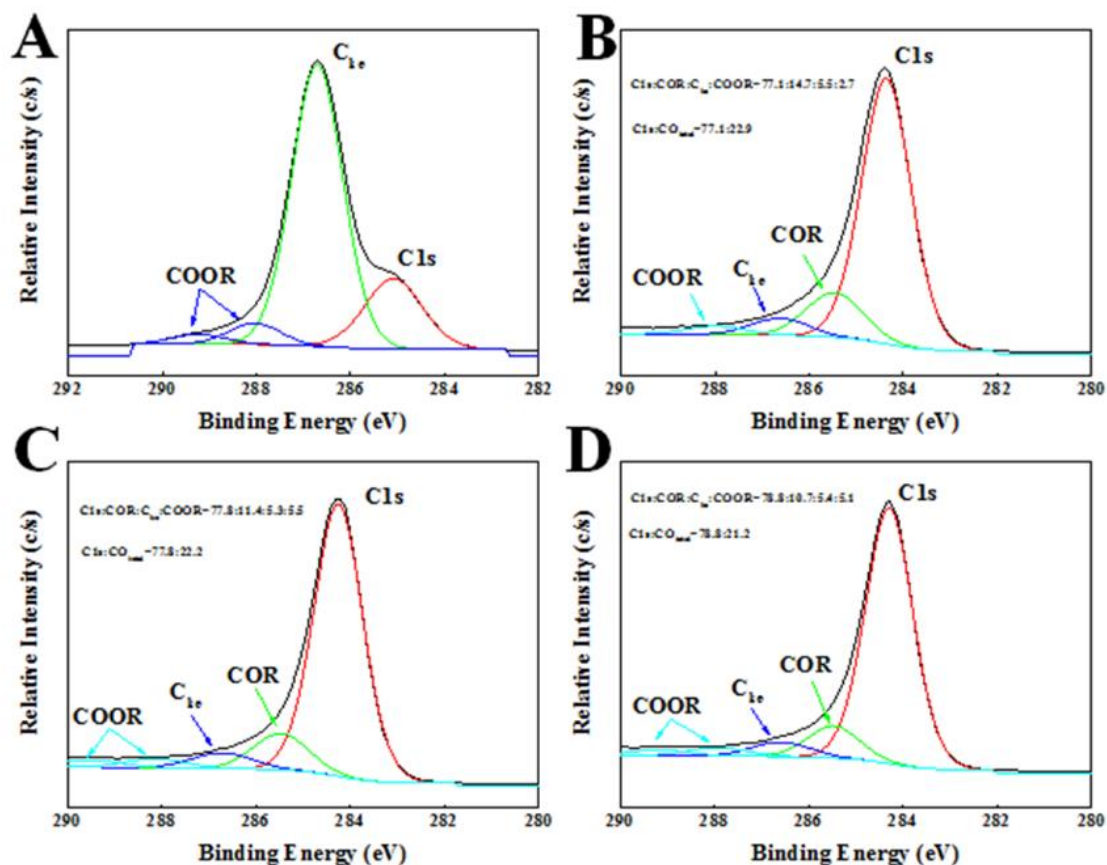


Figure 2.7 XPS spectra of the C1s region scan for (A) raw CFs, (B) desized CFs, (C) CNT-CFs and (D) oxidized CNT-CFs.

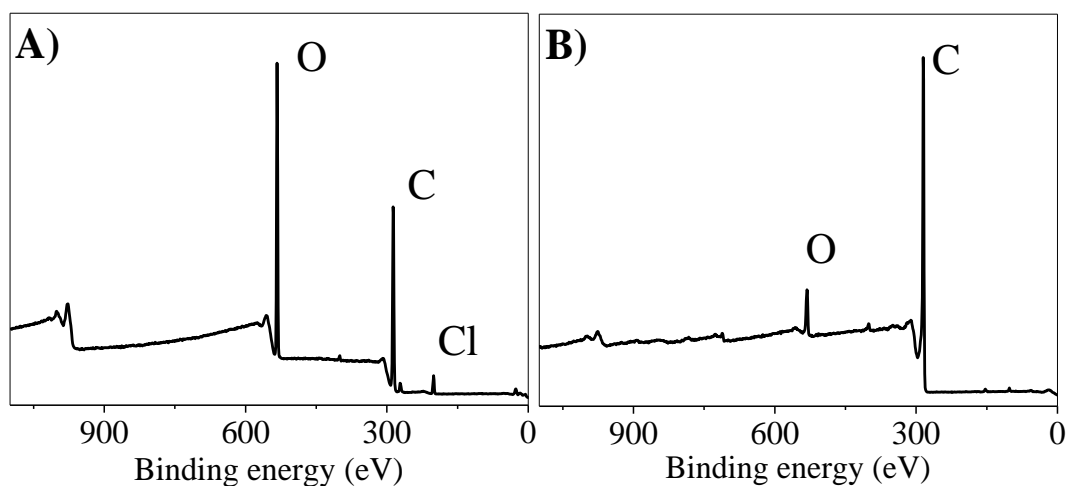


Figure 2.8 XPS spectra of the survey of (A) original CFs and (B) desized CFs.

Since the oxygen/carbon ratio is not obvious to reflect the difference between original and desized CFs. The survey scan of original CFs (**Figure 2.8A**) shows the presence of carbon, oxygen and chlorine elements; however, after desizing, only carbon and oxygen can be observed (**Figure 2.8B**). The disappearance of any clear Cl signal indicated the successful removing of the sizing layer.

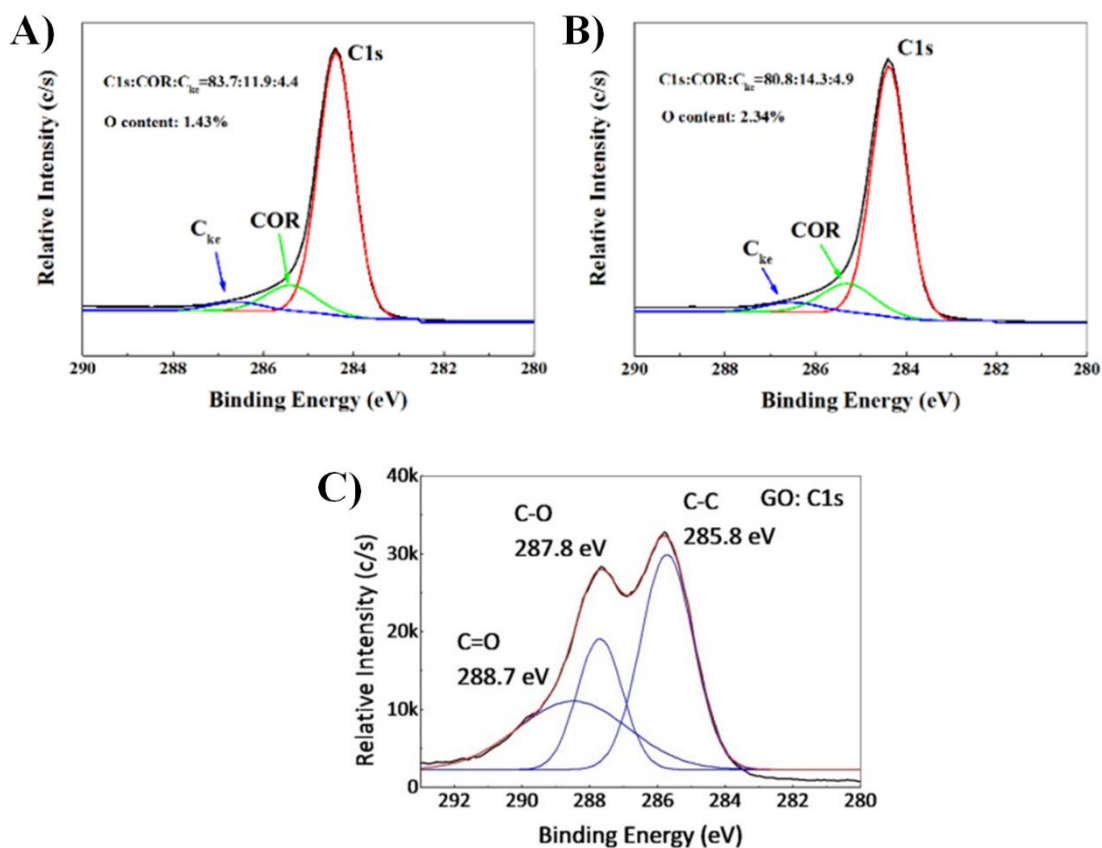


Figure 2.9 C1s XPS spectra of (A) original GNPs, (B) O-GNPs and (C) GOs.

To investigate the oxidation quality of O-GNPs and GOs, XPS spectra were conducted on both fillers, as shown in **Figure 2.9**. We fitted the C1s peaks in the spectra of (A) original GNPs, (B) O-GNPs and (C) GOs. Comparing the spectra of O-GNPs and original GNPs, no obvious difference could be observed in the curves, while a small increase of the O:C ratio was observed for original GNPs (1.43 %) and O-GNPs (2.34 %). An increase of the O:C ratio can mean that the degree of oxidation of oxidized GNPs is higher than for original GNPs. The C1s XPS spectra of GOs show three different binding energies for carbon atoms: one is from the C-C bond at 285.8 eV, and the other two that form a hump at 287-290 eV arise from the overlap

of two different carbon atoms (the O=C at 288.7 eV and the C-O at 287.8 eV), indicating the complete oxidation of the GNPs.

FT-IR and Raman spectroscopy of GO and GNPs

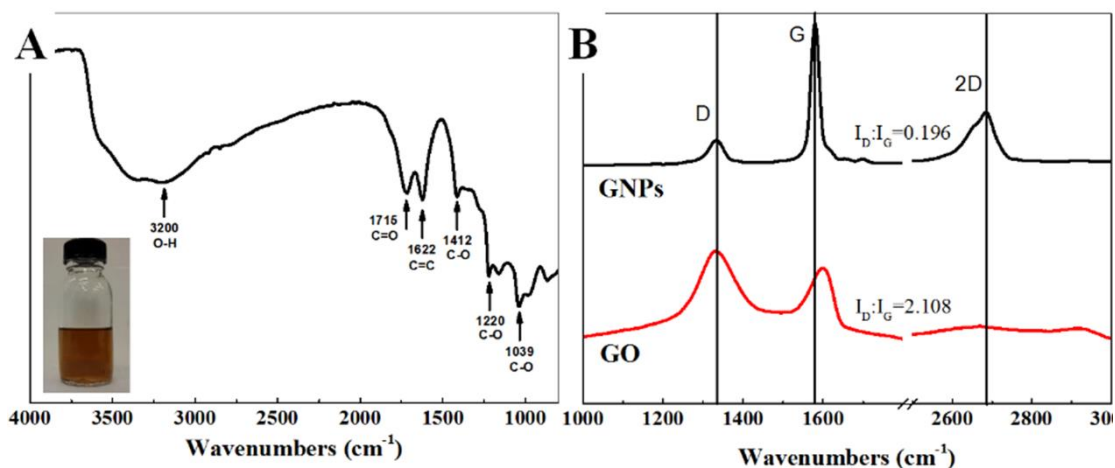


Figure 2.10 (A) Fourier-Transform infra-red (FT-IR) curve of GOs; the inserted image is a view of the GOs dispersed in ethanol by ultrasonication; (B) Raman spectra of GNPs and GOs.

Figure 2.10A shows the FT-IR curves of GOs. For GOs, the oxidation in sulfuric acid provided a typical absorption peak at 1715 cm^{-1} associated with the carboxyl group and an absorbency at approximately 1039 cm^{-1} , which corresponds to the other side groups. Other oxygen-containing groups were also marked out in the spectra.

In the Raman spectra shown in **Figure 2.10B**, the G5 exhibits a weak D band at 1350 cm^{-1} and an incisive G band at 1580 cm^{-1} . However, the D band of GO strongly increases while the G band shifts to higher wave numbers due to the graphite amorphization, which confirms the lattice distortions caused by oxidation. I also employ the ratio between D and G ($I_{D/G}$) to roughly estimate the oxidation degree of GOs. In the case of G5, this value is as low as 0.196. While in the case of GOs, this value increases to 2.108. Furthermore, the 2D band at 2700 cm^{-1} is highly sensitive to the stacking of graphene sheets [10]. The Raman spectrum of G5 shows an incisive band related to its few-layer structure. After oxidation, GO shows an obviously broadened peak with a lower intensity around 2700 cm^{-1} .

2.4 Partial conclusion

This chapter contains experimental and characterization works for the thesis. First, CNT-CFs and CNT-GNPs have been produced with *in-situ* grafting of CNTs on the surface of CFs and GNPs by CVD. Morphology characterization by TEM and SEM indicate that the CNTs are successfully grafted on the CF and GNP surface. For CNTs-CF, the length of CNTs is about 440 nm with a very dense array. The CNTs on GNP surface has a length of tens of micrometers. TGA is conducted to evaluate the mass fraction of CNTs grafted on the GNP and CF surfaces. Since CFs have a much higher decomposition temperature than CNTs, TGA is a suitable method to evaluate the amount of CNTs on CFs. Based on the result, it can be found that 2.5 wt% of CNT have been grafted on the CFs. However, GNPs have a decomposition temperature similar to CNTs, it is not possible to evaluate the CNT fraction on GNPs with this method.

Secondly, the oxidation process has been conducted for both the CNT-CFs and the GNPs. For oxidized CNT-CFs, the XPS results show that the oxygen fraction increases by 1 % compared to CNT-CFs, indicating the introduction of oxygen-containing groups on the hybrids surface. For the GNPs, two kinds of methods have been used, surface oxidation in air condition and complete oxidation by the Hummers method. TGA, XPS and morphology characterization reveal the difference between them.

References

1. Sengupta, R., et al., *A review on the mechanical and electrical properties of graphite and modified graphite reinforced polymer composites*. Progress in Polymer Science, 2011. **36**(5): p. 638-670.
2. Im, H. and J. Kim, *Thermal conductivity of a graphene oxide–carbon nanotube hybrid/epoxy composite*. Carbon, 2012. **50**(15): p. 5429-5440.
3. Bai, J., *Procede de synthese de nanotubes de carbone sur materiaux micrometriques longs et particuliers*. 2010, Google Patents.
4. Zhao, H. and J. Bai, *Highly Sensitive Piezo-Resistive Graphite Nanoplatelet–Carbon Nanotube Hybrids/Polydimethylsilicone Composites with Improved Conductive Network Construction*. ACS Applied Materials & Interfaces, 2015. **7**(18): p. 9652-9659.
5. Liu, Y., et al., *Synthesis, characterization and cytotoxicity of phosphorylcholine oligomer grafted graphene oxide*. Carbon, 2014. **71**: p. 166-175.
6. Zhang, J., *Different surface treatments of carbon fibers and their influence on the interfacial properties of carbon fiber/epoxy composites*. 2012.
7. Zielke, U., K. Hüttinger, and W. Hoffman, *Surface-oxidized carbon fibers: I. Surface structure and chemistry*. Carbon, 1996. **34**(8): p. 983-998.
8. Stankovich, S., et al., *Synthesis and exfoliation of isocyanate-treated graphene oxide nanoplatelets*. Carbon, 2006. **44**(15): p. 3342-3347.
9. Marcano, D.C., et al., *Improved Synthesis of Graphene Oxide*. ACS Nano, 2010. **4**(8): p. 4806-4814.
10. Ferrari, A.C., et al., *Raman spectrum of graphene and graphene layers*. Physical review letters, 2006. **97**(18): p. 187401.

Chapter 3 Comparison of different surface treatments of carbon fibers used as reinforcements in epoxy composites: Interfacial strength measurements by in-situ scanning electron microscope tensile tests

Introduction

In chapter 2, I have successfully treated the CF surfaces by different methods and obtained four kinds of CFs with different surface states: Raw CFs, Desized CFs, carbon nanotube grafted CFs (CNT-CFs) and oxidized CNT-CFs. I want now to address this question: How do these treatments affect the intrinsic properties of CFs and the final performance of the composites?

In this chapter, I first study the intrinsic properties of the four kinds of CFs by a single fiber tensile test. The modulus, strength, and ultimate elongation are compared. Secondly, the interfacial shear strength (IFSS) of the CF-epoxy composites is studied by a single fiber fragmentation test. Thirdly, to evaluate the interfacial strength in different states of surface modification, I develop an *in-situ* measurement method by using a SEM and a nano-manipulator to apply a tensile micro-load. This experiment allows both an observation of the fracture behavior of the interface and a measurement of its interfacial strength. Then, this method is applied on graphene-based composites to observe the fracture behavior on a micrometer scale. Fourthly, an elemental analysis is carried out in a scanning transmission electron microscopy (STEM) by combining an energy dispersive X-ray (EDX) spectrum mapping which offers some insight into the efficiency of the surface modification of the CFs.

3.1 Experiment and characterization

3.1.1 Preparation of CNT-CF/epoxy composites

A 1080S epoxy resin -- accompanied with the curing agent 1084 with a mass ratio of 1/3 - was used. The resin and curing agent were mixed homogeneously and then a small bundle of CF fabric was slowly put into the epoxy matrix for a thorough immersion. Afterwards, the mixture was degassed for 60 min inside a vacuum oven at room temperature. The curing process was conducted at 60 °C for 15 hours. At last, the post-curing process was conducted at 100 °C for 1.5 h. The as-prepared composites were cut into small cuboids for further microstructure characterizations.

3.1.2 Tensile tests of pure epoxy

The mechanical properties of the pure epoxy were determined by tensile testing. Bone-shaped specimens were manufactured using an open face steel molds. The specimen length was 50 cm. The length, width, and thickness of the gauge section of the specimen were 33, 6, and 3.2 cm, respectively. The geometry and dimensions of the tensile test specimen comply with an ASTM D638. The specimens were tested in an Instron 5544 machine equipped with a 2 kN load cell. The specimens were loaded at a rate of 2 mm/min. Five specimens were tested.

3.1.3 Single fiber test

The single CF tensile test and single CF fragmentation test were carried out using the Instron 5544 instrument with a load cell of 5 N and 2 kN, respectively. The single CF tensile test was conducted according to NF ISO 11566. The cross-head speed used was 0.5 mm/min, and the gauge length was around 25 mm. The single fiber fragmentation test was carried out with dog-bone shape samples of 0.2 mm in thickness and 10 mm in gauge length. Each individual CF or CNT-CF was embedded in the middle of the composite specimen. The cross-head displacement was 0.1mm/min. After fiber break saturation, the number of breaks was obtained using an optical microscope (Leica Aristomet DC300).

3.1.4 Tensile and TEM samples preparation by FIB

CF/Epoxy composites used for the FIB-SEM was previously polished by the sand papers with different particle sizes to obtain an ultra-smooth surface. To decrease the damage on the CF-epoxy interface, the polishing procedure was conducted in one direction at very low speed.

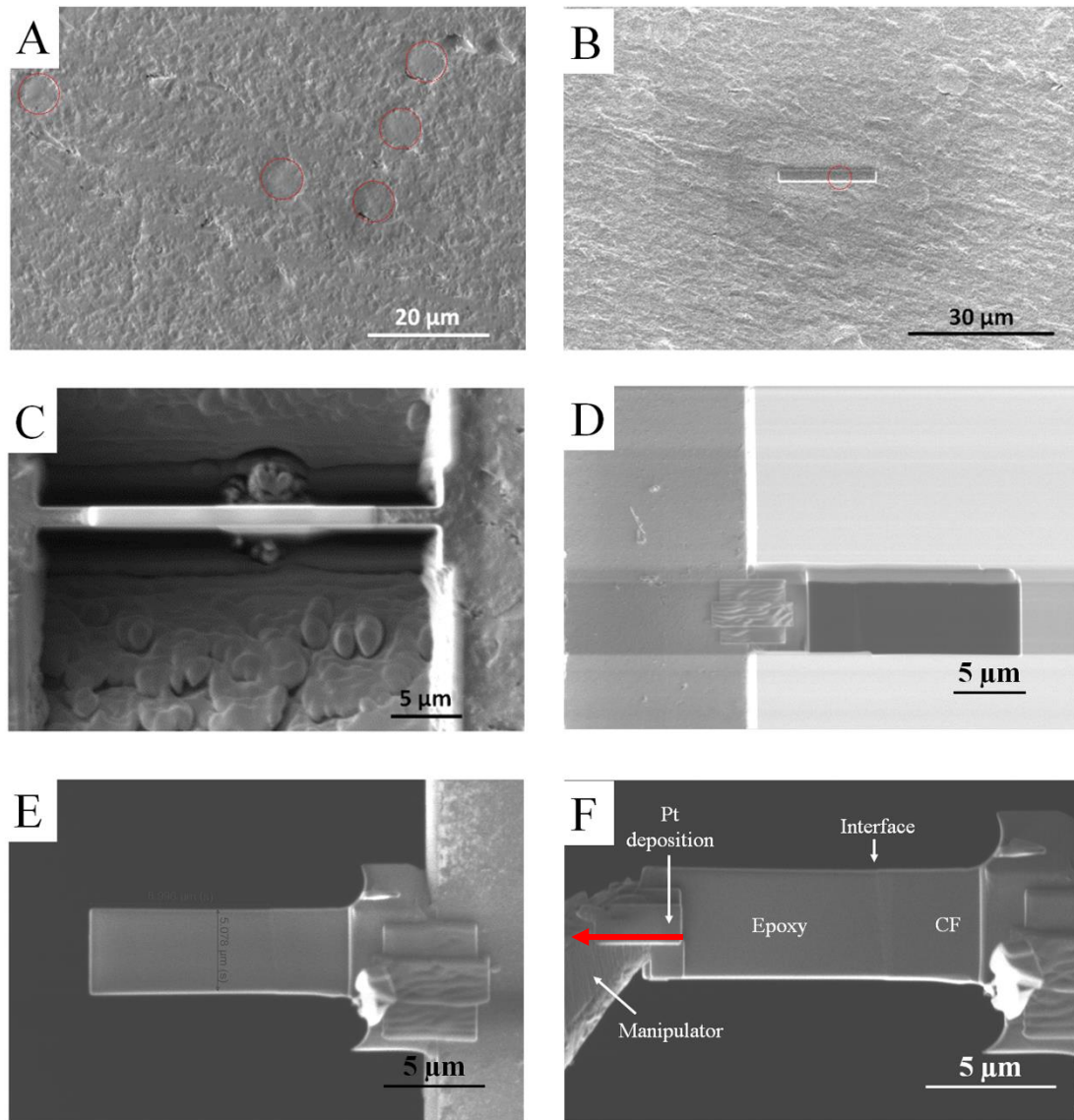


Figure 3.1 The preparation of the sample for micro-tensile test: (A) The polished surface containing several CFs which are marked out by red circles; (B) A Pt protection is deposited on the CF/epoxy interface with a dimension of $20\mu\text{m}\times 2\mu\text{m}\times 1\mu\text{m}$, and the red circle indicates the position of the targeted CF; (C) The tensile sample is milled down to a thickness of $1\mu\text{m}$, with a width of $8\mu\text{m}$; (D) the lamella is lifted out by the manipulator and soldered to the copper grid edge by Pt deposition; (E) Two quarter-circles are conducted on the interface to avoid the stress concentration; (F) The manipulator is welded to the lamella by depositing a Pt layer, the red arrow indicates the loading direction.

The FIB sample preparation was performed in the same Helios 660 (FEI) as described in chapter 4. The sample preparation procedures are shown in **Figure 3.1**. First, a cross-section with vertically aligned CFs was selected (**Figure 3.1A**) and the platinum (Pt) protective layer with a thickness of $1.0\mu\text{m}$ was deposited on the surface of the target milling area (**Figure 3.1B**).

A 21 nA and then a 2.5 nA beam current were applied to obtain a lamella with a thickness of $\approx 1.5 \mu\text{m}$ (**Figure 3.1C**). Afterwards, the section was detached from the surrounding material and transferred to a TEM half-grid before the fine thinning (**Figure 3.1D**). The fine thinning was carried out only at the areas of interest to remove the surface deposited materials. To avoid stress concentration during the tensile test, two quarter-circles were made in the CF region (**Figure 3.1E**). Finally, the micro-manipulator was soldered to the sample by depositing a Pt layer. To avoid a point force load on the sample, the deposited Pt covered the whole width of the sample (**Figure 3.1F**). The width and the thickness of the samples were $5.0 \mu\text{m}$ and $1.5 \mu\text{m}$, respectively and the epoxy part had a length ranging from $6.5 \mu\text{m}$ to $7.0 \mu\text{m}$.

Once the manipulator was strongly soldered to the tensile sample by Pt deposition, the magnification of the electron beam images and ion beam images were set properly, at $6500\times$. The current of the ion beam was set to 80 pA to decrease the damage to the tensile sample. A stepwise displacement of 200 nm was applied to the manipulator. Both electron beam and ion beam images were acquired to measure the global deformation during each tensile step.

Following the same procedure, several experiments were carried out on each type of sample: eight for raw CF/epoxy, five for desized CF/epoxy, five for CNT-CF/epoxy, and seven for oxidized CNT-CF/epoxy, respectively.

3.1.5 Characterization

The SEM and TEM characterization were conducted in the same condition as we described in chapter 2. Energy-dispersive X-ray spectroscopy (EDX) was carried out on the same equipment and operated in scanning transmission electron microscope (STEM) mode. All the images were acquired with a high-angle annular dark-field (HAADF) detector. The EDX mapping was acquired for 10 min.

3.2 Results and discussion

3.2.1 Basic characterization of different types of CFs

Table 3.1 Elongation and tensile strength at break and Young's modulus of single fiber tests for four types of CFs. 30 samples were measured for each kind of fiber. Evaluation of the interfacial shear strength (IFSS) of different CFs in the composites.

	Raw	Desized CF	CNT-CFs	CNT-CFs Oxidized
Strength (MPa)	4252.6 ± 1356.8	3269.9 ± 976.7	5375.1 ± 1287.7	4218.4 ± 1191.5

Modulus (GPa)	195.3±33.6	207.1±25.5	230.8±16.5	201.6±15.5
Elongation (%)	2.2±0.6	1.6±0.5	3.1±0.5	2.1±0.6
Critical length (mm)	0.456	0.778	0.53	0.42
Shape Parameter	3.47	3.72	4.51	3.98
IFSS (MPa)	93	34	76	90

The evaluation of interfacial properties is important to better understand the previously mentioned mechanical reinforcing effects in the CF/epoxy composites.

In the first place, the single tensile test was conducted to study the influence of the CVD procedure and of the CNT grafting on the mechanical properties of CFs. The average fiber elongation and tensile strength at breaking point along with Young's modulus results are summarized in the **Table 3.1**. It can be found that both the strength at break and Young's modulus of CNT-CFs are higher than those of the as-received CF, reaching 5375.1 MPa and 230.8 GPa, respectively (compared to 4252.6 MPa and 195.3 GPa for the as-received CF). After further oxidization, the strength and Young's modulus of CNT-CFs return to the same level as raw CF. However, the simple removal of the sizing layer can largely decrease the strength of CFs.

The above results demonstrate that no degradation of the mechanical properties of CFs has been generated in the CVD process used for the CNT growth. Moreover, the CF mechanical properties could be further improved when the optimized CVD conditions and CNT arrangement are used.

3.2.2 Interfacial shear strength (IFSS)

The interfacial shear strength (IFSS) between CFs and the epoxy matrix is investigated via single fiber fragmentation tests [1]. The IFSS is estimated from the Kelly-Tyson model [2]. The obtained results are summarized in **Table 3.1**. The average critical fragment length of raw CFs is shortest in all four types of CF/epoxy, indicating a best interfacial bonding strength with CFs. The estimated IFSS of raw CF/epoxy is around 93 MPa. It was mentioned previously that as-received CFs contain a sizing layer that protects them from manipulation deterioration and improves their interfacial bonding with the polymer matrix in the composites. After being heated at 650°C to remove the sizing layer, the IFSS of desized CF/epoxy is greatly decreased to 34 MPa, becoming one third of the strength as compared with raw CF/epoxy. The growth of CNTs was conducted above 600°C, and the sizing layer was removed due to heat

decomposition. It can be found that the fiber fragment length increased after the CNT growth, as compared to that of raw CF/epoxy, which demonstrate a lower IFSS (76 MPa). After surface oxidation of CNT-CFs, the IFSS of oxidized CNT-CFs/epoxy is increased to 90 MPa, almost reaching the same level as raw CF/epoxy.

3.2.3 *In-situ* interfacial strength measurement

To evaluate the axial interfacial strength between CFs and the epoxy matrix, an *in-situ* method has been developed in a SEM column. There are several advantages of testing fibers using *in-situ* SEM and a significant one among them is a precise measurement of the strain along the entire gauge length. Besides, the stretching process can be clearly observed along with the fracture behavior.

Considering the typical tensile specimen in **Figure 3.2**, it has enlarged ends or shoulders for gripping. The important part of the specimen is the reduced gage section. The cross-sectional area of the gage section is reduced relative to that of the remainder of the specimen so that deformation and failure will be localized in this region. Another important area is the connection region between the gage section and the shoulders, which should be great enough so that the stress concentration do not affect the gage section. Usually, we use the R/W ratio to evaluate the stress concentration degree. In the traditional tensile test, this ratio is larger than 2 to avoid the stress concentration.

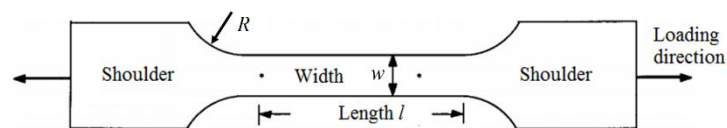


Figure 3.2 Typical tensile specimen, showing a reduced gage section and enlarged shoulders.

3.2.4 Simulation

A finite element (FE) model of composites is developed to evaluate the stress concentration in the structure. In this model, I consider that the tensile load remained in the elastic region, and the detailed physical properties of the epoxy and CFs are shown in **Table 3.2**. Using the commercial software ABAQUS 6.11, an 8 nodes three-dimensional linear brick element is used for the matrix modeling.

Table 3.2 The physical properties of CFs and epoxy used for simulation.

	Young's modulus (GPa)	Poisson's ratio	Density (g/cm ³)
CFs	195	0.2	1.60
Epoxy	3.5	0.38	1.13

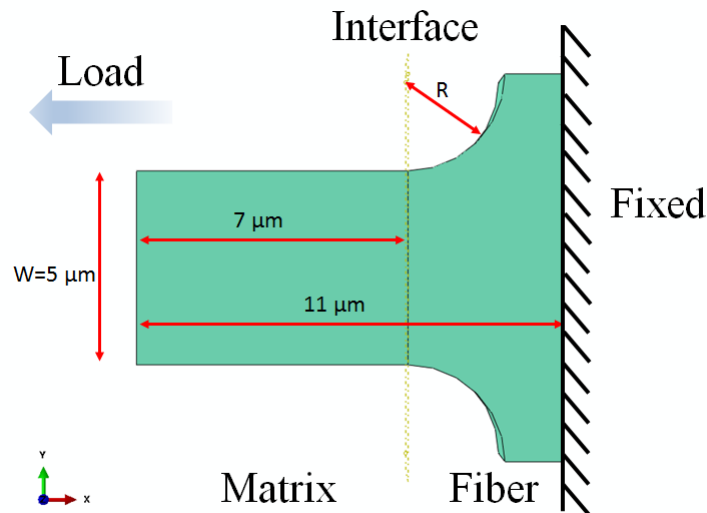
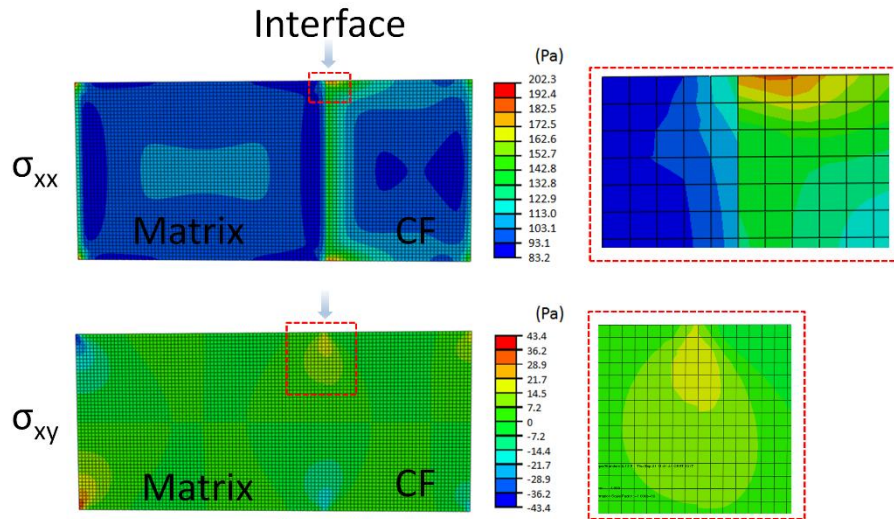
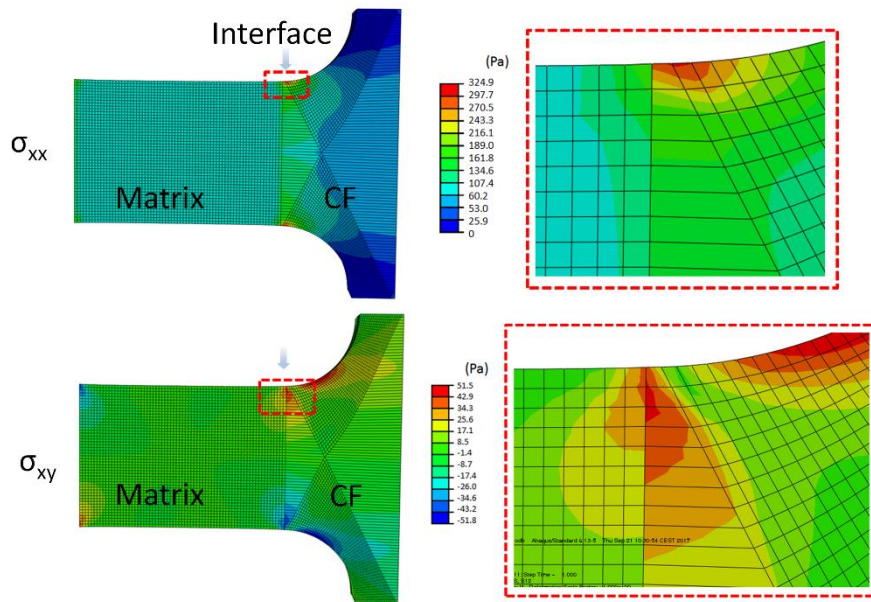


Figure 3.3 A schematic illustration of a representative tensile sample for the fiber and epoxy matrix.

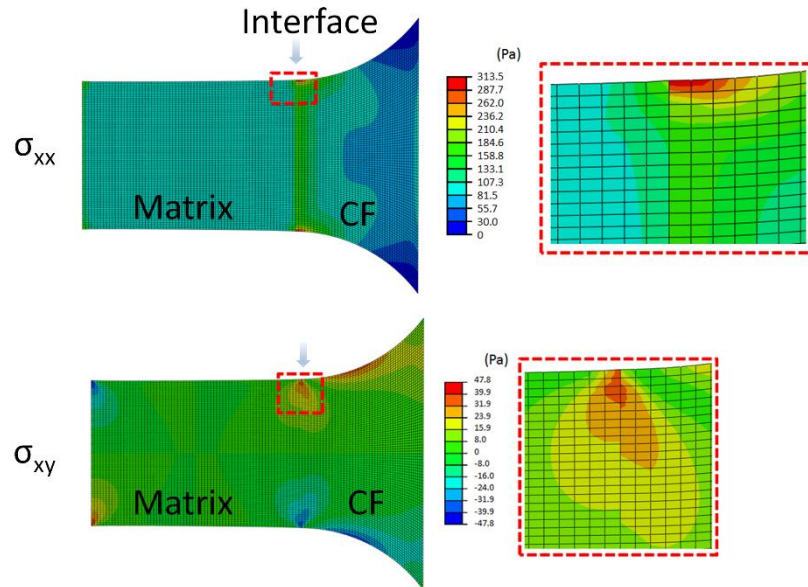
The bond-shaped specimen is selected and the perfect bonding at the interface is assumed in this study. A schematic illustration of a representative tensile sample for the fiber and epoxy matrix is shown in **Figure 3.3**. In the model, the epoxy matrix with a cuboid-shape is in the left side of the sample, which has a dimension of $7 \mu\text{m} \times 5 \mu\text{m} \times 1 \mu\text{m}$. The neck region is in the CF part. To optimize the design of the tensile structure, four R/W ratio, 0.5, 1, 2 and ∞ (rectangular shape), are compared. The right side is clamped and a load of 100 Pa is added in the -X direction. The structural shear (σ_{xy}) and tensile stress (σ_{xx}) distribution along the sample are shown in **Figure 3.4**.



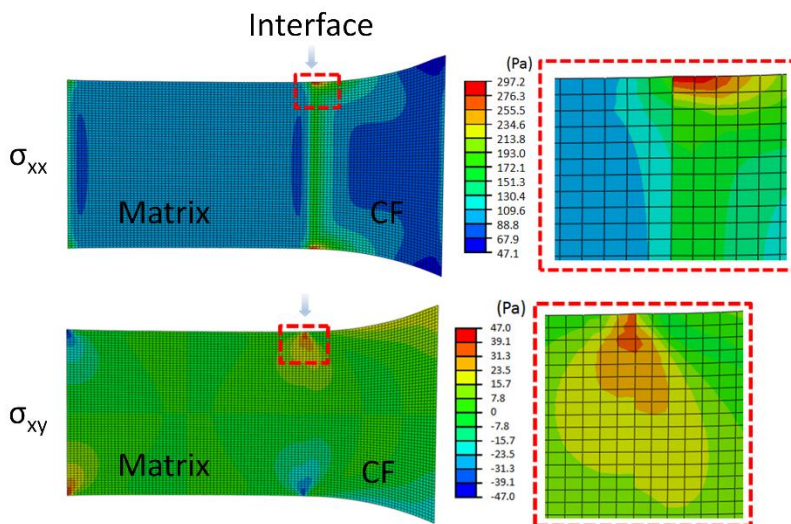
(A) $R/W = \infty$



(B) $R/W = 0.5$



(C) R/W=1.0



(D) R/W=2.0

Figure 3.4 Calculated shear (σ_{xy}) and tensile stress (σ_{xx}) distribution along the samples with different R/W ratio: (A) R/W= ∞ ; (B) R/W=0.5; (C) R/W=1.0; (D) R/W=2.0. (The red rectangular in each sample shows the enlarged stress distribution image.)

Given that sufficiently accurate estimation of the stress distribution in the interface of CF/epoxy composite is essential in this study. According to the FE results shown in **Figure 3.4**, in four different structure, the maximum stress is found at each edge of the interface, both for shear and tensile stress. Among the four structures, the stress concentration is the weakest in

$R/W=\infty$ (the rectangular shape), in which the tensile stress is almost homogeneously along the interface. Hence, the rectangular shape is selected as the structure for the *in-situ* tensile test.

3.2.5 Experiment by FIB-SEM

A specimen in micrometer-scale has been designed as shown in **Figure 3.5(A)**. It keeps a half shape of traditional tensile specimen, with a gage section formed by the epoxy matrix and a shoulder section formed by the CF. To get rid of the stress concentration caused by the neck region, the interface moves far enough from it. The final specimen prepared by FIB is shown in **Figure 3.5(B)**. Theoretically, the stress transferred homogeneously in the cross-section all along the tensile specimen, the stress acting on the epoxy matrix equals the stress at the interface. Hence, the interfacial strength at the interface can be obtained by measuring the stress loading on the epoxy matrix part. Here are the details: (1) the original length (l_0) of epoxy matrix can be precisely measured on the SEM image from the interface to the edge of Pt deposition. (2) the tensile force is loaded by shifting the manipulator discontinuously with the smallest step (200 nm) until the failure is reached. (3) the images are acquired after each shifting step to monitor length change in epoxy matrix.

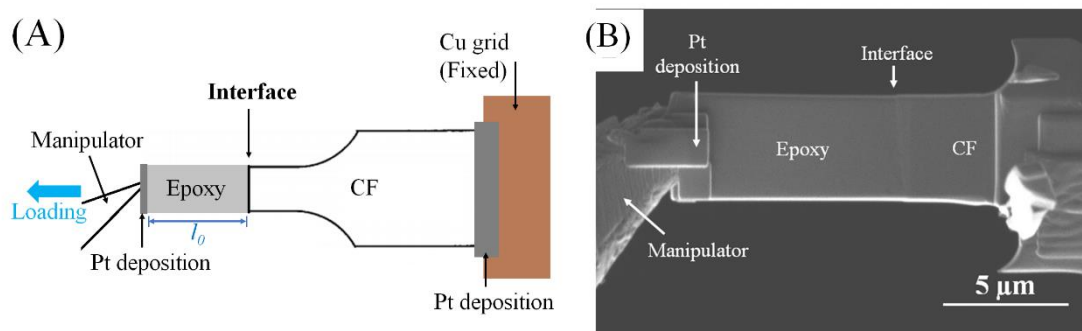


Figure 3.5 (A) The sketch of a tensile specimen to measure the interfacial strength between the CF and epoxy matrix; (B) SEM image of final tensile specimen prepared by FIB-SEM.

Figure 3.6 provides three typical fracture positions during the tensile test with the rectangular shape. The ideal situation is shown in **Figure 3.6(A)**, in which the fracture happens in the interface. By measuring the deformation on the matrix part, the interfacial stress could be estimated precisely. **Figure 3.6(B)** shows a strong interaction in the interface, in which the fracture happens in the epoxy matrix. In this situation, the interfacial stress exceeds the fracture stress of epoxy matrix. **Figure 3.6(C)** shows a failure tensile test due to the debonding of the manipulator. Usually, the epoxy matrix breaks in the plastic region. Hence, if the failure

happens in the Pt deposition part, the specimen cannot be re-soldered since the second tensile in the failure sample could not reflect the real interfacial stress based on the strain.

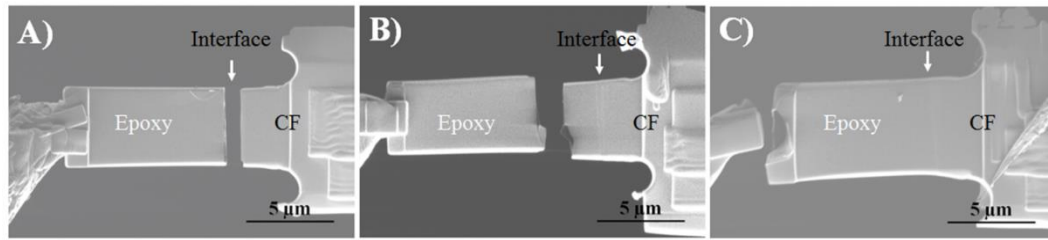


Figure 3.6 Fracture position during the tensile test: (A) at the interface, (B) in the epoxy matrix and (C) at the connection point.

Figure 3.7(A) presents SEM images where an increasing tensile displacement is applied to an interface until the failure is reached. The green arrows on the top indicate the tensile direction, and the CF/epoxy interface is pointed out by a green line. It is obvious that the CF part is thicker than the matrix, which is caused by the milling process: Since CFs are much harder than polymers, the CF cannot achieve the same thickness as the matrix with the same milling conditions. However, it is found that the interface position remains at the same position during the stretching process, which indicates the traverse strain of the CF can be negligible compared with the polymer domain due to its much higher modulus.

As a method of evaluation and confirmation of the tensile displacement, ion beam images were also acquired during testing along with electron images, as shown in **Figure 3.7(B)**. For each tensile stepwise, the error in displacement can be effectively reduced by measuring and comparing the two series of images. **Figure 3.7(D)** shows the sample position: the angle between the electron beam and the sample is 38° and the angle between the ion beam and the sample is 90° . The stretching direction is perpendicular to the plane generated by the two beam sources.

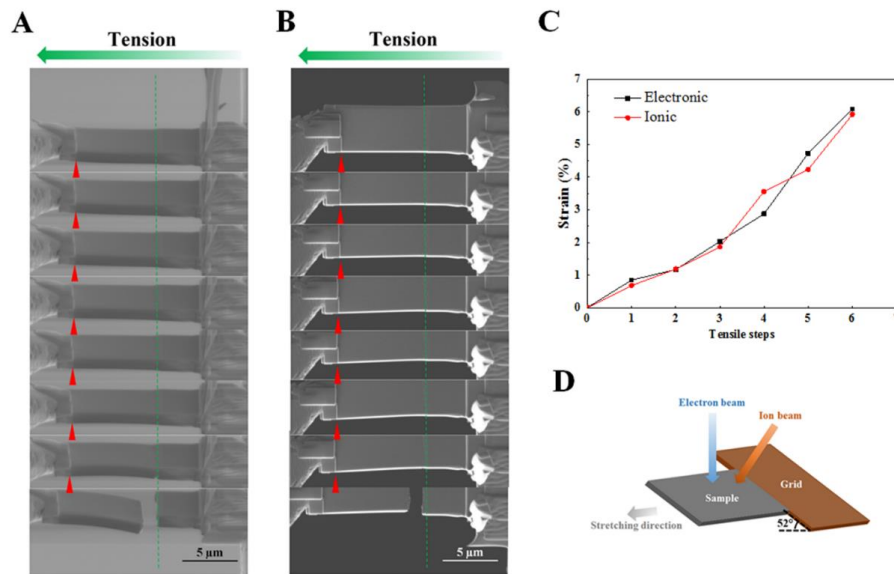


Figure 3.7 Stretching process of a raw CF/epoxy composite sample observed by SEM with two series (A) Electron and (B) Ion images; (C) Strain-step curves during the stretching process, data extracted from two series of images; (D) Sketch of the global sample position, with regard to the stretching direction and the two beam sources.

The apparent strain is defined by the change in the length of the segment between the interface and the deposited Pt. As shown in **Figure 3.7(C)**, the curves about the strain-stretching steps in the two series of images are extracted. During the stretching process, the manipulator moves by steps of 200 nm. However, in the first stage, the strain is not increased due to the tiny bending existing in the manipulator. The two curves are almost overlapped with little difference. Hence, the strain measurement can be conducted with either type of image which exhibit a clear CF/epoxy interface.

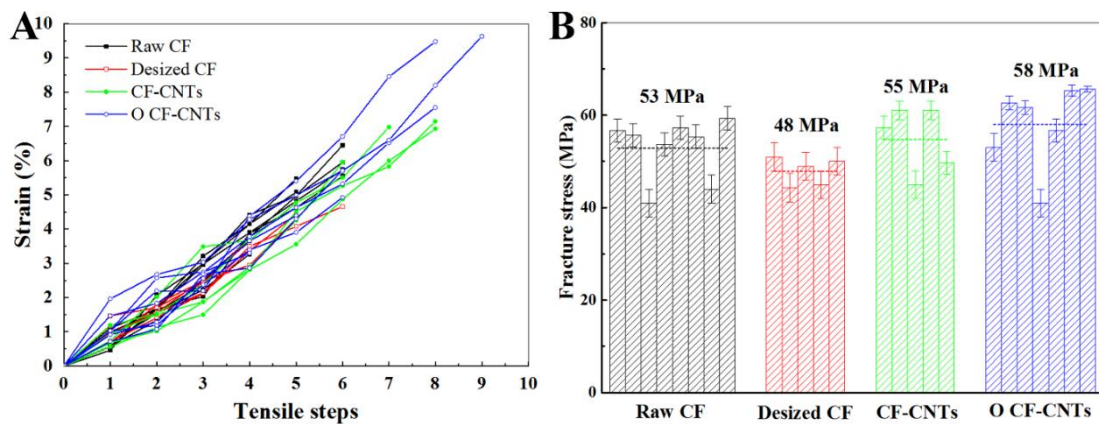


Figure 3.8 (A) Displacement-tensile step plot of stretching samples extracted from ionic images. The black, red, green and blue lines are the results from the raw CF/epoxy, desized

CF/epoxy, CNT-CFs/epoxy and oxidized CNT-CFs/epoxy, respectively. (B) Fracture strengths of the raw CF/epoxy, desized CF/epoxy, CNT-CF/epoxy and oxidized CNT-CF/epoxy.

The displacement is measured by either ionic or electron images acquired during each tensile step, as shown in **Figure 3.8(A)**. The strain of all the curves increases linearly during the stretching. The curves have a similar slope since the major strain is localized on the epoxy part with almost the same geometry. The small discrepancy in the curves is due to the blurry boundary in some images (the green lines in **Figure 3.8(A)** and **(B)**). According to the measured results, the failure step happens between steps four and nine. The fracture of raw CF/epoxy interface mostly happens in step six, leading to an average strain of 5.14 %. The desized CF/epoxy tend to break at a lower step, mostly at the fourth and fifth step, leading to an average strain of about 4.15 %. After grafting CNTs, the interaction between CNT-CFs and epoxy recover and the fracture mostly happens in sixth, leading to an average strain of 5.59 %. By oxidation treatment, the interaction between oxidized CNT-CFs and epoxy matrix further increases. The breaking point tends to happen at a higher step. Even for two samples of oxidized CNT-CFs/epoxy composite, the fracture happens at the connection point or in the epoxy matrix, rather than at the interface, which indicates that the interfacial strength between oxidized CNT-CFs and epoxy is larger than the fracture strength of epoxy matrix.

Since the stress-strain values of pure epoxy can be easily acquired by tensile test (as shown in **Figure 3.9**, the interfacial strength between CFs and epoxy can be estimated by fitting the corresponding strain in the stress-strain curves, as shown in **Figure 3.8(B)**. The fracture strength of epoxy is 66.5MPa. The average strain of oxidized CNT-CFs/epoxy is 6.82 % before failure, corresponding to 58 MPa in the stress-strain curves. However, since several samples broke in the matrix part, the actual interfacial strength of oxidized CNT-CFs/epoxy is possibly larger than 58 MPa. By using the same method, the interfacial strength of raw CF/epoxy, CNT-CF/epoxy and desized CF/epoxy are 53, 55 and 48 MPa, respectively. These values are close to the values reported by other groups [3].

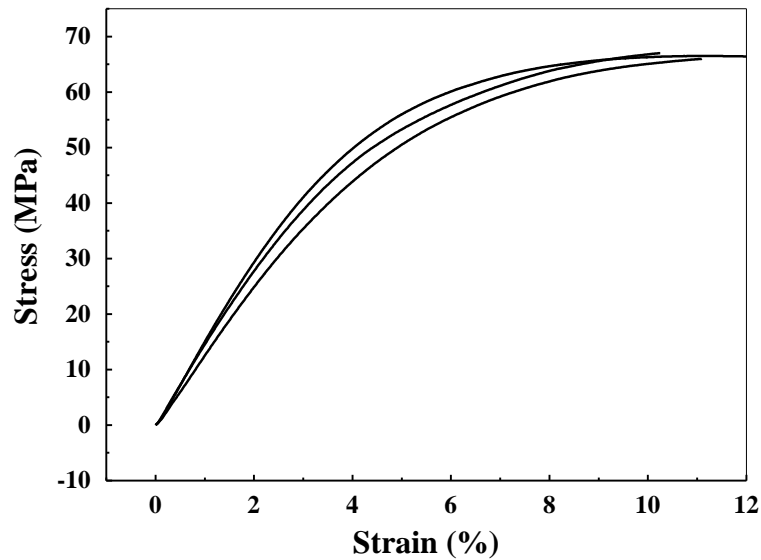


Figure 3.9 Stress-strain values of pure epoxy matrix by tensile test.

3.2.6 *In-situ* tensile test for GNP/epoxy composite

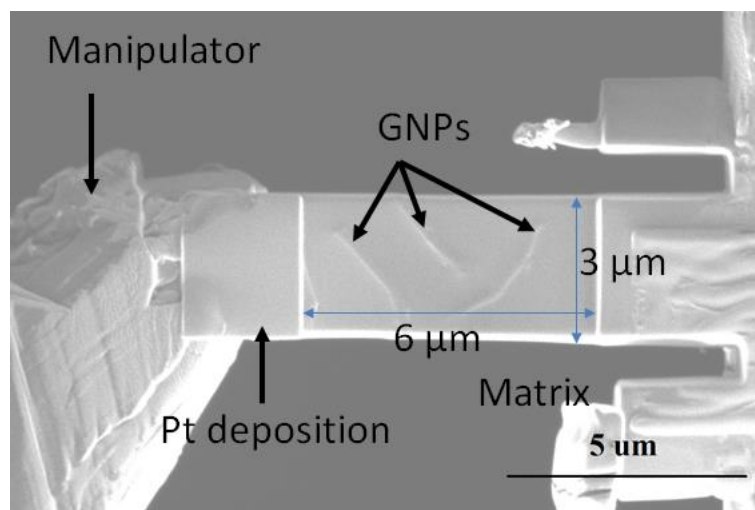


Figure 3.10 Detailed size value of a GNP/epoxy tensile sample.

Since the *in-situ* tensile test has successfully measured the interfacial strength between CFs and the polymer matrix, we are wondering if this method could be used in other systems, for example, the GNP/epoxy composite. Hence, in this section, the same process is conducted on the GNP/epoxy composite. The size value is shown in detail in **Figure 3.10**. A composite sample with dimensions of $6\ \mu\text{m} \times 3\ \mu\text{m} \times 1\ \mu\text{m}$ is prepared by FIB. One side is attached on the copper grid and another side is soldered with the manipulator. Since the GNP is more rigid than the epoxy matrix, after exposition to the ion beam at low current for several seconds, the profile of the GNP appears in the matrix, as we pointed out by arrows.

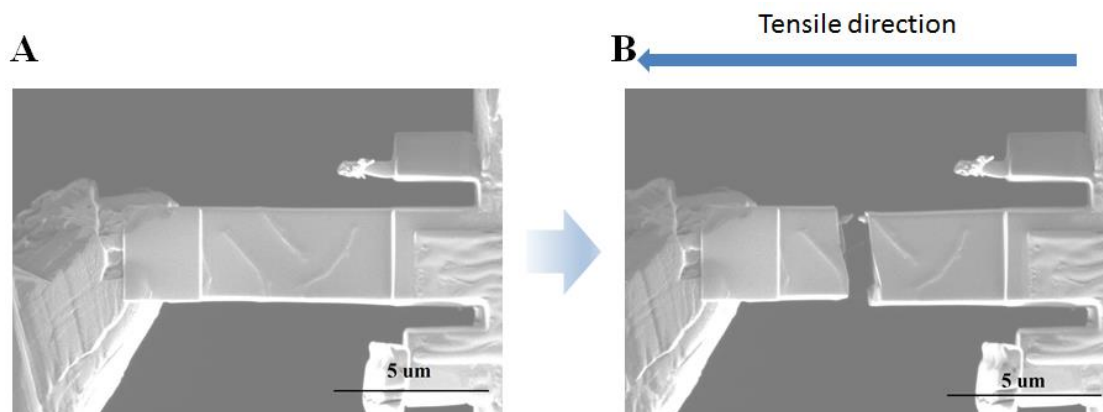


Figure 3.11 (A) Sample without stretching; (B) after failure.

The ideal conditions for the measurement of the GNP/epoxy interfacial strength need to satisfy three conditions:

- (1) the GNP is perpendicular to the tensile direction;
- (2) the failure happens at the GNP/epoxy interface;
- (3) there are no bubbles in the matrix.

However, in this sample, we only achieve the third ideal condition. The sample before and after stretching is shown in **Figure 3.11**. Three pieces of GNPs are not vertical to the tensile direction. Hence, it is not suitable to measure the interfacial strength. However, the fracture behavior can be directly observed during the stretching. The tensile direction follows the $-x$ axis. After several steps of stretching, the sample breaks in the central part, but not along the GNP/epoxy interface. **In Figure 3.11B**, a small piece of GNP can be seen on the fracture surface, which indicates the unmodified GNP which has a weak interaction with the epoxy matrix. Furthermore, for original GNPs, it tends to aggregate. Hence, the fracture can happen in between the interlayer.

3.2.7 STEM/EDX characterization of interface/interphase

To understand the function of the CNT layer on the CF surface, STEM combined with EDX are employed to study the CF/epoxy composite interface. It is suitable for acquiring high-resolution images with a detailed elemental information and quantitative analysis on the interphase composition. It has been successfully adopted in various fields. Four TEM lamellae were prepared by FIB, as shown in **Figure 3.12**. The CF orientation is parallel to the lamella

plane. In four images, the dark part corresponds to the CF thicker than the epoxy domain as explained in section 3.2.2.

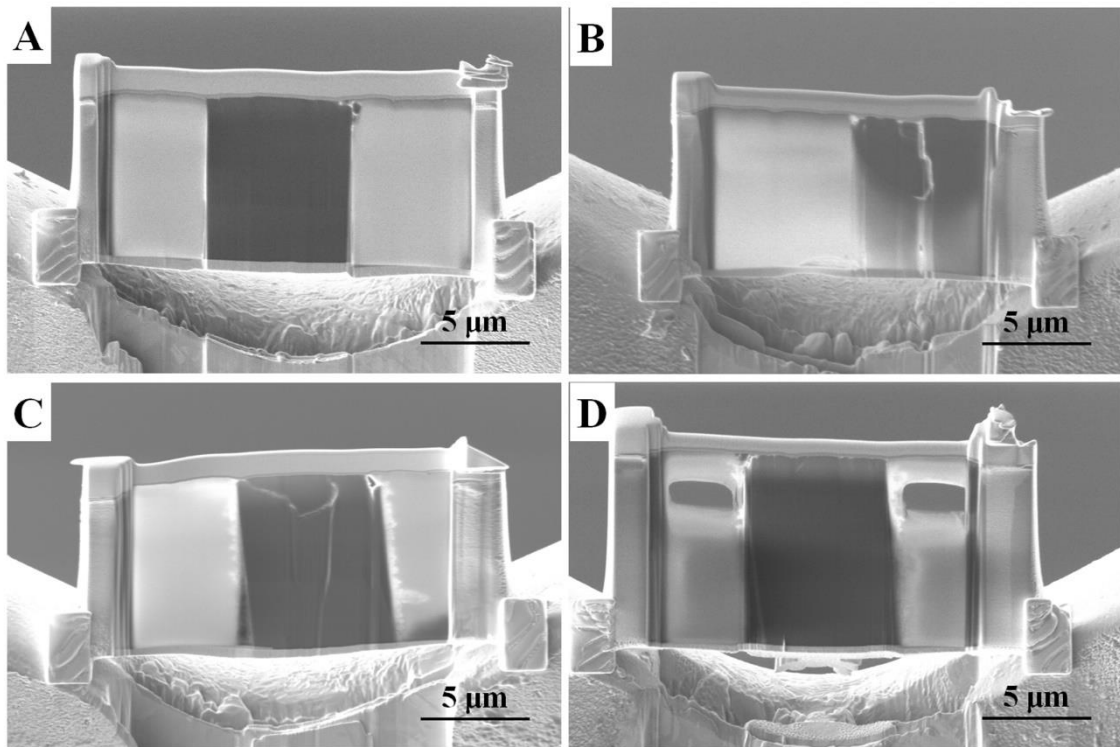


Figure 3.12 TEM lamellae prepared by FIB (A) raw CNT-CFs/epoxy, (B) desized CNT-CFs/epoxy, (C) CNT-CFs/epoxy and (D) oxidized CNT-CFs/epoxy.

Since the CF, CNTs and epoxy resin are all carbon-based materials, the contrast is weak in bright field². It is preferable to use the HAADF detector in STEM mode, which is known as Z-contrast configuration. It has two major advantages: one is that small differences in the average atomic number or thickness of the material can be observed with a higher contrast difference in the dark field image; the other is that the region of interest can be scanned with a very small probe (#0,1 nm in diameter) which helps to acquire high resolution EDX mapping. **Figure 3.13** shows two STEM HAADF images of raw CF/epoxy and CNT-CF/epoxy, respectively. For the raw CF/epoxy (**Figure 3.13A**), the bright region corresponds to the CF part with a larger thickness than the epoxy part while the dark part is the pure epoxy. The interface in between is the obvious boundary. CNT-CF/epoxy is presented in **Figure 3.13B**. A tubular structure can be clearly observed by STEM under high resolution. After grafting CNTs

² The beam of electrons passes directly through an aperture before reaching the specimen. The image results from a weakening of the direct beam by its interaction with the sample.

on a CF surface, the epoxy matrix can immerse the CNT layer and wet the CF surface completely without creating voids in the interface region. The CNTs are dispersed in the matrix homogeneously. The average thickness of the CNT layer is around 440 nm. The bright spots in the matrix domain should be the catalyst used for the CNT growth.

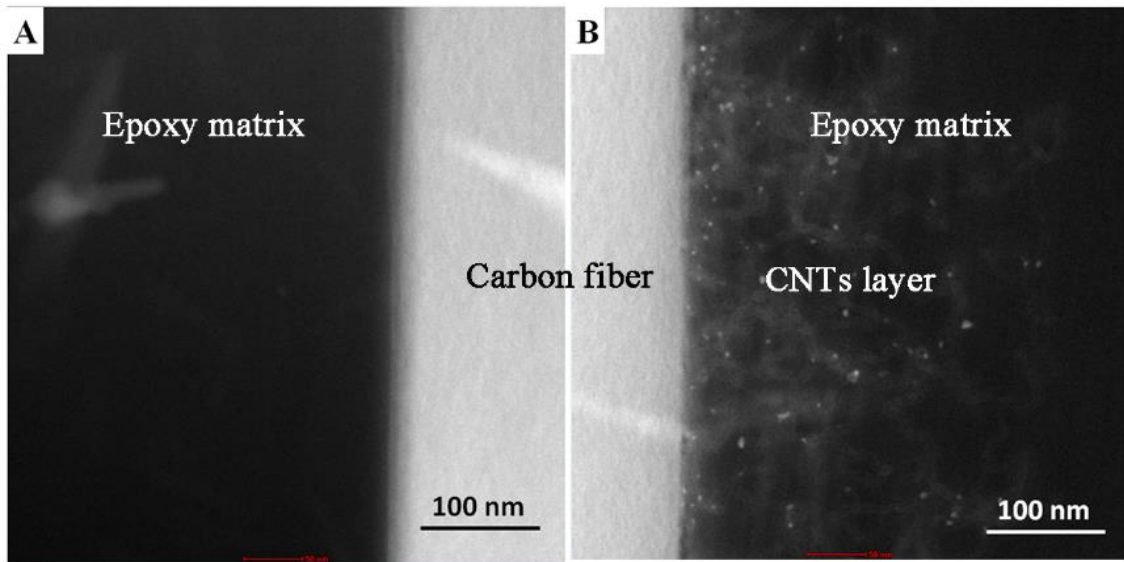


Figure 3.13 STEM Z-contrast (HAADF) image showing the interface region of the CF and epoxy: (A) raw CF/epoxy and (B) CNT-CF/epoxy interfaces.

Figure 3.14(A) presents a STEM image of raw CF/epoxy interface. The green rectangle corresponds to the region selected for EDX analysis where three elements -- oxygen, carbon and chlorine -- were investigated. Chlorine exists in the sizing layer but has migrated to the epoxy domain and has aggregated at the interface. For oxygen, there also exists an aggregation at the interface, indicating that the oxygen-containing groups have a higher density than in the epoxy matrix. For carbon, the aggregation in the CF domain is obvious.

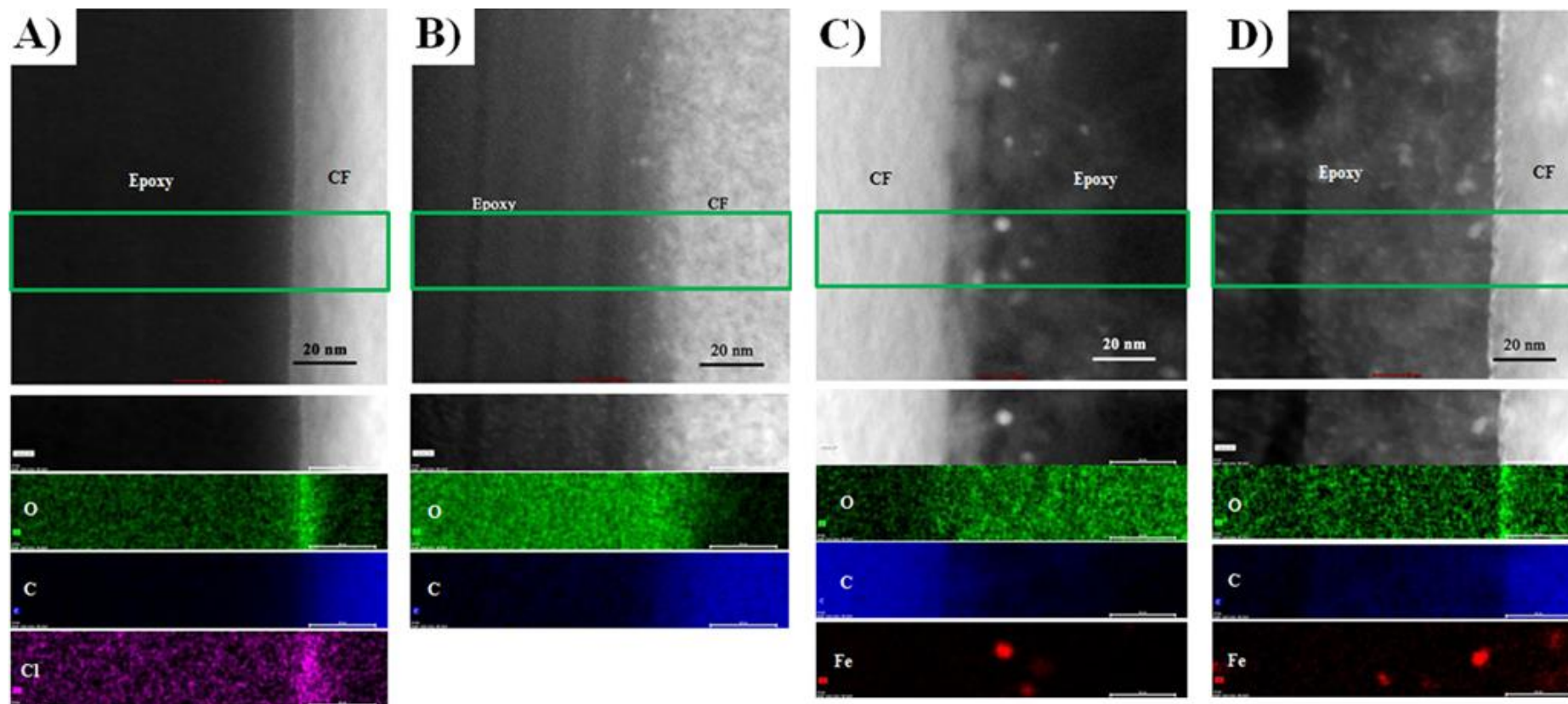


Figure 3.14 High magnification STEM Z-contrast (HAADF) image showing a CF perpendicular to the epoxy foil prepared by FIB: Interfaces of (A) Raw CF/epoxy, (B) Desized CF/epoxy, (C) CNT-CF/epoxy and (D) Modified CNT-CF/epoxy, respectively. The regions marked out by the green rectangle were analyzed by EDX, the elements were marked out by different colors, green for oxygen, blue for carbon, pink for chlorine and red for iron, respectively.

Figure 3.14(B) shows a STEM image of desized CF/epoxy interface. After the removal of the sizing layer, there is no aggregation in the interface part. From the CF to the epoxy domains, the element presence changes gradually both for carbon and oxygen. Compared with raw CF/epoxy composite, the interface is more blurred in desized CF/epoxy.

Figure 3.14 (C) and (D) correspond to the observation of CNT-CF/epoxy and modified CNT-CF/epoxy composites, respectively. The CNT layers are distributed homogeneously on the CF surfaces. The bright spots near the interface correspond to the heavier iron catalyst particles, which is confirmed by EDX. The CNT layer morphology can be figured out in the epoxy matrix. In the case of the CNT-CF/epoxy interface, the elements also change gradually. However, in the modified CNT-CF/epoxy interface, I find there an oxygen aggregation. As far as carbon is concerned, there is no element aggregation layer.

Grafting a layer of CNTs on the surface of CFs is a common method to modify the interaction between the polymer matrix and CFs. The effect of reinforcement is obvious since the CNT layer can greatly increase the contact area at the interface. Moreover, the CNTs, with their perpendicular arrangement, can insert in the matrix part and further increase the interfacial strength. The CNT layer can also increase the conductivity of the entire composites.

After removing the sizing layer, the interaction between the CFs and the epoxy matrix is greatly weakened due to the decrease of chemical bonds. After grafting CNTs on the surface, the increased interfacial strength is obvious compared to the case of desized CF/epoxy composites, since CNTs can largely increase the contact area between matrix and CF. Furthermore, the CNT layer, with its mechanical properties, could enhance the surrounded matrix. The oxidized CNT-CF/epoxy composite presents the best interfacial strength of the four composites. The oxidized CNT-CFs are fabricated by heating the sample at 400 °C for 4 min to increase the oxygen-containing groups on the surface. The obvious aggregation of the oxygen at the interface can largely increase the interfacial strength between the CFs and the epoxy matrix. The same reason could be used to explain the interaction between raw CFs, which contains a sizing layer to increase the interaction between CF, and epoxy matrix. As we have mentioned before, increasing the surface roughness and depositing a transition layer are two major methods to improve the interfacial properties. Here, oxidized CNT-CFs combine both methods, i.e. grafting CNTs increases the surface roughness and introduces oxygen-containing groups to increase the chemical bonding, which leads to the best interfacial strength of the four types of composites.

3.3 Partial conclusion

In this chapter, an *in-situ* tensile test was conducted in a SEM to measure the interfacial strength between CFs and the epoxy matrix.

First, the basic properties of the CFs after modification have been investigated, including the raw CFs, desized CFs, CNT-CFs, and the oxidized CNT-CFs. The results indicate that the mechanical properties of oxidized CNT-CFs can reach the same level as the raw CF, and are much better than the desized CF and CNT-CFs.

Secondly, a tensile specimen on a micrometer-scale have been designed with bond-shape. Based on the results, it was found that grafting a CNT layer on a CF surface can modify the interfacial properties and reinforce the epoxy matrix surrounding the CFs. After further oxidation of CNT-CFs, the interfacial strength can be further increased.

Thirdly, this method was applied to the GNPs/epoxy composite. Since the fracture is not along the interface of GNPs/epoxy, it is not suitable for the interface strength measurement. However, the fracture behavior can be clearly observed in a micro-scale.

Last, the STEM combined with an EDX analysis have been conducted. It was found that the interaction between oxygen-containing groups and epoxy was the crucial factor in determining the interfacial strength. This knowledge can be used to guide the modification of other types of reinforcement and fabricate composites with excellent mechanical properties.

References

1. Etcheverry, M. and S.E. Barbosa, *Glass fiber reinforced polypropylene mechanical properties enhancement by adhesion improvement*. *Materials*, 2012. **5**(6): p. 1084-1113.
2. Kelly, A. and a.W. Tyson, *Tensile properties of fibre-reinforced metals: copper/tungsten and copper/molybdenum*. *Journal of the Mechanics and Physics of Solids*, 1965. **13**(6): p. 329in1339-338in2350.
3. Mäder, E., et al., *Adhesion of PBO fiber in epoxy composites*. *Journal of materials science*, 2007. **42**(19): p. 8047-8052.
4. Zhou, W., et al., *Atomically localized plasmon enhancement in monolayer graphene*. *Nature nanotechnology*, 2012. **7**(3): p. 161-165.
5. Carter, C.B. and D.B. Williams, *Transmission electron microscopy*. 2009: Springer-Verlag US.
6. Wu, Q., et al., *Nano-analysis on the structure and chemical composition of the interphase region in carbon fiber composite*. *Composites Part A: Applied Science and Manufacturing*, 2014. **56**: p. 143-149.
7. Yang, S., et al., *Graphene - Based Nanosheets with a Sandwich Structure*. *Angewandte Chemie International Edition*, 2010. **49**(28): p. 4795-4799.

Chapter 4 Intensive EELS study of epoxy composites reinforced by graphene-based nanofillers

Introduction

In chapter 3, I carried out a multiscale study of the interface between CFs and epoxy. The STEM observations combined with EDX analysis have successfully demonstrated the influence of surface treatment of CFs. It was found that the interaction between oxygen-containing groups and epoxy was the crucial factor in determining the interfacial strength. Do these modifications have the same influence on the GNPs/epoxy composites?

In this chapter, four composites -- GNP/epoxy, O-GNP/epoxy, GO/epoxy and CNT-GNP/epoxy, are studied. First, the dynamic mechanical properties and dielectric conductivity are measured. Secondly, the STEM observations combined with EELS are conducted to understand the structure-property relationship. In the second part, several parameters for the EELS spectra are determined, such as the sample thickness, the exposure time, etc. Thirdly, EDX mapping is also conducted in this work, and indirectly evaluate the interface strength.

4.1 Experiment and characterization

4.1.1 Preparation of GNP-based nanofiller/epoxy composites

The procedure for preparing 4.0 wt.% GNP/epoxy and oxidized GNP/epoxy composites is as follows (**Figure 4.1**): 0.8 g nanofiller was mixed with 14.4 g of epoxy resin by a three-roll mill (EXAKT 80, Germany) for 30 min. The gap size between the adjacent rollers was set to 50 μm and the rotation speed was set to 30 rpm. Afterwards, 4.8 g of curing agent were manually mixed with the previous sample to obtain a homogeneous suspension. The mixture was poured into an aluminum bowl and had a thickness of 5 mm. Then, the sample was degassed for 60 min at room temperature in a vacuum oven. After that, the mold was put in an oven at 60°C for 15 h. Due to our previous work, after 15 h at 60 °C, the crosslinking was still unfinished, so the sample was annealed at 100°C for 1.5 h to complete the crosslinking reaction. The same procedure was used with three other nanofillers.



Figure 4.1 Three-roll milling method process to prepare the epoxy composites with graphene-based nanofillers.

4.1.2 TEM sample preparation by FIB

A FIB column in a SEM was used to prepare the sample for the STEM-EDX-EELS study. The 4 wt% graphene-based epoxy composites (G/Epoxy) used for the FIB-SEM were prepared by the same procedure as described in previous chapter (section 3.1.4).

The FIB sample preparation was performed in a Helios 660 (FEI) Dual Beam FIB-SEM system with a Ga⁺ ion source. First, the cross-section of the composite was identified and targeted as the region of interest (**Figure 4.2A**). Then, a 2 μm platinum (Pt) protective layer with a cylindrical shape was deposited on the surface of the target milling area (**Figure 4.2B**). A 21 nA beam current was used for the coarse milling until the sample was left with a 2 μm thickness (**Figure 4.2C**), and then a 2.5 nA beam current was used for medium milling until a

thickness of $\approx 1 \mu\text{m}$ was reached (**Figure 4.2D**). Afterwards, the section was detached from the surrounding material and transferred to a TEM half-grid for the fine thinning step (**Figure 4.2E**). Finally, the fine thinning was carried out only at the desired areas until they became transparent in the 3 kV SEM mode, using a 200 pA beam currents. The amorphous layer on the sample surface was removed with a low-energy ion beam in three steps, (i) 5 kV (41 pA), (ii) 2 kV (23 pA) and (iii) 1 kV (28 pA), respectively (**Figure 4.2F**).

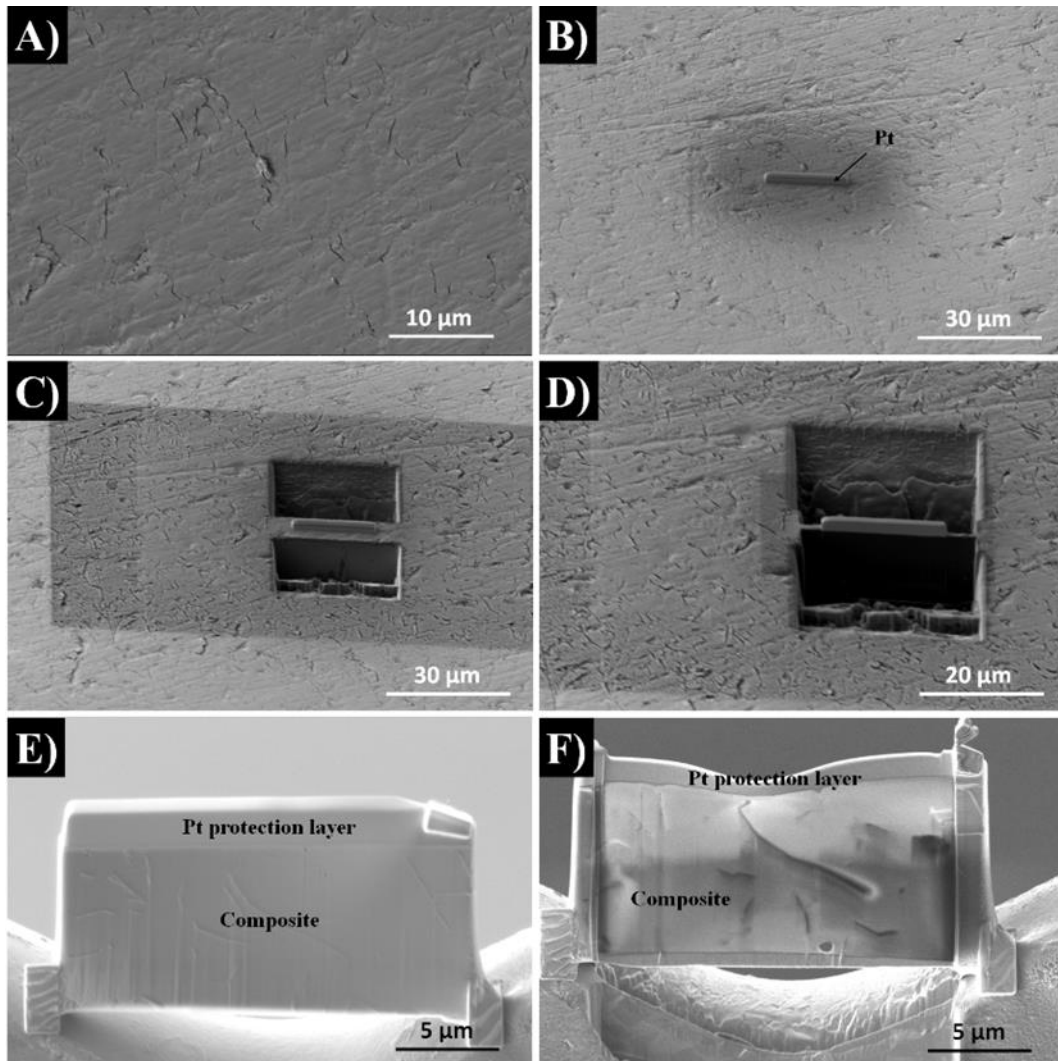


Figure 4.2 TEM sample preparation procedures by FIB.

4.1.3 Characterization

The SEM and conventional TEM characterization were conducted in the same conditions as we described in chapter 3. The sample thickness in different regions, t , was obtained from energy-loss spectra using the log-ratio method [1]. The inelastic mean free path (MFP) was calculated using the method of Iakoubovskii *et al.*[2]. The density of the pure epoxy matrix

was measured by a traditional weight-volume method. Dynamic mechanical thermal analysis (DMA) was conducted in tension mode with a Netzsch DMA 242C. The measurements were taken with a temperature ranging from 30 to 150 °C with 2 °C/min heating rate at a frequency of 1 Hz. The size of the specimen was 12mm × 5mm × 1mm. The dielectric properties were characterized as a function of the frequency (from 10 to 10⁶ Hz) by the impedance analyzer (Solartron 1260). Before the measurement, silver paints were applied on both surfaces of each sample to reduce electrical contact resistance (ECR). The sample size was 10 mm × 10 mm × 1 mm.

4.2 Results and discussion

4.2.1 Morphology characterization of nanofillers and epoxy composites

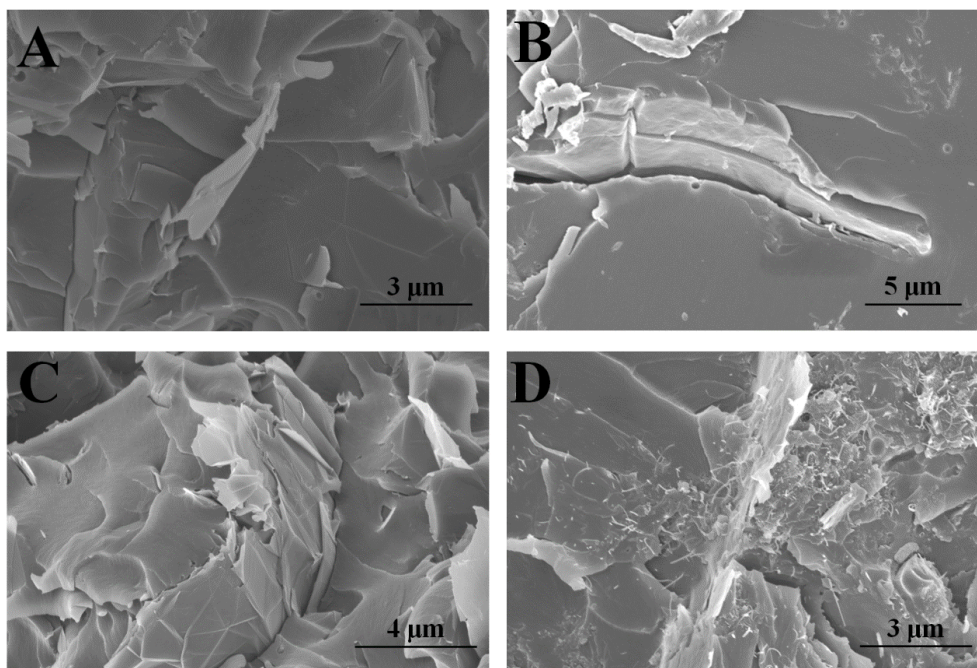


Figure 4.3 Fracture surface of G/epoxy composites with a weight fraction of 4 %, (A) GNP/epoxy, (B) GO/epoxy, (C) O-GNP/epoxy and (D) CNT-GNP/epoxy, respectively.

Figure 4.3 shows the cross-section of G/epoxy composites. After mixing by the three-roll milling method, the nanofillers homogeneously distribute in the matrix. In **Figure 4.3A**, some GNPs are directly pulled out from the epoxy matrix with a smooth surface, which infers the weak interfacial connection between original GNPs and matrix. Since the sample was prepared by a brittle fracture method in liquid N₂, the weak interface may have already separated during this process, leading to the appearance of cracks between the GNPs and the epoxy in the image.

After oxidation, many types of oxygen-containing groups are present on the GO surface, such as hydroxyl, carboxyl and epoxy. These groups can react with the curing agent during the solicitation process, which leads to a stronger interface. However, the three-roll milling process cannot exfoliate the aggregation of GO. Hence, the separation can happen between the GO layers during the fracture. In **Figure 4.3B**, some traces of wrinkled surfaces of GOs appear. **Figure 4.3C** shows the fracture surface of an O-GNP/epoxy composite. There are a few differences compared to the original GNP/epoxy composite. **Figure 4.3D** shows the SEM morphology of the fracture surface of a CNT-GNP/epoxy composite, where, due to the CNTs grown perpendicularly to the platelets, the CNT-GNPs are well immersed in the epoxy matrix, without aggregation. The coupling of 1D and 2D structures displays the maximum effective surface, leading to a largely augmented interfacial adhesion.

4.2.2 Composite properties

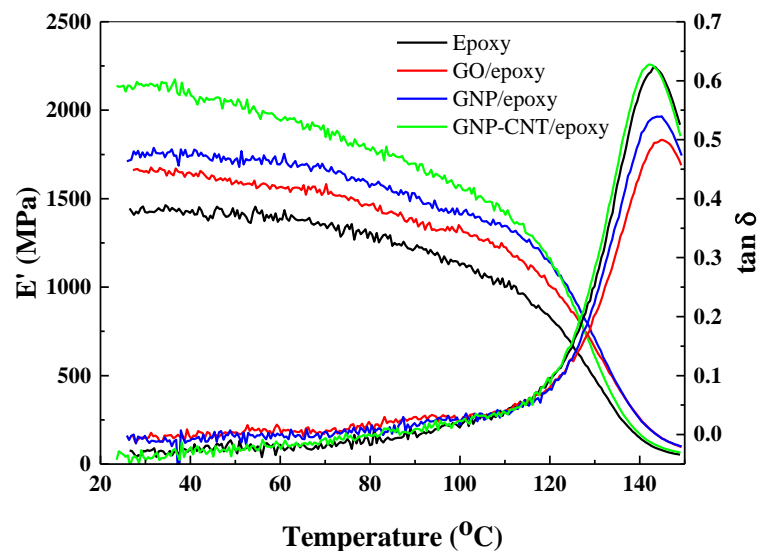


Figure 4.4 Dynamic mechanical modulus E' and loss tangent ($\tan \delta$) versus temperature of 4 wt% G/epoxy composites compared to pure epoxy.

The thermo-mechanical and flexural properties of G/epoxy nanocomposites are investigated by dynamic mechanical analysis in tensile mode. The results are shown in **Figure 4.4**.

The pure epoxy has a storage modulus of 1450 MPa at 30 °C. After incorporating 4 wt% GO nanofillers, the storage modulus increases to about 1600 MPa, 10 % increasing comparing to the pure epoxy. It is reasonable since the GO tend to aggregate in the matrix as confirmed

by SEM. The storage modulus increases to the value of 1750 MPa for the GNP/epoxy composites, due to the better dispersion of the GNP nanofillers compared to GO. However, GNPs can be used as “lubricant”, the relative movement could happen in the interlayer, which decrease its enhancement. The CNT-GNP/epoxy composite has the largest storage modulus of the three composites (at the same weight fraction), which reaches the value of 2200 MPa. The coupling of CNTs and GNPs could effectively reduce the “lubricant” effect of the GNPs. Furthermore, the presence of CNTs can reinforce the surrounding matrix at the GNP interface.

Since the glass transition temperature (T_g) of composites is below 150°C, the experiment is conducted in the temperature range of 25°C (room temperature) to 150°C. The glass transition temperature value, T_g , is evaluated according to the temperature corresponding to the loss tangent peak in the DMA curve. It reflects the transition of the composite materials from a hard glass state to a soft rubber state, due to the internal movement of the polymer chains. As shown in **Figure 4.4**, the glass transition temperature of the different G/epoxy composites are in a narrow range between 139°C and 142°C, and comparable with the pure epoxy, which indicates that the GNPs studied in this work did not degrade the thermal stability of the structural composites.

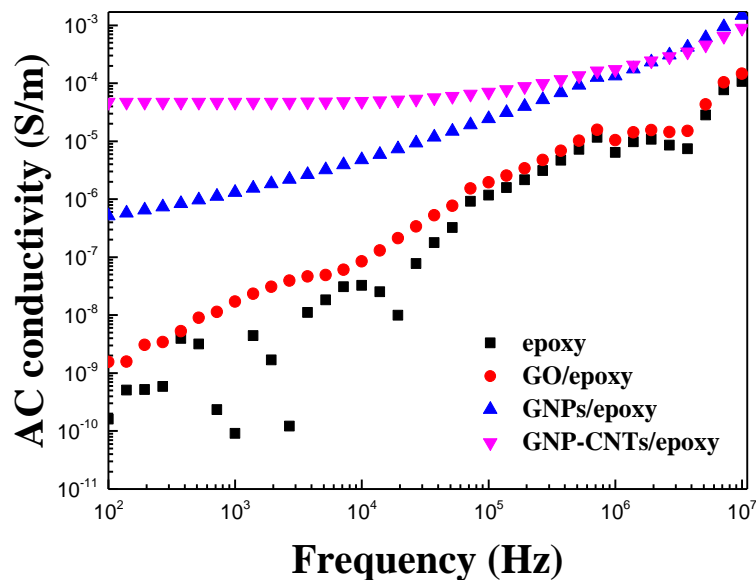


Figure 4.5 Frequency dependence of Alternating Current (AC) conductivity for the 4 wt% G/epoxy composites compared with pure epoxy.

Figure 4.5 presents the frequency dependence of AC conductivity for pure epoxy and for the different G/epoxy composites. The AC conductivity increases significantly with the increase of frequency for all the samples from 10 to 10^7 Hz. It also varies with the different nanofillers in the epoxy matrix. The CNT-GNP/epoxy composite has the best AC conductivity in all the ranges. The original GNP/epoxy has a lower AC conductivity than the GNP-CNTs/epoxy in the low frequency range. However, in the high frequency range (above 10^6 Hz), the GNP/epoxy composite has the same performance as the CNT-GNP/epoxy one. After oxidation, the intrinsic properties of the GOs are largely damaged, it contributes few for the electrical properties in the epoxy composites.

4.2.3 EELS study

4.2.3.1 Influence of sample thickness for EELS acquisition

It is very useful to measure the local thickness of a specimen since it affects largely the part of the spectrum influenced by plural-scattering. Usually, the thickness could be obtained from the low-loss spectrum, named as the log-ratio method. The equation is given by [3]:

$$I_0 = I_t \exp\left(\frac{-t}{\lambda}\right) \quad (4.1)$$

where I_t is the total intensity integrated up to a suitable (but arbitrary) energy-loss (as shown in **Figure 4.6**),

I_0 is the zero-loss intensity,

t is the specimen thickness,

and λ is the inelastic MFP for an energy loss lower than a given value.

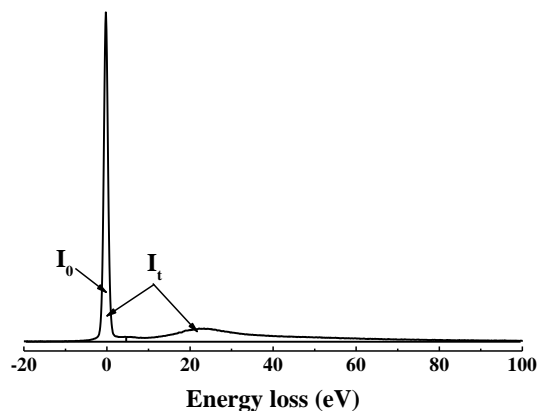


Figure 4.6 the integrals and energies involved in measuring the low energy region of the loss spectrum.

Based on Iakoubovskii's work [2], measured on a wide range of solids, the equation follows a scaling law:

$$\frac{1}{\lambda} = \frac{11\rho^{0.3}}{200FE_0} \ln \left\{ \frac{\alpha^2 + \beta^2 + 2\theta_E^2 + |\alpha^2 - \beta^2|}{\alpha^2 + \beta^2 + 2\theta_C^2 + |\alpha^2 - \beta^2|} \times \frac{\theta_C^2}{\theta_E^2} \right\} \quad (4.2)$$

$$F = \frac{\left(1 + \frac{E_0}{1022}\right)}{\left(1 + \frac{E_0}{511}\right)^2} \quad (4.3)$$

$$\theta_E = \frac{5.5\rho^{0.3}}{FE_0}, \quad \theta_C = 20 \text{ mrad}$$

where E_0 is the acceleration high voltage in TEM (in kV units),

F is the relativistic correction factor,

α and β are respectively the convergence and collection semi-angles in the EELS acquisition system,

θ_E is the characteristic angle of inelastic scattering corresponding to an energy loss E ,

and ρ is the density of the probed region.

In my experiment, I used $\alpha = 17.9$ mrad and $\beta = 7.2$ mrad. Hence, the first equation can be simplified as:

$$\frac{1}{\lambda} = \frac{11\rho^{0.3}}{200FE_0} \ln \left\{ \frac{\alpha^2 + \theta_E^2}{\alpha^2 + \theta_C^2} \times \frac{\theta_C^2}{\theta_E^2} \right\} \quad (4.4)$$

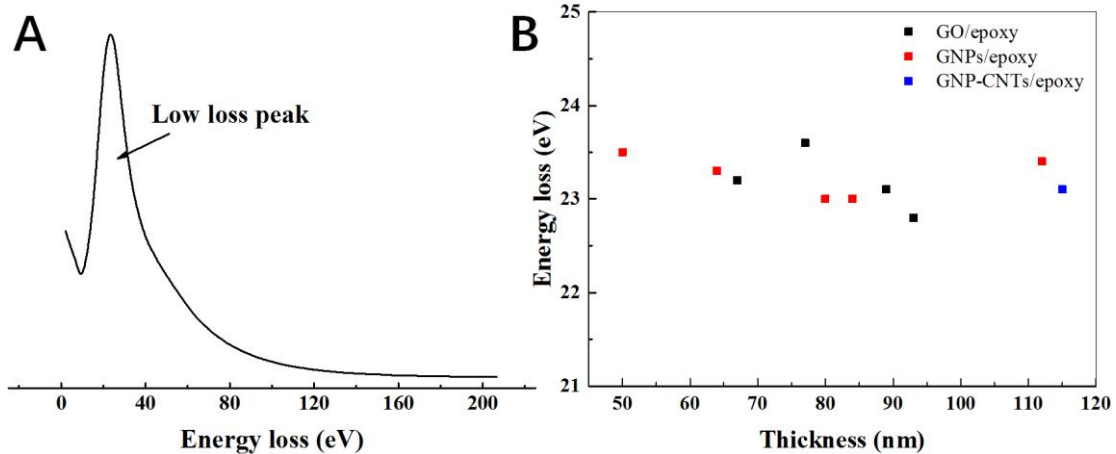


Figure 4.7 (A) Low-loss spectra of epoxy matrix; (B) Peak positions extracted out from low-loss spectra of three different samples as a function of sample thickness (measurements in the epoxy matrix part only).

To verify the thickness of our samples, different regions are chosen in the matrix as the tested regions. The density of pure epoxy is measured by a traditional mass-volume method. A 10 mm × 10 mm × 2 mm sample is polished manually and balanced. Three samples are tested to decrease the variation. Finally, a density of 1.13 g/cm³ is obtained for pure epoxy.

The low-loss peak is also referred to as the plasmon excitation, which reflects the solid-state character of the specimen. For polyaromatic solids, the low loss area exhibits two main plasmon peaks, which are ascribed to the excitation of π and $\pi+\sigma$ electrons, as shown in **Figure 4.7A**. The $\pi+\sigma$ peak is located at 20-25 eV for polymers and 23.5-27 eV for amorphous carbon and graphite.

All the peak values are extracted from the low-loss spectra of epoxy matrix from three different samples, and the values are showed in **Figure 4.7B** as a function of thickness. It can be found that the peak values are in the range of 22.8-23.6 eV. As the thickness increases, the values have few changes. It can be concluded that the values of the low-loss peaks do not depend on the thickness in a certain range.

4.2.3.2 Influence of exposure time on the core-loss spectra

The polymer matrix is very sensitive to the electron beam. A long exposure time under the electron beam induces great damages to the sample structure. In my experiment, to decrease the damage, I used a high tension of 80 kV for TEM characterization. To study the influence of exposure time on the EELS spectra and TEM images, a region with epoxy matrix is chosen and irradiated under the electron beam in TEM mode. The chosen exposure times are 0, 1, 5, 10 min. The core-loss spectra and TEM images are showed in **Figure 4.8**:

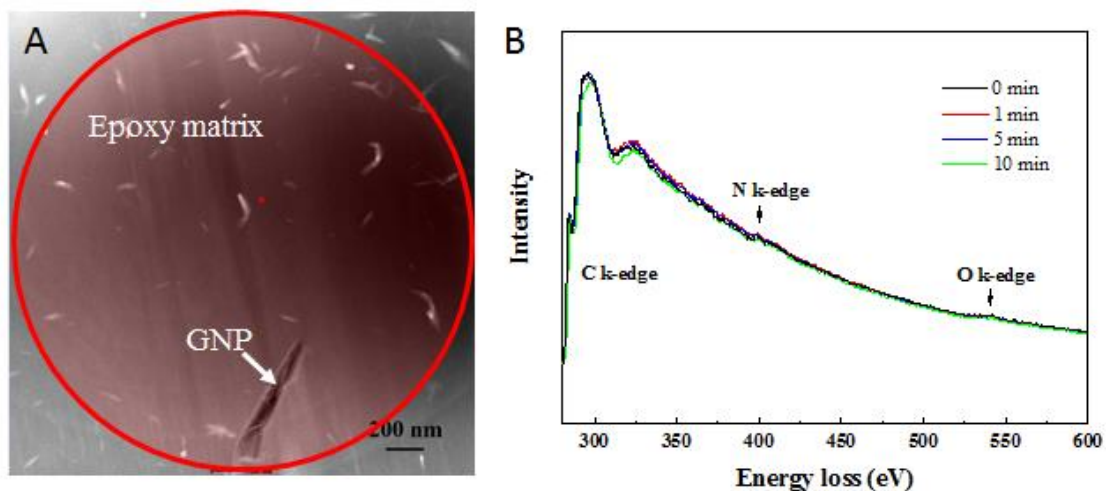


Figure 4.8 (A) region selected for electron beam irradiation at 80 keV, the red circle indicates the area and is controlled by the aperture II; (B) Related core-loss spectra with different time exposures.

After irradiation of the matrix part, there is no change in the STEM image, as shown in **Figure 4.8**. However, a small piece of GNP (indicated by the arrow) separates from the matrix as the irradiation time increases. In **Figure 4.8B**, I show the core-loss spectra of epoxy matrix acquired after different exposure times. The C, N and O K-edge can be easily distinguished from the spectra, and there is no obvious change from one spectrum to the other. It can be concluded that the electron beam irradiation at 80 keV for less than 10 min has few effects on the core-loss spectra.

4.2.3.3 Influence of the sample thickness on the core-loss spectra

TEM and STEM investigations were performed on the composite films prepared by FIB. **Figure 4.9(A-C)** shows HAADF-STEM images for different G/epoxy composite films. For the GNP/epoxy composite in **Figure 4.9A**, the GNPs could be easily recognized with their whiter contrast, which is due to the larger thickness compared to the surrounding matrix. Since GNPs have a much higher hardness than the epoxy matrix, I could not achieve the same level of thickness in the same milling conditions. What more, the upper side of the images is darker than the bottom, which is also caused by a small difference in thickness. **Figure 4.9B** shows a GO/epoxy composite. Though less contrast exists between GO and matrix, the GO is clearly distinguished in the central part with a thickness of several hundred of nanometers. The interface between the GO and matrix is rougher than that of GNP and matrix. The traces on the surface are due to the milling process. There is also a small different contrast in the matrix part due to the thickness variation. **Figure 4.9C** demonstrates a CNT-GNP/epoxy composite, the GNP having a platelet shape on the right side, the grafted CNTs are well dispersed in the surrounding matrix.

In three HAADF-STEM images, the thickness is measured at three different spots, and the values are listed in **Figure 4.9(D-F)**. In the GNP/epoxy sample, 5 positions are marked out in the epoxy matrix, where low-loss and core-loss spectra were acquired. The $\ln(I_t/I_0)$ values are calculated by the DM software. The inelastic MFP of the matrix is calculated as 113 nm. For all test position in the epoxy matrix, the thickness is lower than the inelastic MFP, and the thickness even reaches 50 nm at some point. 6 positions are marked out in the GO/epoxy

sample, in which points 4 and 5 are in the GO region, the others being in the epoxy matrix. All the thicknesses are lower than 100 nm. In the CNT-GNP/epoxy sample, the thickness is greater than with the two other samples, and is around 110 nm.

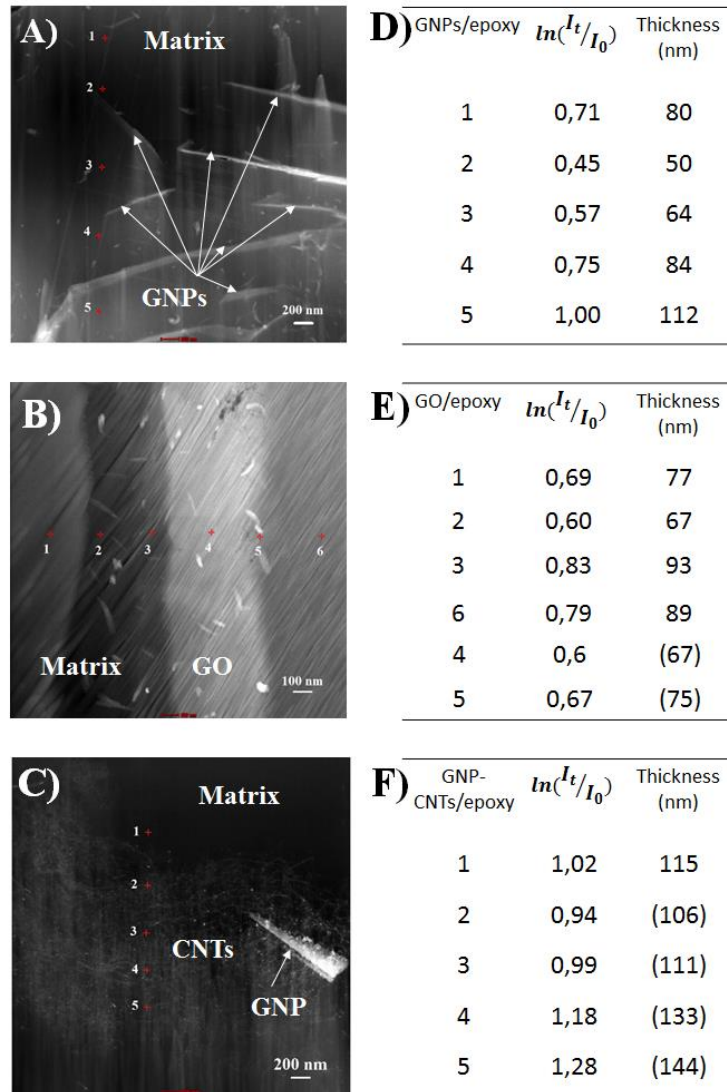


Figure 4.9 HAADF-STEM images of (A) GNP/epoxy, (B) GO/epoxy and (C) CNT-GNP/epoxy composites; Tables (D-F) show the thickness values of each point measured in images (A-C), respectively.

EELS are effective to obtain fingerprint chemical information (i.e. electronic structure of the atoms, type of bonding, nearest-neighbor chemical environment). To study the influence of the thickness on the core-loss spectra, the five spectra are probed at the points marked out in **Figure 4.9A** corresponding to situations with different thicknesses. In **Figure 4.10A**, the

individual oxygen peak at approximately 530 eV can be clearly observed on all five spectra with the similar peak intensity. Meanwhile, a clear nitrogen peak at 400 eV appears in the thicker points and gradually decreases as the thickness decreases.

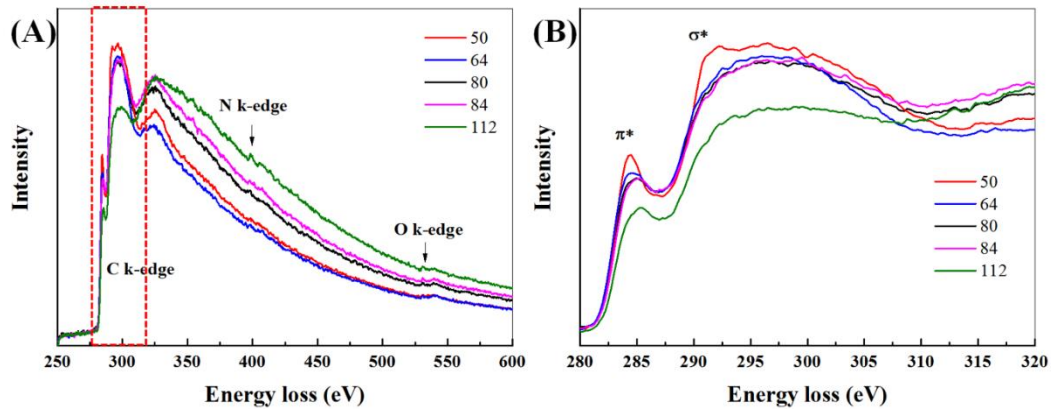


Figure 4.10 (A) Energy-loss spectra in the C K-edge, N K-edge and O-K edge ranges with different sample thicknesses; (B) Enlarged C K-edge marked out with the red rectangle in (A).

Table 4.1 The thickness influence on the O/C and N/C ratios in the epoxy matrix.

Thickness (nm)	50	64	80	84	112
O/C ratio (%)	8.62	6.04	7.42	10.2	10.57
N/C ratio (%)	2.32	0.78	2.28	1.69	1.10

Although all five spectra were acquired from the pure epoxy matrix, the thickness lead to different intensities of a specific element. Based on this result (as shown in **Table 4.1**), a relatively thick area could have a higher inelastic cross-section, which leads to a greater sensitivity to the N and O element.

In **Figure 4.10B**, the C K-edge spectra of the five points show an energy-loss around 294 eV. A clear feature of the peak at 294 eV is attributed to the C=O π^* resonance and the peak at 292 eV is attributed to the carbon sp^3 bond (C-C σ^* resonance). For the 112 nm-thick sample, the spectrum is relatively smooth, but a few peaks can be distinguished. However, for the 50 nm-thick sample, it is possible to identify the low-signal peaks, i.e. the fine structures. Rosenberg *et al.* [4] have reported that those low-signal peaks do not correspond to noise but to transitions. Based on this, the thinner sample is more sensitive in the C K-edge energy-loss range.

4.2.3.4 Low-loss and core-loss spectra of G/epoxy composites

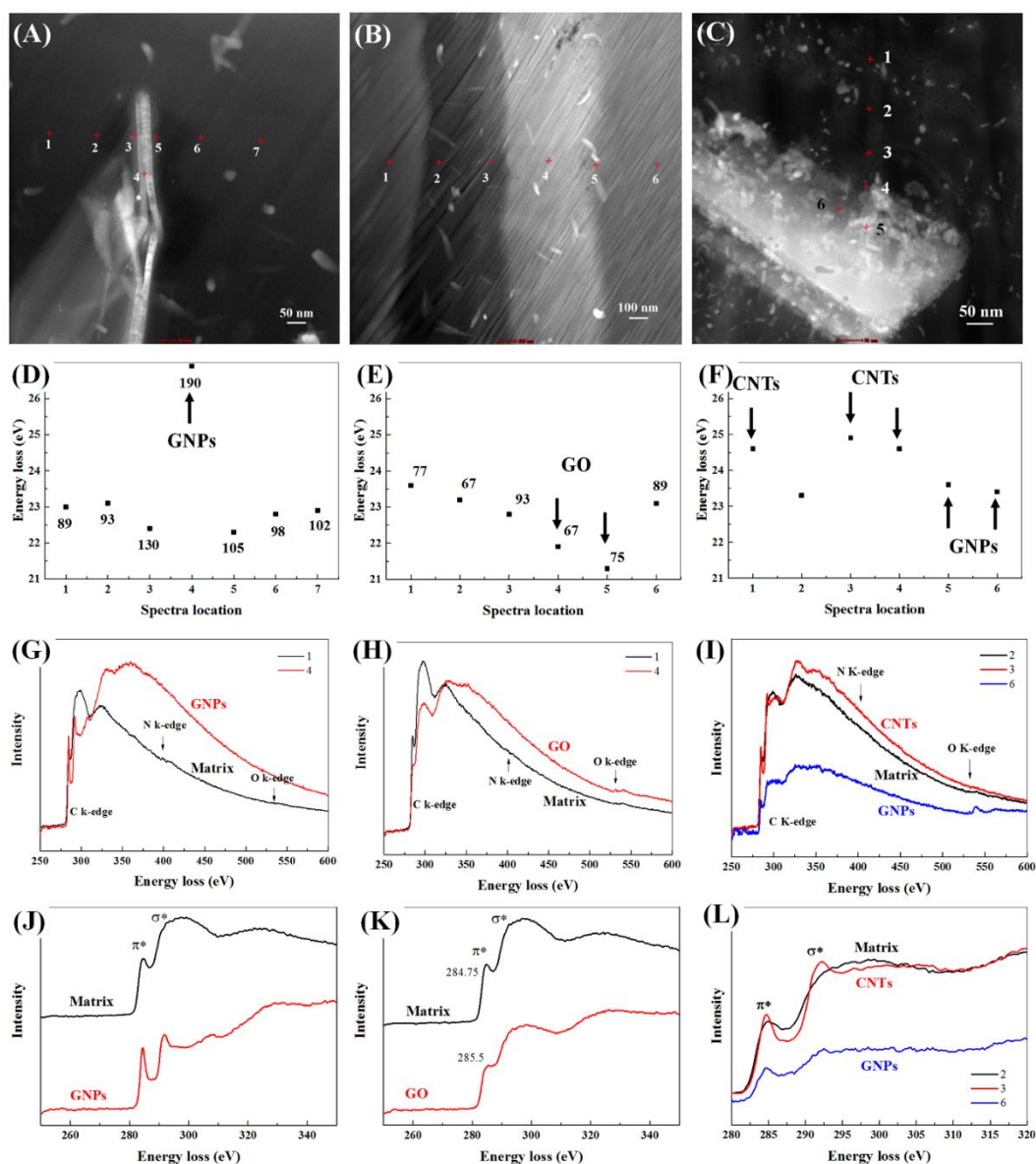


Figure 4.11 HAADF-STEM images of (A) GNP/epoxy, (B) GO/epoxy and (C) CNT-GNP/epoxy composites. (D-F) Corresponding plasmon peak measurements. (G-I) Corresponding core loss spectra. (J-L) Corresponding C K-edges.

Based on Ferrari's study [5], the low loss peak position can be used to evaluate the mass density of the probed region. To analyze different phases in the composites, the low loss spectra were acquired from all three composites. **Figure 4.11A** shows the HAADF STEM image of a GNP/epoxy composite, in which the bright thin line in the center corresponds to the GNP. Seven spots are analyzed using EELS, the fourth being in the GNP region and the others six

points being in the matrix part. The same acquisitions are performed in GO/epoxy matrix on six different spots, in which the fourth and fifth points are in the GO region, as shown in **Figure 4.11B**. For CNT-GNP/epoxy composites, since the CNTs have an average thickness of 50-80 nm, a higher magnification is used to ensure that some points were acquired from the CNT region, as shown in **Figure 4.11C**. The tubular structure of CNTs could be clearly observed at this magnification. Among the six points chosen in GNP-CNTs/epoxy composites, the first, third and fourth points are probed on the CNT part. The second point is probed on the matrix and the fifth and sixth are probed on the GNP region.

The low-loss peak values are extracted out from the spectra and their locations represented as shown in **Figure 4.11(D-F)** for GNP/epoxy, GO/epoxy and CNT-GNP/epoxy composites, respectively. For all spectra acquired from the three samples, the energy loss is in the range of 22.5-23.6 eV. There is a small variation between them nonetheless, which is quite reasonable since all the components cannot be identical during the crosslinking reaction. However, in the GNP/epoxy composite, the energy-loss corresponding to the GNP region (26.9 eV) is much higher than that in the matrix part. In the GO/epoxy composite, the energy-loss of GOs is in the range of 21.3-21.8 eV, a little lower than that of the matrix. In the hybrid reinforced composite, the CNTs have an energy-loss value of 24.5 eV, in between the matrix and the GNP values. However, the energy-loss of the GNP part in the hybrid is even smaller than that of the CNTs, and at the same level as the matrix.

Since GOs, GNPs, CNTs and the matrix are composed of one or several light elements, C, O and N, the weight and valence density of these three elements have a very small discrepancy. Hence, their difference in energy-loss can directly reflect the variation of the mass density. To confirm the experimental results, the mass densities of the GOs, GNPs, CNTs and epoxy are either found from the literature or calculated directly, and give 1.06, 2.25, 2.1 and 1.13 g/cm³, respectively. Compared to these values, the energy-losses in GNP/epoxy and GO/epoxy are in a very good agreement with the density results. However, for the CNTs, the energy-loss is smaller than for GNPs. For the CNT-GNP/epoxy composite, the specimen thickness is around 100 nm, and is greater than the diameter of the CNTs, in the range of 50-80nm. Hence, even when the probe is focused on the CNT, the low-loss peak contains a part of the signal of the surrounded matrix (as shown in **Figure 4.12**). The energy-loss is a weighted average value of the CNTs and the matrix.

Since the low-loss spectrum can reveal the density variation in the different region, a more detailed analysis of the density variation in the interface region are studied and presented in chapter 5.

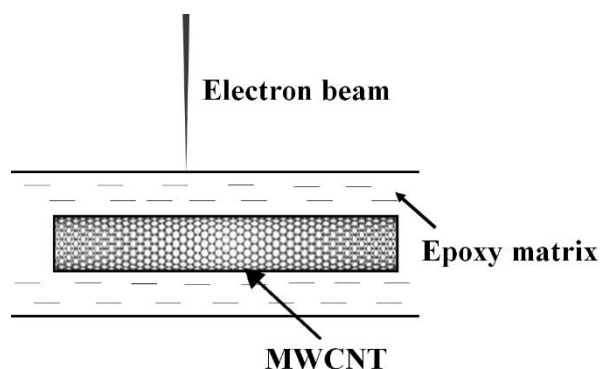


Figure 4.12 A scheme of the cross-section of CNT-GNP/epoxy sample where the electron beam pass through the MWCNT region.

To confirm the fine structure of the nanofillers and the epoxy matrix, the core-loss spectra have been acquired in the different phases of all three types of composites. **Figure 4.11G** shows the core-loss spectra of the GNPs and epoxy matrix acquired from the first and fourth points in **Figure 4.11A**, respectively. The spectra of the matrix are discussed intensively and to make a comparison with the GNPs, the O K-edge at 530 eV and N K-edge at 400 eV do not appear in the GNP spectrum. The GNPs used here have maintained their composition during the composite fabrication process. **Figure 4.11J** zooms on the C K-edge at 284 eV to study the fine structures. The C K-edge of the matrix is very similar to the amorphous carbon case. However, the C K-edge of GNPs shows two obvious peaks at 284 eV and 292 eV, which corresponds to the $1s$ to π^* and $1s$ to σ^* transitions, respectively. The peak shapes are very similar to graphite, indicating its sp^2 layered structure. **Figure 4.11H** shows the core-loss spectra of a GO and matrix. The spectra of the epoxy matrix exhibit very few differences from one type of composite to the other. For the GO spectrum, the O K-edge at 530 eV appears more strongly due to the oxidation process. **Figure 4.11K** shows the enlarged C K-edge of the matrix and the GO. Few differences could be distinguished from these two spectra, indicating that the GO becomes amorphous after oxidation. For the CNT-GNP/epoxy composite, three core-loss spectra corresponding to the matrix, CNTs and the GNP, have been acquired and shown in **Figure 4.11I**. The spectrum of CNTs is a mixed signal of the CNTs and the matrix. The N K-

edge and O K-edge are not as strong as in the matrix. However, a very strong O K-edge appears in the GNP spectrum, which indicates that the GNP has been oxidized in the hybrid composites. The C K-edge shown in **Figure 4.11L** has a great difference entre three phases. The CNT C K-edge shows obvious π^* and σ^* transition peaks due to its graphitic structure. These two peaks are very weak in the GNP spectrum due to the oxidation.

4.2.4 Energy dispersive X-ray spectroscopy (EDX) characterization of G/epoxy composites

To further confirm the element distribution in the three composites, energy-dispersive analysis (EDX) mapping was acquired in four composites, as shown in **Figure 4.13**. Once the proper threshold applied to transform the spectrum intensity of a given pixel into a colored pixel, the brightness of a given element color represents the relative concentration of this element. **Figure 4.13A** presents a STEM image of a raw GNP/epoxy composite. The bright region in the center corresponds to the GNP and the two sides with the relatively low brightness correspond to the epoxy matrix. A region in the center has been selected to perform the EDX analysis and two elements, oxygen and carbon, have been analyzed. The HAADF image shows the morphology after EDX acquisition. To obtain a high-resolution mapping, 10 mins have been used to do the acquisition. Some damages were observed afterwards since the polymer matrix is very sensitive to electron irradiation: The interface was broken, which gives an evidence that original GNPs have a weak interaction with epoxy matrix. Since the GNPs contain the carbon element only and have a higher density than the matrix part, carbon is shown with a brighter color in the GNP region than in the matrix. There is no oxygen in the GNP part, but a weak signal still exists, due to the FIB milling process which introduces a small amount of oxygen. The oxygen in the GNP domain is much lower than in the matrix. **Figure 4.13B** shows the EDX mapping of the O-GNP/epoxy interface region, where carbon and oxygen mappings were also acquired. The carbon mapping has no obvious difference compared to GNP/epoxy, and is brighter in the GNP domain. However, the situation is totally different for oxygen, which tends to aggregate at the interface, indicating the induced chemical bonding.

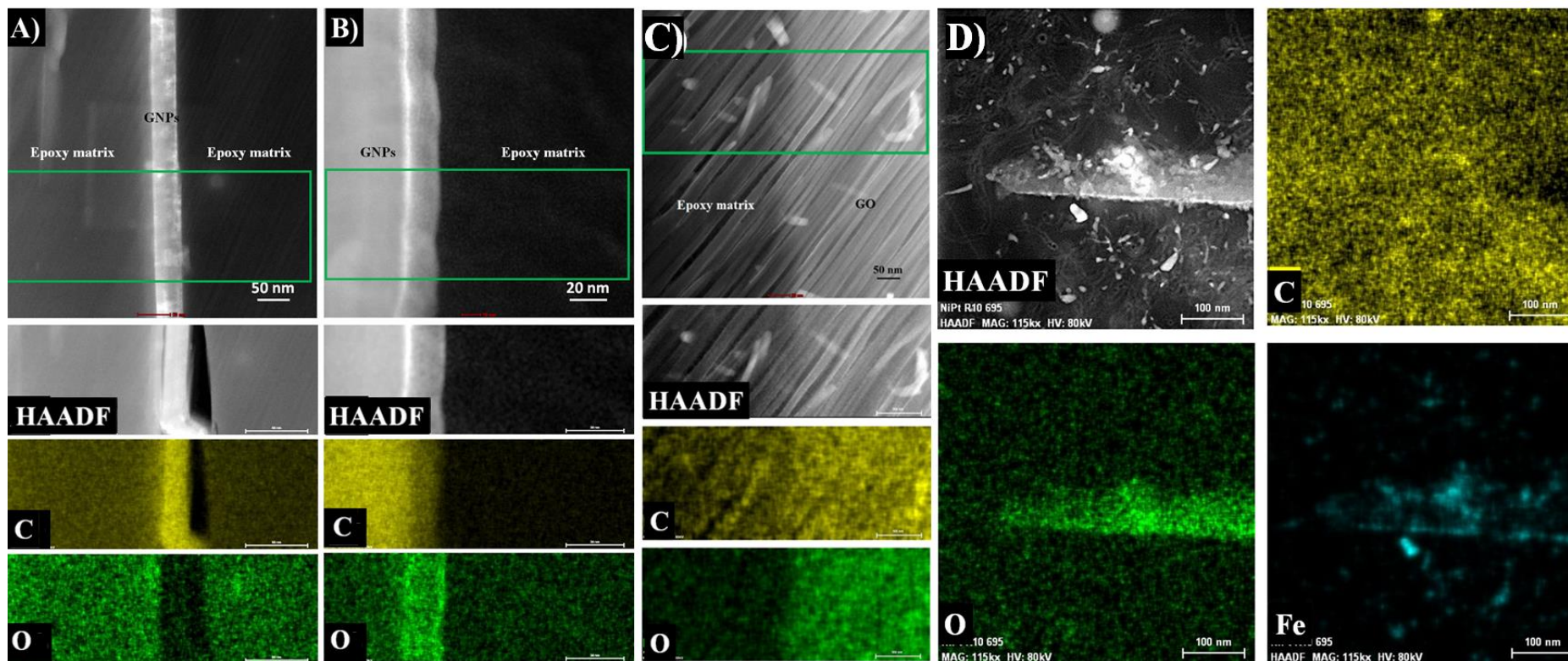


Figure 4.13 High magnification STEM Z-contrast (HAADF) image showing the nanofillers in the epoxy matrix: (A) GNP/epoxy, (B) O-GNP/epoxy, (C) GO/epoxy and GNP-CNT/epoxy composites. The regions marked out by green rectangular in (A) and (B) and the entire region in (C) were analyzed by energy dispersive X-ray spectroscopy (EDX), the elements were marked out by different colors, green for oxygen, yellow for carbon, and blue for iron, respectively.

Figure 4.13C shows a STEM image of a GO/epoxy composite. After oxidation, GOs have a very similar composition compared to the matrix, which decreases the contrast. The HAADF image shows the state after the acquisition, where the interface is not broken. The oxygen-containing groups in the GO could react with the curing agent in the matrix, and build a strong interface. The C mapping shows very few differences. However, the GOs domain shows a relatively higher concentration of oxygen compared to that of the matrix part. **Figure 4.13D** shows the EDX mapping of a CNT-GNP/epoxy composite, where three elements -- carbon, oxygen and iron -- were acquired. The HAADF shows the clear tubular structure of the CNTs, the bright triangle part is the GNP, the bright spots the iron catalyst. The carbon mapping shows very few differences in the region. However, the GNP part has a much higher oxygen concentration than the other parts, which confirms the conclusion made before. The GNPs have been oxidized in the hybrid composite. The iron mapping confirms the presence of the catalyst.

4.3 Partial Conclusion

In this work, four kinds of composites, GNP/epoxy, O-GNP/epoxy, GO/epoxy and CNT-GNP/epoxy composites, have been studied. First, the mechanical and electrical properties of the composites were measured. The results indicate that the CNT-GNP/epoxy composite has the best performance in both DMA and conductivity tests. Secondly, the nanoscale characterization of four composites has been conducted by combining STEM-EELS-EDX observations. The effect of the TEM sample thickness and electron irradiation time have been investigated. It can be found that the thickness under 120 nm has a limited effect on the low-loss spectra. However, in a certain range, thicker samples have a better element sensitivity to the N and O K-edge peaks. Thirdly, the low-loss and core-loss spectra of the four kinds of composites have been studied intensively. The element composition in the different samples could be easily obtained with the core-loss spectra. The density varied in the matrix and nanofiller domains. More details about the density change in the interface between the matrix and the nanofillers will be presented in chapter 5. Finally, an EDX mapping was also conducted in this work, the difference at the interface caused by the surface treatment could be easily observed, and could be used to indirectly evaluate the interface strength.

References

1. Malis, T., S. Cheng, and R. Egerton, *EELS log - ratio technique for specimen - thickness measurement in the TEM*. Microscopy Research and Technique, 1988. **8**(2): p. 193-200.
2. Iakoubovskii, K., et al., *Thickness measurements with electron energy-loss spectroscopy*. Microscopy research and technique, 2008. **71**(8): p. 626-631.
3. Egerton, R.F., *Electron energy-loss spectroscopy in the electron microscope*. 2011: Springer Science & Business Media.
4. Eberlein T, Bangert U, Nair RR, Jones R, Gass M, Bleloch AL, et al. Plasmon spectroscopy of free-standing graphene films. *Phys Rev B* 2008;77(23):233406–233409.
5. Ferrari, A.C., et al., *Density, sp^3 fraction, and cross-sectional structure of amorphous carbon films determined by X-ray reflectivity and electron energy-loss spectroscopy*. *Physical Review B*, 2000. **62**(16): p. 11089.

**Chapter 5 Quantitative Study of Interface/Interphase
in Epoxy/Graphene-based Nanocomposites
by Combining STEM and EELS analyses**

Introduction

In chapter 4, I studied the influence of the sample thickness on the EELS spectra, including the low-loss and core-loss spectra. In the low-loss spectrum, a broad peak appears in the range from 22 eV to 25 eV. When comparing the low-loss spectra of GNPs with those of epoxy, I found that the low-loss peak of GNPs shifts towards higher energy-loss than epoxy. However, the low-loss peak of GOs shifts towards lower energy-loss region compared with epoxy, and corresponds to the excitation of $\pi+\sigma$ electron in the polyaromatic solid. This peak position is identified as E_p [1].

According to the expression relating the plasmon energy to the valence electron density, e.g. [2],

$$E_p = \hbar \left(\frac{n_e e^2}{\epsilon_0 m^*} \right)^{\frac{1}{2}} \quad (1)$$

where n_e stands for the valence electron density,

ϵ_0 for the vacuum dielectric function,

m^* an m for the electron effective mass, and the free electron mass, respectively.

The mass density is derived from the valence electron density n_e by assuming that carbon contributes with four valence electrons, oxygen with six and hydrogen with one, to obtain

$$n_e = 12 \frac{\rho N_A}{M_C} \left(\frac{3X_C + 5X_O + 1}{11X_C + 15X_O + 1} \right) \quad (2)$$

with $X_H = 1 - X_C - X_O$,

where X_H , X_C and X_O correspond to the element fraction of hydrogen, carbon and oxygen, respectively;

ρ is the overall density of tested region;

N_A is the Avogadro constant;

M_C is the molar mass of carbon

Thus, the mass density is given by:

$$\rho = \frac{\epsilon_0}{12\hbar^2 N_A e^2} M_C m^* E_p^2 \left(\frac{11X_C + 15X_O + 1}{3X_C + 5X_O + 1} \right) \quad (3)$$

Thus, for the same chemical component region, a high value of E_p usually leads to a high density. In the epoxy matrix, the mass density behaves as:

$$\rho \propto E_p^2 \quad (4)$$

In chapter 4, a quantitative analysis of the interphase observed in the GNP/epoxy composite by STEM/EELS has not been reported in detail. Hence, in the present chapter, I present a detailed STEM/EELS analysis of composites reinforced by pristine GNPs or GOs. The images undeniably reveal the presence of GNPs and GO inside the polymer matrix. An EELS analysis, and more precisely a low-loss peak analysis, is presented as a powerful tool to identify the valence electron density in the tested region. Furthermore, the physical density of the materials is carried out using the equations presented in [2] to have a quantitative evaluation on the interphase density. Interphase thicknesses of different nano-fillers are also compared.

5.1 Results and discussion.

5.1.1 GNP/ & GO/epoxy nanocomposites

Figure 5.1 shows SEM images of GNP/epoxy (**A**) and GO/epoxy (**B**) nanocomposites with 1.0 wt%. After incorporation into the polymer matrix, the GNPs are homogeneously distributed. Besides, some GNPs are pulled out directly from the epoxy matrix. On the contrary, the GO/epoxy nanocomposite shows some platelet aggregations, as marked out by the red circles. GO and epoxy have a similar composition, they are difficult to identify by SEM. The existing oxygen-containing groups on the GO surface enable to enhance the interaction with the epoxy matrix. Furthermore, after oxidation, the platelet size decreases.

Figure 5.1(C) presents a STEM image of a GNP/epoxy composite, in which the bright region in the upper side shows the pure epoxy with a larger thickness due to the inappropriate thinning process during sample preparation. At the bottom, the relatively thin region contains a GNP platelet. The in-plane of GNPs is approximately perpendicular to the sample foil. Both sides of the GNP edges adhere to the matrix, and show a bright grey color. In the thin region, the epoxy has a homogeneous grey color, indicating the uniform thickness in this part.

Figure 5.1(E) shows a STEM image of a GO/epoxy composite. During the three-roll process, some single layer GOs have been broken into small pieces, which appear homogeneously distributed (bright regions). However, they are not perpendicular to the sample plane. The bright line appearing in the image is the aggregation of GO layers, which are perpendicular to the plane and more suitable for the interface study.

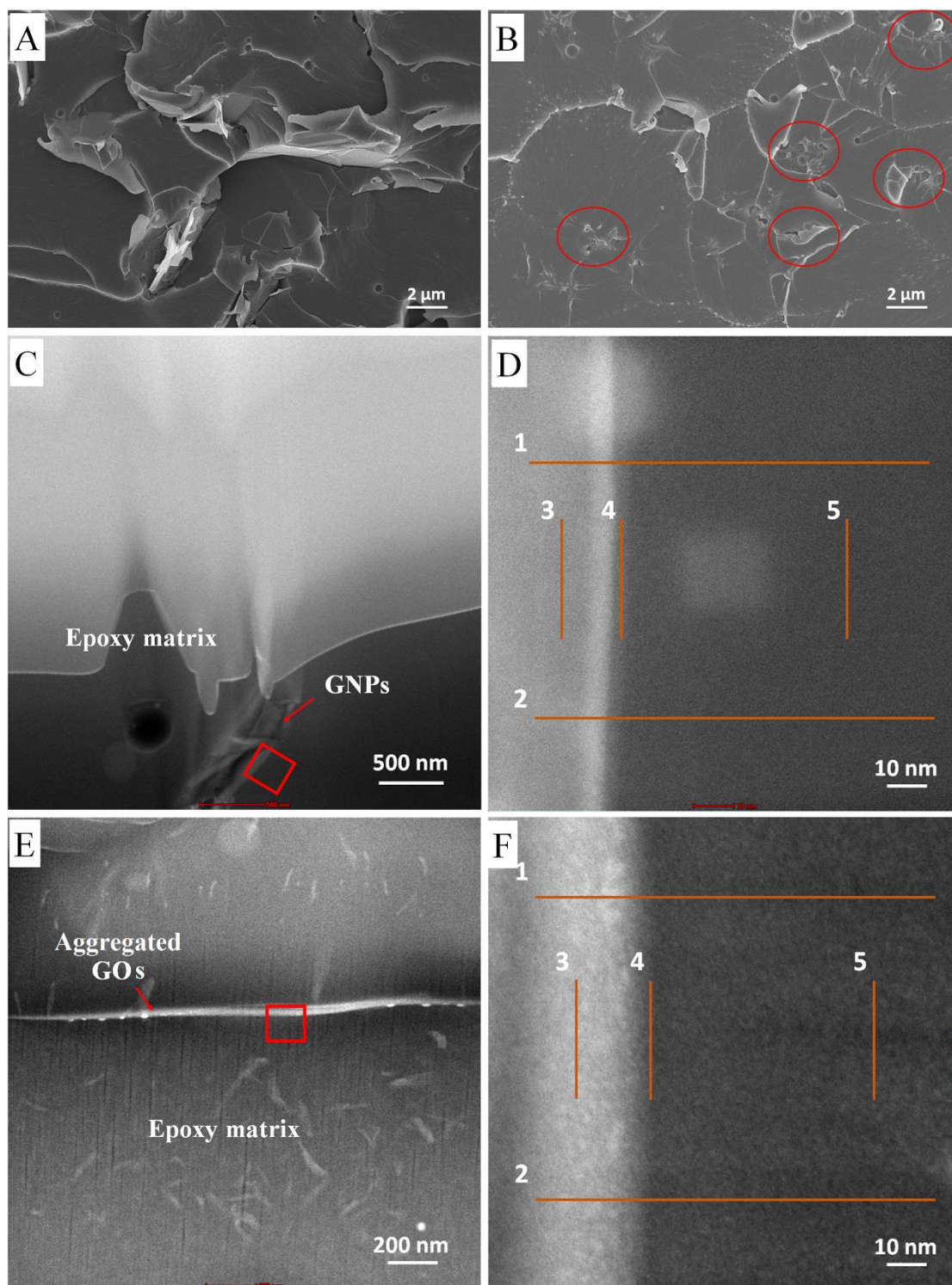


Figure 5.1 SEM images of (A) the GNP/epoxy and (B) the GO/epoxy composite fractured surface with 1.0 % weight fraction. Overview of STEM Z-contrast image showing: (C) a GNP plane perpendicular to the epoxy foil prepared by FIB, (E) the GO/epoxy sample. (D) and (F) show higher magnification Z-contrast images of the framed regions in (C) and (E), respectively. EELS analyses were carried out along the lines indicated on these images.

Two regions in **Figure 5.1(C)** and **(E)** are enlarged: **Figure 5.1(D)** and **Figure 5.1(F)** correspond to the red rectangular region in **Figure 5.1(C)** and **Figure 5.1(E)**, respectively. First, in **Figure 5.1(D)**, the dark region is the epoxy matrix while the bright one corresponds to a GNP. In high resolution, some surface bulges could be observed in the region. At the interface, the boundary is obvious and smooth, the brighter region on the GNP side and the grey region in the matrix part compose a transition layer, namely the interphase. Meanwhile, EELS spectra are acquired in the positions marked by the five orange lines, two lines across the interface with a length of 100 nm and three lines parallel to the interface with a length of 30 nm. 100 spectra were acquired on each horizontal line and 30 spectra on each vertical line leading to an average acquisition distance between two points of 0.5 nm. Secondly, **Figure 5.1(F)** is the enlargement of the red rectangle in **Figure 5.1(E)** including two domains, a GO and the epoxy matrix. The boundary is fuzzy with a continuously changing shade of gray, which is due to the better connection between the GO and the epoxy matrix. The hydroxyl and epoxy groups on the GO plane have chemical reaction with the curing agent and covalently bond to the epoxy net. Then, the same EELS acquisition process was conducted in the interphase region.

5.1.2 Interphase characterization

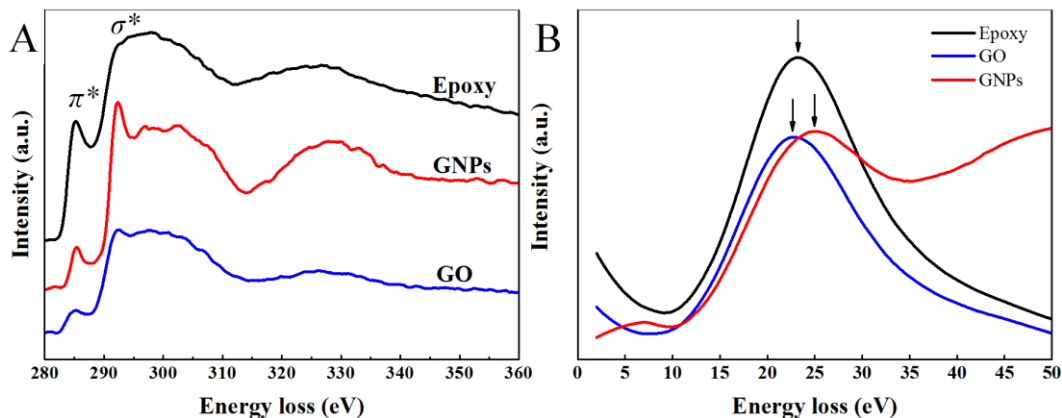


Figure 5.2 (A) Carbon core-loss and (B) low-loss spectra acquired from the epoxy matrix, a GNP and a GO, respectively.

Electron energy loss spectroscopy (EELS) is currently the preferred method to obtain the sp^3 content from the size of the π^* peak in the carbon K-edge absorption spectrum, where the low energy-loss spectrum gives the valence plasmon energy and thereby the mass density.

Normalized EEL spectra showing the carbon core-loss and low-loss are presented in **Figure 5.2**. In **Figure 5.2(A)**, it is possible to observe the differences between the response intensity of the edges and the shape of the spectral curves, namely the fine structures. At an

energy loss of 285.3 eV, the $1s$ to π^* transition is observed, while the states corresponding to a transition from $1s$ to σ^* are observed at 292 eV. These transitions are the main features of the EEL spectra of graphite and other carbon-based materials and they both correspond to the excitation fingerprint of the valence band electrons, above the Fermi level. The identification of the transitions in EEL spectra is done by carefully observing each spectrum. The only treatment employed during this task is the background subtraction and the plural scattering removal. Once these procedures are applied, the spectra are similar to those presented in **Figure 5.2(A)**. From the detailed observation of each spectrum, GNPs have a narrow and incisive π^* transition compared with the two other spectra, and are the closest to the pure graphitic spectrum. After oxidation, a GO π^* transition is still noticeable, but with a reduced intensity. However, for the epoxy matrix, the π^* transition is immersed to some low-signal peaks.

To study the physical density of the interface region, I have acquired spectra along a line across the interface region. In **Figure 5.1 (D)** and **(F)**, I have already acquired 100 low energy-loss spectra for each horizontal line and 30 spectra for each vertical line, respectively. After treatment of the spectra, the value of the peak position of each spectrum is extracted. Then, for each region, I put all the values as a function of the position as presented in **Figure 5.3**. The points are counted from the left to the right side for the lines across the interface, and from top to bottom for the lines parallel to the interface.

Figure 5.3(A) corresponds to the line 1 in **Figure 5.1(D)**, in which I can easily distinguish the GNP and the epoxy regions since the average energy-loss of GNPs is higher than that of epoxy matrix, i.e. 24.86 ± 0.135 eV for GNPs and 23.70 ± 0.08 eV for the epoxy matrix. Between them, there exists a narrow region in which the energy-loss decreases gradually. Referring to the STEM image of **Figure 5.1(D)**, this region contains two parts, a GNP region from point 11 to point 19, and an epoxy region from point 20 to point 24, which is considered as a transition layer, namely the interphase, and marked out by **1** and **2**. As mentioned before, the distance between each point is 1 nm and thus the thickness of the interphase is 14 nm. Then, I calculate the average plasmon energy value E_p of the epoxy both in the interphase and the bulk region: I obtain 23.95 ± 0.176 eV in region **2** and 23.70 ± 0.08 eV in the bulk epoxy. According to equation (4), it can be found clearly that the density of the epoxy in the interphase region is increased by 2.12 % compared with the matrix. [If one of the evaluations for the reinforcement of nanofillers are supposed to be the increase of the density [5], it is obvious that GNPs have the enhancement to the surrounded polymer matrix.

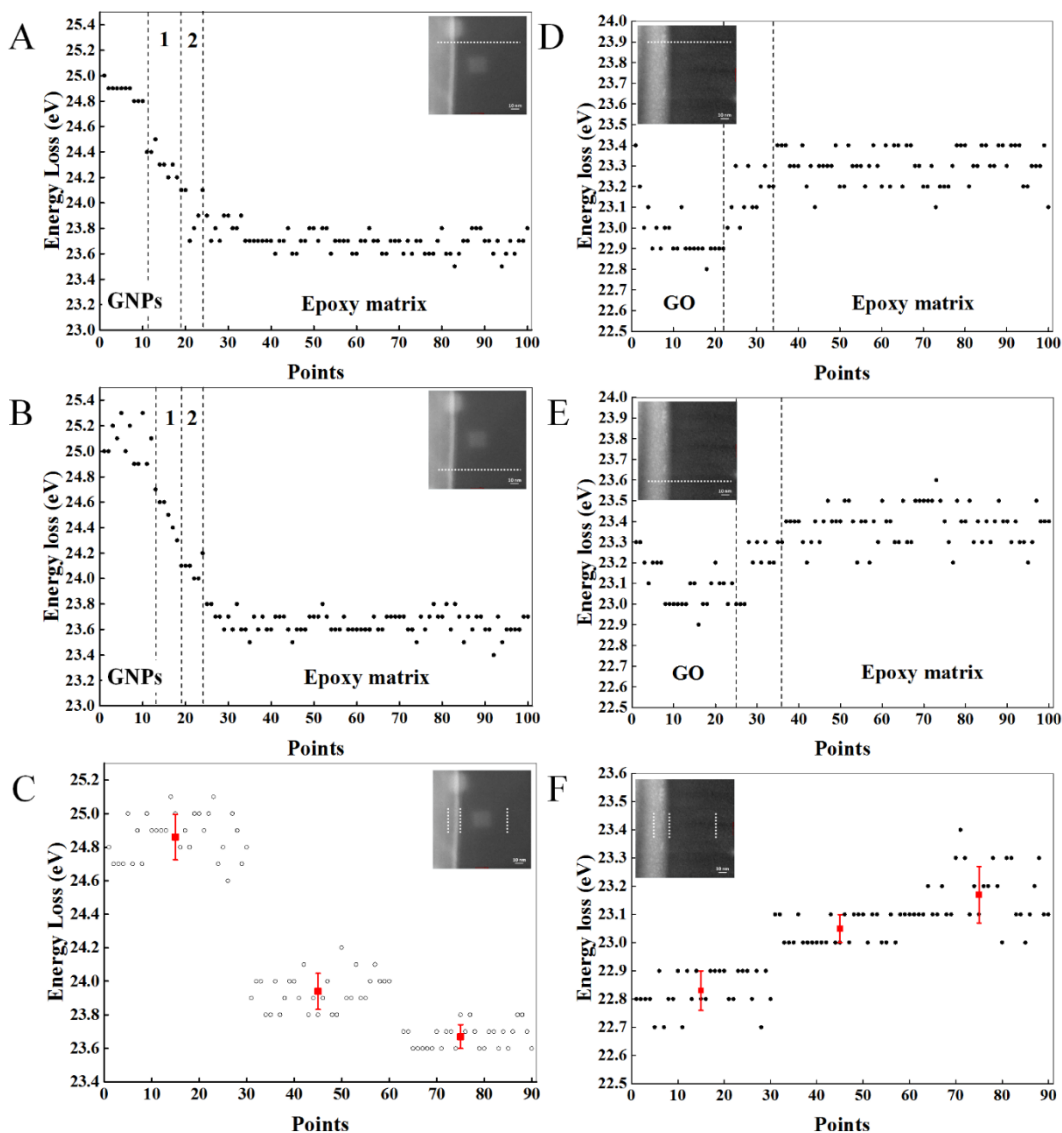


Figure 5.3 the peak positions extracted from the low energy-loss spectra acquired from Figure 5.1(D) and (F), shown as a function of the acquisition order from point 1 to point 100: (A) for line 1 in Figure 5.1(D); (B) for line 2 in Figure 5.1(D); (D) for line 1 in Figure 5.1(F); (E) for line 2 in Figure 5.1(F); three lines parallel to the interface in each images showed the low energy-loss spectra acquisition from three regions, GNPs, epoxy in interphase region and epoxy matrix; the numbers indicate the acquisition order during experiment, point 1 to point 30 for line 3, point 31 to point 60 for line 4 and point 61 to point 90 for line 5, respectively; (C) 90 peak position values of low energy loss spectra from Figure 5.1(D); (F) 90 peak position values of low energy loss spectra from Figure 5.1(F). The inserted images indicate the acquisition position for each spectrum. All the peak values are listed in the table S1

To verify the enhancement phenomenon, as shown in **Figure 5.1(D)**, another region is selected to acquire the low energy-loss spectra and is treated by the same way. The extracted value is shown in **Figure 5.3(B)**. In the graph, three regions can be obviously distinguished which correspond to the GNPs, the epoxy in the interphase region and the bulk epoxy, respectively. The average energy-losses for the three regions are 24.86 ± 0.135 eV, 24.08 ± 0.075 eV and 23.65 ± 0.08 eV, respectively. These values are similar to the former one. After comparison, it can be found that the epoxy density in the interphase region has been improved by 3.67 %, with a thickness of 12 nm. For the same nanofillers, the enhancements on the density and thickness of the interphase are almost kept at the same level.

To make a comparison with the GNPs, I also acquire the low energy-loss spectra of GO/epoxy interface. An aggregated GO platelet was chosen for the acquisition of EEL spectra since single layer GO is too small and rarely perpendicular to the foil plane. 100 spectra are acquired in the interface region, along a distance of 100 nm. The same procedure is applied to the acquired low energy-loss spectra. The peak position value is presented in Figure 5.3(D) and (F). Referring to Figure 5.1(F), the situation is reversed, i.e. the E_p of GO is lower than the epoxy matrix, i.e. 22.83 ± 0.07 eV for GO and 23.17 ± 0.10 eV for the epoxy matrix. It is reasonable since GO has almost the same density as the epoxy matrix. After oxidation, the interlamellar space of GO is doubled compared with graphite. Using this approach, the density of GO is halved ($\rho = 1.06$ g/cm³) [6]. However, there still exists a transition region between GO and the epoxy matrix. As marked by a dashed line in Figure 5.1(D) and (F), the average thickness of the transition layer is 12.5 nm. Due to the fuzzy GO/epoxy boundary, the entire transition layer is considered as the interphase region. After calculation on both lines, the values demonstrate the existence on an interphase region with a decreased density of 1.11 % and 1.62 %, respectively, compared with the epoxy matrix. Furthermore, the plasmon energy-loss of the GO/epoxy composite is decreased by 0.5 eV when compared with GNP/epoxy. This could be due to the oxygen-containing groups on the GO surface. These groups could be in competition with the resin to react with the curing agent, leading to a small decrease of the matrix density.

To further confirm the stability of the interphase, the line acquisitions are conducted in the same region as shown in **Figure 5.1(D)** and **(F)**. Three vertical lines are set at the GNP (respectively GO), the epoxy interphase region and the matrix bulk with a length of 30 nm, respectively. 30 spectra are acquired from each line. The data are treated by the same procedure as discussed before. The peak position values are presented in **Figure 5.3(C)** and **(F)** as a

function of the acquisition order. In **Figure 5.3(C)**, it is obvious that when going from a GNP to towards the epoxy region, the value of E_p decreases gradually: 24.86 ± 0.135 eV for GNPs, 23.94 ± 0.107 eV for epoxy in the interphase region and 23.67 ± 0.071 eV for epoxy in the matrix bulk. The situation is reversed in **Figure 5.3(F)**, in which the value of E_p increases gradually when going from the GO towards the epoxy matrix: 22.83 ± 0.07 eV for GO, 23.05 ± 0.05 eV for epoxy in the interphase region and 23.20 ± 0.10 eV for the epoxy matrix bulk.

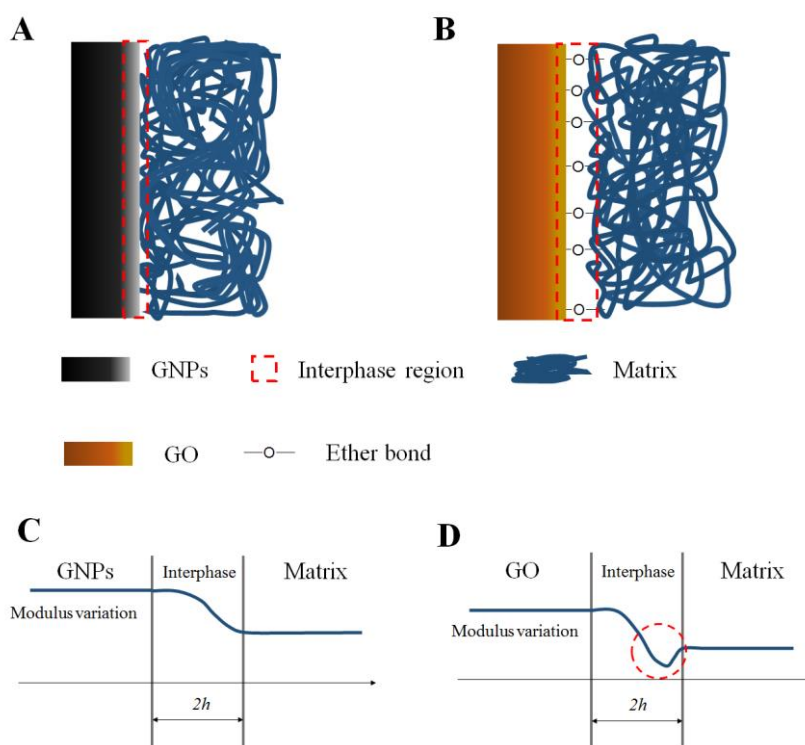


Figure 5.4 Schematic representation of a composite interphase: (A) GNP/epoxy, (B) GO/epoxy; modulus variation in the interphase: (C) GNP/epoxy and (D) GO/epoxy.

According to our results, there exists an interphase region, which connects the reinforced part and the polymer matrix. Due to the crosslinking, the epoxy matrix forms a net structure surrounding the nanofillers. In the case of GNPs, due to its chemical inertness, no chemical reaction happened in the interphase region, leading to a clear and smooth interface, as shown in **Figure 5.4(A)**. After oxidation, the oxygen-containing groups have been introduced onto the graphene plane, epoxy groups on the plane can react with the curing agent, as shown in **Figure 5.4(B)**. The boundary between GO and epoxy is blurred. The density of GO is also halved due to the higher intermellar distance compared to graphite.

The transition layer where the elastic moduli vary continuously between the two materials has been discussed by Delale and Erdogan in 1988 [7]. They considered the thickness of this transition layer as $2h$, ranging from nanometers for an automatically sharp interface, to micrometers for a diffused bi-material interface. Based on our work, it has been found that this transition layer is composed of two parts, the nanofiller and the polymer, respectively. Those with a high-density part take up a thicker transition region, as shown before, 8 nm GNPs part in 13 nm transition-layer of GNPs/epoxy. The larger the difference between the densities of two components, the thicker the thickness of the interphase.

Based on Fan's work [5], there exists a rough relationship between the modulus and the density, $\frac{E_1}{E_2} \propto \left(\frac{\rho_1}{\rho_2}\right)^2$. For the same type of material, a higher density leads to a larger modulus. In the low-loss spectra, the density decreases when going from a GNP towards the epoxy matrix in the transition layer, indicating the decrease of modulus from nanofillers to matrix, as shown in **Figure 5.4(C)**. For GO/epoxy composites, the situation is reversed, since the matrix has a higher density than the GOs. Although GOs have a much lower modulus than the original GNPs, its modulus is still higher than that of the epoxy matrix. Thus, there exists a minimum modulus, which must have a negative influence on the entire properties of the final composites, as marked out by the red circle in **Figure 5.4(D)**.

To obtain better nanocomposite properties, the modification of the nanofillers is usually taken into account since an improved interphase/interface can be achieved between the nanofillers and the matrix. However, for graphene-based composites, after the modification, more defects could be introduced which can negatively influence their intrinsic properties. Although the chemical bonds exist at the interface, the entire mechanical properties of the GO/polymer composite decrease compared with the GNP/epoxy composite. Therefore, a compromise should be considered before functionalization/modification.

5.2 Partial conclusion

In this work, I quantitatively studied the interphase structures between the epoxy matrix and graphene-based materials by using STEM and EELS. The low energy-loss spectra analyses identified an interphase zone. There exists a transition layer between the polymer matrix and the nanofillers, which bridges two parts with a gradually changed density. The density of the GNP/epoxy interphase has been found to be 2.9 % higher compared with the epoxy matrix. However, the density of the GO/epoxy interphase is decreased by 1.4 % compared with the

epoxy matrix. While many oxygen-containing groups are introduced onto the graphene surface after oxidation, the intrinsic properties of the graphene sheets are largely decreased. This work gives an understanding of the interphase of carbon-based composites and provides an indication of the effects of the nanofiller modification. A better interaction between the nanofillers and the matrix in the interface leads to an efficient energy transfer; while the excellent properties of nanofillers should be maintained. Those two aspects should be considered in fabricating polymer matrix composites.

References

1. L. Laffont, M. Monthieux, V. Serin, Plasmon as a tool for in situ evaluation of physical properties for carbon materials, *Carbon* 40(5) (2002) 767-780.
2. A.C. Ferrari, A. Libassi, B.K. Tanner, V. Stolojan, J. Yuan, L.M. Brown, S.E. Rodil, B. Kleinsorge, J. Robertson, Density, sp³ fraction, and cross-sectional structure of amorphous carbon films determined by x-ray reflectivity and electron energy-loss spectroscopy, *Physical Review B* 621(16) (2000).
3. L. Ponsonnet, C. Donnet, K. Varlot, J.M. Martin, A. Grill, V. Patel, EELS analysis of hydrogenated diamond-like carbon films, *Thin Solid Films* 319(1–2) (1998) 97-100.
4. R.A. Rosenberg, P.J. Love, V. Rehn, Polarization-dependent C-K near-edge x-ray-absorption fine structure of graphite, *Physical Review B* 33(6) (1986) 4034-4037.
5. H. Fan, C. Hartshorn, T. Buchheit, D. Tallant, R. Assink, R. Simpson, D.J. Kissel, D.J. Lacks, S. Torquato, C.J. Brinker, Modulus–density scaling behaviour and framework architecture of nanoporous self-assembled silicas, *Nature materials* 6(6) (2007) 418-423.
6. M.A. Rafiee, J. Rafiee, Z. Wang, H. Song, Z.-Z. Yu, N. Koratkar, Enhanced Mechanical Properties of Nanocomposites at Low Graphene Content, *ACS Nano* 3(12) (2009) 3884-3890.
7. F. Delale, F. Erdogan, On the mechanical modeling of the interfacial region in bonded half-planes, *Journal of Applied Mechanics* 55(2) (1988) 317-324.

6.1 General conclusions

This thesis focuses on the interface & interphase study between a polymer matrix and carbon-based fillers, including CFs and GNPs. The main results are concluded as follows:

6.1.1. Surface modification of carbon-based fillers

I applied different surface treatment methods on the reinforcements. Two series of reinforcements, on the micro- and nanometer scale, namely CFs and graphene-based materials, were used here.

To improve the interaction between the nanofillers and the polymer matrix, two major routes were used in this thesis:

(1) The introduction of a “strong” chemical bonding: An oxidation process was conducted for both the CNT-CFs and the GNPs. For oxidized CNT-CFs, the XPS results show that the oxygen fraction increases by 1 % compared to CNT-CFs, indicating the introduction of oxygen-containing groups on the hybrids surface. For the GNPs, two methods were used, surface oxidation in air condition and complete oxidation by the Hummers method. TGA, XPS and morphology characterization reveal a difference between them.

(2) An increase of the surface roughness: CNT-CFs and CNT-GNPs were produced with *in-situ* grafting of CNTs on the surface of CFs and GNPs by CVD. Morphology characterization by TEM and SEM indicated that the CNTs are successfully grafted on the CF and GNP surfaces. For CNT-CFs, the length of CNTs is about 440 nm, with a very dense array. The CNTs on GNP surfaces have a length of tens of micrometers. TGA is conducted to evaluate the mass fraction of CNTs grafted on the GNP and CF surfaces. Since CFs have a much higher decomposition temperature than CNTs, TGA is a suitable method to evaluate the amount of CNTs on CFs. Based on this result, it can be found that 2.5 wt% of CNTs were grafted on CFs.

However, GNPs have a decomposition temperature similar to CNTs, and it was not possible to evaluate the CNT fraction on GNPs with this method.

6.1.2 The interface study between CF and epoxy

A multi-scale investigation of the interface of CF/epoxy composites was conducted.

First, the basic properties of the CFs after modification was investigated, including the raw CFs, desized CFs, CNT-CFs, and the oxidized CNT-CFs. The results indicate that the Young's modulus and ultimate stress of oxidized CNT-CFs can reach the same level as the raw CFs, and are much better than the desized CFs and CNT-CFs.

Secondly, a tensile sample on a micrometer-scale was designed with a bond-shape. The tensile test was successfully conducted in a FIB-SEM column. Based on the results, it was found that grafting a CNT layer on a CF surface can modify the interfacial properties and reinforce the epoxy matrix surrounding the CFs. After further oxidation of CNT-CFs, the interfacial strength can be further increased.

Thirdly, this method was applied to the GNPs/epoxy composite. Since the fracture is not along the interface of GNPs/epoxy, it is not suitable for the interface strength measurement. However, the fracture behavior can be clearly observed on a micro-scale.

Last, STEM observations combined with EDX analyses were conducted. It was found that the interaction between oxygen-containing groups and epoxy was the crucial factor in determining the interfacial strength. This knowledge can be used to guide the modification of other types of reinforcement and fabricate composites with excellent mechanical properties.

6.1.3 Interface & interphase study of GNP/epoxy composites

Four kinds of composites, GNP/epoxy, O-GNP/epoxy, GO/epoxy and CNT-GNP/epoxy, have been studied on the nano-scale, combining STEM-EELS-EDX analyses.

First, to optimize the acquisition conditions of EELS spectra, the effect of TEM sample thickness and electron irradiation time were investigated. It can be found that a thickness under 120 nm limits effects on the low-loss spectra. However, in a certain range, thicker sample are more sensitive to the N and O K-edge peaks.

Then, the low-loss and core-loss spectra of four kinds of composites were studied intensively. The element composition in different samples could be easily obtained by the core-

loss spectra. The density varied in the matrix and nanofiller part. To study further the influence of surface treatments on the interface region, a line scan of the low-loss spectra across the interface region was carried out on GNP/epoxy and GO/epoxy composites. By analyzing the low energy-loss spectra, I successfully identified the interphase zone: a transition layer between the polymer matrix and the nanofillers which bridges two parts with a gradually changing density. The density of the GNP/epoxy interphase was found to be 2.89 % higher compared with that of the epoxy matrix. However, the density of the GO/epoxy interphase was decreased by 1.37 % compared with the epoxy matrix. While many oxygen-containing groups were introduced onto the graphene surface after oxidation, the intrinsic properties of graphene sheets decreased significantly.

This work gives an understanding of the interphase of carbon-based composites and provides an indication for the effects of the modification of nanofillers. A better interaction between the nanofillers and the matrix in the interface leads to efficient energy transfer; while the excellent properties of nanofillers should be maintained. Those two aspects should be considered in fabricating polymer matrix composites.

Thirdly, EDX mapping was also conducted in this work, the interface difference caused by surface treatment could be easily observed, which could be used to indirectly evaluate the interface strength.

Finally, the mechanical and electrical properties of composites were measured. The results indicated that CNT-GNP/epoxy has the best performance in both DMA and conductivity test.

6.2 Perspective

For the CNT-GNPs and CNT-CFs, efforts are needed to study the connecting force between the CNT and its substrate (GNPs and CFs in our present study). It helps exploring the mechanism of CNT growth. Moreover, the quantification of interactions makes a crucial contribution to prevent the macroscopic device from failure during the subsequent procedures such as surface functionalization and mixing process.

As I mentioned in the thesis, besides the interfacial interaction, the dispersion state of nanofillers also plays a major role on the final composite performance, especially with GOs, which have a strong aggregation tendency after oxidation. To achieve more homogeneous nanofiller dispersion in composites, processing parameters need to be well studied.

Based on others' results (see chapter 3 for references), the fiber diameter is crucial for the determination of the interaction volume in single fiber fragmentation tests. choosing the cross-section area including the CNTs can increase the determined value. In in-situ tensile tests, the length of the CNT layer needs to be considered. The oxidized CNT-CFs have the best interaction with the epoxy matrix compared to desized CFs and CNT-CFs. CNT-CFs combined with the sizing process can be studied.

I identified an interphase region by using low-loss spectra in the epoxy matrix. This region has a varying density due to the different surface environment. Apart from the nanofillers, it is quite promising to study the interphase by changing the matrix, such as varying the post-curing time, changing the curing agent/resin ratio, etc.

I used SEM-FIB and TEM observations to study the interface and obtained the density variation across the interface, very useful to understand the structure-property relationships in composites. Atomic force microscope (AFM) could be used to study the mechanical properties in a local region. The combination of two methods is quite promising.

Appendix I Directly measuring interfacial shear strength between Polymethyl methacrylate and graphene nanoplatelets

1 Introduction

Graphene has attracted enormous attentions since reported in 2004 [1]. Due to its excellent physical and chemical properties, graphene may have a wide range of applications in a variety of engineering applications. Very recently, graphene based polymer composites have been extensively studied in order to improve electrical and mechanical properties of polymers. However, the preparation of single-layer graphene is quite expensive and involved in complicated process, which leads to a small yield. Attentions have been paid to graphene nanoplatelets (GNPs), which have been studied for their use as reinforcements in polymer composites, especially for improving their mechanical properties including Young's modulus, tensile strength and toughness, as well as their electrical conductivity [2].

The mechanical properties of polymer composites are influenced by several aspects, such as dispersion, orientation and interfacial properties of the reinforcement [3]. Among them, the interfacial shear strength (IFSS) is the critically important value for the stress transfer from polymer to the reinforcement [4]. The existing stress transfer model for the two-dimensional reinforcement assumed that the plane of the platelet was bonded to the polymer matrix, and was parallel to the loading direction. The edges of the platelet were debonded to the polymer matrix such that the stress transfer only occurred on the plane of the platelet [5]. Many efforts have been made to directly and indirectly measure the IFSS of polymer composites. The IFSS values were shown to have a large scattering, due to the different experiment configuration with specific assumptions and the technical difficulties during the measurement.

In this work, we propose to use a simple sandwiched structure to directly measure the IFSS by tensile test. Two types of polymers, polymethyl methacrylate (PMMA) and polyvinyl alcohol (PVA), sandwiched GNPs in the contact area. Then, an in-plane load was applied to

stretch the structure. By changing the GNPs density covering the interface, we could obtain a series of mean IFSS. Linear fitting will be done to deduce the average IFSS of PMMA-GNPs.

2 Experimental section

2.1 Samples preparation

PMMA in DMF solutions was spread freely to form a homogeneous film on a glass substrate, dried at 45 °C for 48h. We used the same method to prepare PVA films, but for the solution which was deionized water, and the substrate which was plastic. The thickness of the PMMA and PVA films thus obtained were ~0.5mm and ~0.3mm, respectively. Then, both films were cut into rectangular films (Fig.1(1)).

The GNP dispersion was prepared by ultrasonication (KNG-G5, KNANO Science Inc., China) in pure ethanol. A spray coating method was used to homogeneously deposit GNPs on the PMMA surface with a commercial airbrush (WilTec GmbH, Germany) (Fig.1(2)). GNPs with different densities were obtained by varying the spray duration.

A little amount of water was used in the PMMA and PVA contact area. PVA easily dissolve in water. Then, we pressed the two films together and kept in perfect contact. The PMMA and PVA contact interface is 1.5 cm * 1.0 cm. Last, we dried the sandwich structure at 45 °C during at least 1 week to ensure the evaporation of water which existed on the interface (Fig.1(3)).

2.2 Microstructure characterization and Tensile test

The microstructure of different surfaces was observed by scanning electron microscope (SEM) (ZEISS, LEO 1530 Gemini). To calculate the GNP covered areas on the PMMA surface, we considered all the GNPs transferred to PVA surface after separated. Optical microscope images of the separated PVA surface (Fig. 4A) were treated with ImageJ in order to calculate the GNP density (Fig. 4B). Tensile tests were carried out with an Instron machine 5544. An in-plane load was applied with two cross-head clamped on the PMMA and PVA films, respectively, using a load cell of 100N and a speed of 1mm/min (Fig. 1(4)).

3 Results and discussion

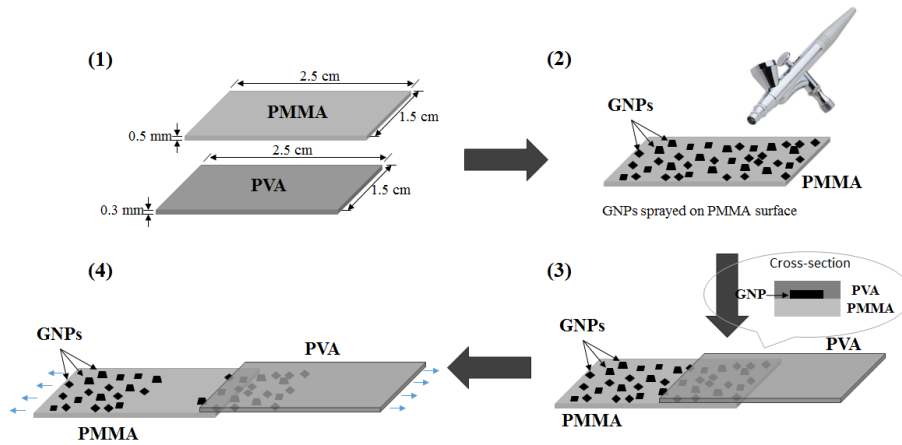


Figure 1 Illustration of the stretching method used in this work.

We designed an easily stretching method to directly measure the mean IFSS between the GNPs and the PMMA matrix. GNPs were used as received without any further treatment and have an average size of about 5 μm across and 5 nm in thickness, as showed in Fig. 2(A). The GNPs had a very uniform distribution on the PMMA layer after being sprayed, and most of the GNPs were paved on the polymer surface (Fig. 2(B)). During the spraying stage, the GNP containing ethanol solution was heated up to 80 $^{\circ}\text{C}$. After the evaporation stage, it had no influence on the PMMA film.

To confirm that the measured interface was indeed the PMMA-GNPs interface, we observed the surface after separation by using a SEM. As we can see on Fig. 2(C), compared with Fig. 2(B), dents were observed with the shapes of GNPs in the red circled region, where no platelet could be found. However, on the PVA surface, there appeared GNP planar surfaces could be observed (Fig. 2(D)): The GNPs transferred from the PMMA to the PVA surface in the process, which indicates the higher strength of the PVA-GNPs interface compared with the PMMA-GNPs interface [6]. Furthermore, the PVA on the surface surrounded the GNPs, some part even covered the GNPs surface (blue circled region in Fig. 2D), thus decreasing the size of the GNP-PMMA interface.

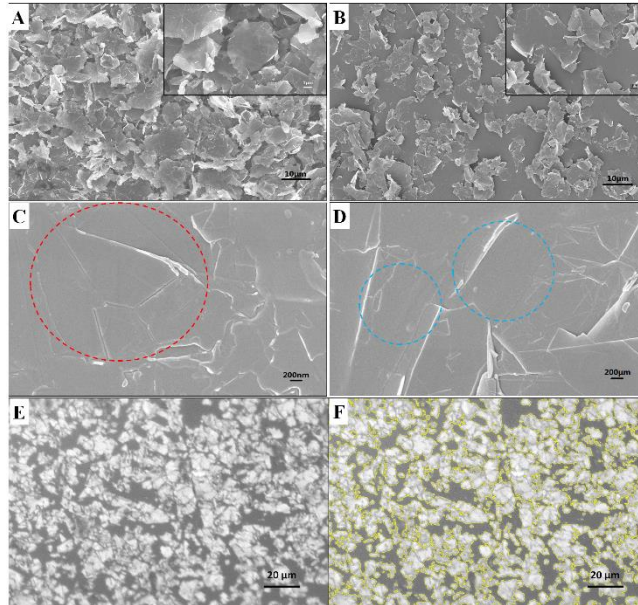


Figure 2 SEM images of (A) Original GNPs, (B) GNPs deposited on PMMA surface by spray, (C) PMMA surface after separation from the PVA (the contact area), (D) PVA surface after separation from the PMMA (the contact area). (E) Optical image of the PVA surface after separation by stretching (1000X), (F) Optical image of the PVA surface processed by ImageJ to calculate the GNP covered density (1000X).

The stretching test for all specimens was conducted in order to obtain F_s - the maximum separating force. A crosshead speed of 1mm/min, and a 100N load cell were chosen for the testing. 20 specimens with different GNP-density were tested and 12 of them yielded valid F_s data.

After the separation, each PVA film was cut to a certain size to be observed by optical microscopy. Ten photos of each film were taken and a typical PVA contacting surface was showed on Fig. 2(E). The bright areas on the PVA surface correspond to the GNPs transferred from the PMMA surface. The GNPs were large enough as we can see all of them homogeneously paving the PVA surface. Then, we used ImageJ to calculate the GNPs covered areas on the PVA surface Fig. 2(F). We chose ten areas of each film, calculated the GNP covered areas and took the average to ensure more precise results. The densities ranged from 37.6% to 87.3%.

The IFSS between GNPs and PMMA has been analyzed by means of stretching test, which is a simple test for directly assessing the IFSS by variation of GNP covered areas on the PMMA

surface. The average IFSS between GNPs and PMMA could be calculated according to the following equation, which assumes of a constant IFSS between the GNPs and its contact matrix:

$$\tau_m = \frac{F_s}{l_c w_c} \quad (1)$$

Here, F_s is the maximum separating force obtained in the tensile test, l_c (~1.0cm) and w_c (~1.5cm) stand respectively for the length and the width of the contact area in the sandwich structure. A more precise measurement of the length was processed by a vernier caliper. According to the SEM observation of the polymer surface after stretching, the interface separation occurred as a result of the interfacial gliding of the two surfaces in contact. Therefore, we designated the value calculated from Eq. (1) as the mean IFSS.

Statistical analyses on the mean IFSS were conducted using a linear fitting in conjunction with the stretching test. The results are shown on Fig. 3.

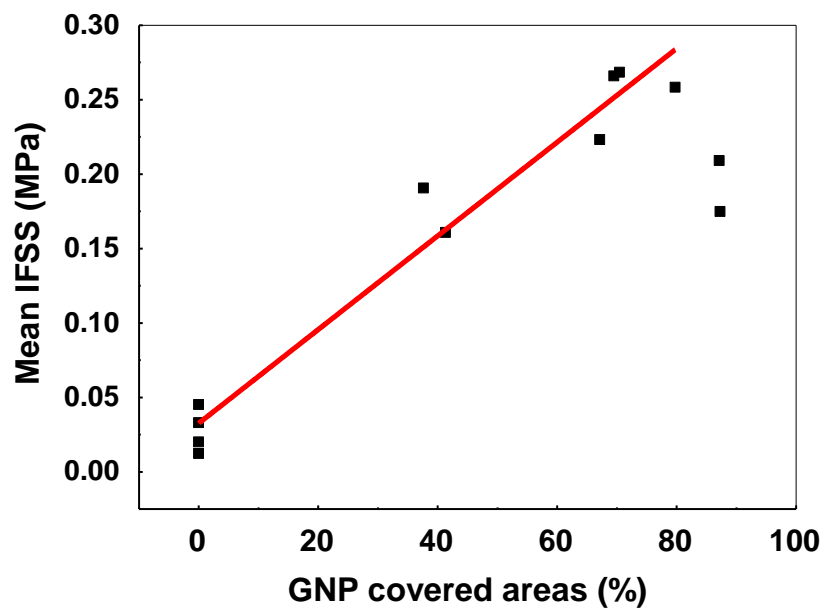


Figure 3 Statistical analysis of the mean IFSS as a function of the GNP covered area.

By fitting the experimental data using the Origin fitting method, we obtained the line equation as:

$$\text{mean IFSS} = 0.00315a + 0.03269 \quad (2)$$

Here, a is the GNP covered area sprayed on the PMMA surface, which was calculated by using ImageJ. The line fitted the data very well. The line extension up to a value of 100% for

a gives a mean IFSS value of 0.35 MPa, which corresponds to a case when the surface is completely covered by GNPs and when only GNPs contacted with the PMMA layer. This value could represent the mean IFSS between GNPs and PMMA. Such a value was comparable to the mean IFSS value tested by other method [7-9]. However, when we continued to increase the GNP covered areas to ~87% during our experiment, the mean IFSS decreased: When the GNP density increased, a part of the platelets overlapped. During the stretching process, the interface between the GNPs glided instead of the interface between GNPs and PMMA, which led to the decrease of the value of the mean IFSS.

4 Conclusion

In this study, we developed a novel method to directly characterize and measure the mean IFSS between GNPs and polymers by a statistical analysis. The method was successfully applied to measure the mean IFSS between GNPs and PMMA, which was about 0.35 MPa. It has important implications for the use of GNPs as reinforcement in composites. This method also could be applied to other nanocomposite systems, allowing for the determination of the IFSS between nanoparticles and the polymer.

Reference

- [1] A.K. Geim, K.S. Novoselov, The rise of graphene, *Nat Mater*, 6 (2007) 183-191.
- [2] X. Ji, Y. Xu, W. Zhang, L. Cui, J. Liu, Review of functionalization, structure and properties of graphene/polymer composite fibers, *Composites Part A: Applied Science and Manufacturing*, 87 (2016) 29-45.
- [3] S. Stankovich, D.A. Dikin, G.H.B. Dommett, K.M. Kohlhaas, E.J. Zimney, E.A. Stach, R.D. Piner, S.T. Nguyen, R.S. Ruoff, Graphene-based composite materials, *Nature*, 442 (2006) 282-286.
- [4] Y. Wyser, Y. Leterrier, J.A.E. Månson, Analysis Of Failure Mechanisms In Platelet-Reinforced Composites, *Journal of Materials Science*, 36 (2001) 1641-1651.
- [5] C.-H. Hsueh, A two-dimensional stress transfer model for platelet reinforcement, *Composites Engineering*, 4 (1994) 1033-1043.
- [6] D.E. Kranbuehl, M. Cai, A.J. Glover, H.C. Schniepp, Measurement of the interfacial attraction between graphene oxide sheets and the polymer in a nanocomposite, *Journal of Applied Polymer Science*, 122 (2011) 3739-3743.
- [7] L. Gong, I.A. Kinloch, R.J. Young, I. Riaz, R. Jalil, K.S. Novoselov, Interfacial Stress Transfer in a Graphene Monolayer Nanocomposite, *Advanced Materials*, 22 (2010) 2694-2697.
- [8] G. Guo, Y. Zhu, Cohesive-Shear-Lag Modeling of Interfacial Stress Transfer Between a Monolayer Graphene and a Polymer Substrate, *Journal of Applied Mechanics*, 82 (2015) 031005-031005.
- [9] T. Jiang, R. Huang, Y. Zhu, Interfacial Sliding and Buckling of Monolayer Graphene on a Stretchable Substrate, *Advanced Functional Materials*, 24 (2014) 396-402.

Appendix II The peak positions values of Figure 5.3

Acquisition position (Points)	Energy Loss (eV)					
	Fig. 5.3A	Fig. 5.3B	Fig. 5.3C	Fig. 5.3D	Fig. 5.3E	Fig. 5.3F
1	25	25	24.8	23.4	23.3	22.8
2	24.9	25	24.7	23.2	23.3	22.8
3	24.9	25.2	24.7	23	23.2	22.8
4	24.9	25.1	24.7	23.1	23.1	22.8
5	24.9	25.3	25	22.9	23.2	22.7
6	24.9	25	24.7	23	23.2	22.9
7	24.9	25.2	24.9	22.9	23.2	22.7
8	24.8	24.9	24.7	23	23	22.8
9	24.8	24.9	25	23	23	22.8
10	24.8	25.3	24.9	22.9	23	22.9
11	24.4	24.9	24.9	22.9	23	22.7
12	24.4	25.1	24.9	23.1	23	22.9
13	24.5	24.7	24.9	22.9	23	22.8
14	24.3	24.6	25.1	22.9	23.1	22.9
15	24.3	24.6	25	22.9	23.1	22.8
16	24.2	24.5	24.8	22.9	22.9	22.8
17	24.3	24.4	24.9	22.9	23	22.9
18	24.2	24.3	24.8	22.8	23	22.9
19	24.1	24.1	25	22.9	23.1	22.9
20	24.1	24.1	25	22.9	23.2	22.9
21	23.7	24.1	24.9	22.9	23.1	22.8
22	23.8	24	25	22.9	23.1	22.8
23	23.9	24	25.1	23	23	22.9
24	24.1	24.2	24.7	23.1	23.1	22.9
25	23.9	23.8	24.8	23.3	23	22.9
26	23.7	23.8	24.6	23	23	22.8
27	23.8	23.7	25	23.1	23	22.9
28	23.7	23.7	24.9	23.3	23.3	22.7
29	23.9	23.6	24.7	23.1	23.2	22.9
30	23.9	23.7	24.8	23.1	23.3	22.8
31	23.8	23.6	23.9	23.2	23.2	23.1
32	23.8	23.8	24	23.3	23.3	23.1
33	23.9	23.6	24	23.2	23.2	23
34	23.7	23.6	23.8	23.2	23.2	23
35	23.7	23.5	23.8	23.4	23.3	23
36	23.7	23.7	24	23.4	23.3	23.1
37	23.7	23.6	23.8	23.4	23.4	23
38	23.7	23.7	23.9	23.3	23.4	23
39	23.7	23.6	24	23.3	23.4	23
40	23.7	23.6	24	23.3	23.4	23

41	23.6	23.7	23.9	23.4	23.3	23
42	23.7	23.7	24.1	23.2	23.2	23
43	23.7	23.7	23.8	23.3	23.3	23.1
44	23.8	23.6	23.9	23.1	23.4	23
45	23.6	23.5	23.8	23.3	23.3	23
46	23.6	23.6	23.9	23.3	23.4	23.1
47	23.7	23.6	24	23.3	23.5	23
48	23.7	23.6	23.8	23.3	23.4	23.1
49	23.8	23.7	23.8	23.4	23.4	23.1
50	23.8	23.7	24.2	23.2	23.4	23.1
51	23.7	23.7	23.9	23.2	23.5	23
52	23.8	23.8	23.9	23.4	23.5	23.1
53	23.8	23.7	24.1	23.3	23.4	23.1
54	23.6	23.6	23.9	23.3	23.2	23
55	23.7	23.6	23.9	23.3	23.4	23
56	23.7	23.6	24	23.2	23.4	23.1
57	23.7	23.7	24.1	23.3	23.2	23
58	23.7	23.6	24	23.4	23.4	23.1
59	23.6	23.6	24	23.3	23.3	23.1
60	23.6	23.6	24	23.2	23.5	23.1
61	23.7	23.6	24	23.4	23.4	23.1
62	23.7	23.6	24	23.2	23.4	23.1
63	23.8	23.6	23.7	23.4	23.3	23.1
64	23.7	23.7	23.7	23.4	23.3	23.2
65	23.7	23.6	23.6	23.2	23.5	23.1
66	23.6	23.6	23.6	23.4	23.3	23.1
67	23.6	23.7	23.6	23.4	23.3	23.2
68	23.7	23.7	23.6	23.3	23.5	23.1
69	23.7	23.7	23.6	23.3	23.5	23.1
70	23.7	23.7	23.7	23.2	23.5	23.3
71	23.6	23.7	23.6	23.2	23.5	23.4
72	23.7	23.6	23.7	23.3	23.5	23.3
73	23.6	23.6	23.7	23.1	23.6	23.1
74	23.7	23.5	23.6	23.2	23.5	23.2
75	23.7	23.7	23.8	23.2	23.4	23.1
76	23.6	23.6	23.7	23.2	23.3	23.2
77	23.6	23.7	23.8	23.3	23.2	23.2
78	23.6	23.8	23.7	23.4	23.5	23.3
79	23.7	23.7	23.6	23.4	23.4	23.2
80	23.8	23.7	23.6	23.4	23.4	23
81	23.6	23.8	23.7	23.2	23.5	23.3
82	23.6	23.6	23.7	23.3	23.3	23.3
83	23.5	23.8	23.6	23.3	23.4	23.1
84	23.6	23.7	23.7	23.4	23.3	23.1

85	23.7	23.5	23.6	23.4	23.4	23
86	23.7	23.7	23.7	23.3	23.3	23.1
87	23.8	23.6	23.8	23.3	23.4	23.2
88	23.8	23.7	23.8	23.4	23.5	23.3
89	23.8	23.7	23.7	23.4	23.4	23.1
90	23.7	23.6	23.6	23.3	23.4	23.1
91	23.7	23.6		23.4	23.3	
92	23.6	23.4		23.4	23.4	
93	23.7	23.7		23.4	23.3	
94	23.5	23.5		23.2	23.3	
95	23.6	23.6		23.2	23.2	
96	23.7	23.6		23.3	23.3	
97	23.6	23.6		23.3	23.5	
98	23.7	23.6		23.3	23.4	
99	23.7	23.7		23.4	23.4	
100	23.8	23.7		23.1	23.4	

Titre : Etude d'interface entre matrice polymère et renforts à base de carbone, à l'aide d'observations multiéchelles et multimodales en microscopie électronique

Mots clés : Interface/Interphase, Composites GNP/époxy, Composites CF/époxy, MEB-FIB, Traitement de surface, STEM-EELS

Résumé : Cette thèse vise à étudier le comportement multiéchelle (nano-, micro- et macroscopique) des composites, basé sur une étude fine utilisant les techniques les plus modernes pour comprendre les interfaces et les quantifier. Deux séries de renforts sur une échelle micrométrique, des fibres de carbone (CF) et des matériaux à base de graphène ont été utilisées ici. Pour améliorer l'interaction entre les nanorenforts et la matrice polymère, deux voies principales ont été utilisées dans cette thèse : l'oxydation des renforts et la greffe de nanotubes de carbone sur leur surface.

L'étude en elle-même a été menée à une échelle microscopique pour étudier la résistance interfaciale entre une fibre de carbone (CF) et la matrice époxy, avec des essais de traction effectués in situ dans la chambre d'un microscope à double colonne MEB-FIB (microscope électronique à balayage couplé à un faisceau d'ions focalisé). Le faisceau d'ions a été utilisé pour découper une éprouvette de traction du composite contenant à la fois de l'époxy et de la CF. Le champ de traction

a été appliqué via le nanomanipulateur et l'essai a été observé via les deux colonnes ionique et électronique (sous deux angles de vue différents) et a permis d'estimer le champ de déformation, et donc la résistance interfaciale au moment de la rupture. Une expérience similaire a été menée sur un composite où les renforts sont des nanoplaquettes de graphène.

Enfin, l'étude en microscopie électronique en transmission de la région de l'interface entre l'époxy et les renforts a révélé la présence d'une interphase et a permis de mesurer son épaisseur et donner une indication de sa nature. À cette fin, une analyse EELS (spectroscopie par pertes d'énergie des électrons) a été effectuée, permettant de mesurer la densité de l'échantillon très localement (taille de sonde de l'ordre du dixième de nanomètre) en travers ou parallèlement à l'interface. Un scénario sur les modes de liaison chimique entre les deux milieux en fonction du traitement de surface utilisé permet d'expliquer la nature des interphases observées.

Title : Interface Study between polymer matrix and carbon-based reinforcements, using the electron microscopy in multiscale and multimodal

Keywords : Interface/Interphase, GNP/epoxy composites, CF/epoxy composites, FIB-SEM, Surface treatment, STEM-EELS

Abstract : This thesis aims to investigate the multiscale (nano-, micro-, and macro-scopic) behavior of the composites based on a fine investigation using the most modern techniques, to understand the interfaces and to quantify them. Two series of reinforcements on a micrometer scale, carbon fibers (CFs) and graphene-based materials, were studied here. To improve the interactions between these nanofillers and the surrounding polymer matrix, two major routes were used in this thesis: the oxidation of the fillers and the grafting of carbon nanotubes on their surface.

The study itself was conducted on a microscopic scale on the interfacial strength between CFs and the epoxy matrix, with tensile tests carried out in-situ in the chamber of a double-column FIB-SEM microscope (scanning electron microscope coupled to a focused ion beam). The ion beam was used to mill a thin bond-shaped tensile specimen of composite containing both an epoxy and a CF part. The

tensile stress field was applied using the nanomanipulator and the test was observed both via the ionic and the electronic columns (with two different angles of view) to estimate the strain field, hence the interfacial strength when the failure is observed. A similar experiment was led on a composite with GNPs.

Finally, the transmission electron microscopy (TEM) study of the interface region between the epoxy and the graphene-based nanofillers revealed the existence of an interphase and allowed to measure its thickness and give an indication of its nature. For this purpose, an EELS (electron energy-loss spectroscopy) analysis was carried out, making it possible to measure the density of the sample very locally (probe size of the order of a tenth of a nanometer) across or parallelly to an interface. A scenario on the chemical bonding modes between the two media as a function of the surface treatment used makes it possible to explain the nature of the observed interphases.

